



**DETERMINATION OF THE CONSTITUTIVE EQUATIONS FOR 1080 STEEL
AND VASCOMAX 300**

THESIS

Zachary A. Kennan, Ensign, USNR

AFIT/GAE/ENY/05-J05

**DEPARTMENT OF THE AIR FORCE
AIR UNIVERSITY**

AIR FORCE INSTITUTE OF TECHNOLOGY

Wright-Patterson Air Force Base, Ohio

APPROVED FOR PUBLIC RELEASE; DISTRIBUTION UNLIMITED

The views expressed in this thesis are those of the author and do not reflect the official policy or position of the United States Air Force, Department of Defense, or the U.S. Government.

AFIT/GAE/ENY/05-J05

**DETERMINATION OF THE CONSTITUTIVE EQUATIONS FOR 1080 STEEL
AND VASCOMAX 300**

THESIS

Presented to the Faculty

Department of Aeronautics and Astronautics

Graduate School of Engineering and Management

Air Force Institute of Technology

Air University

Air Education and Training Command

In Partial Fulfillment of the Requirements for the
Degree of Master of Science in Aeronautical Engineering

Zachary A. Kennan, BS

Ensign, USNR

June 2005

APPROVED FOR PUBLIC RELEASE; DISTRIBUTION UNLIMITED

AFIT/GAE/ENY/05-J05

**DETERMINATION OF THE CONSTITUTIVE EQUATIONS FOR 1080 STEEL
AND VASCOMAX 300**

Zachary A. Kennan, BS

Ensign, USNR

Approved:

Dr. Anthony N. Palazotto (Chair)

Date

Dr. Theodore Nicholas (Member)

Date

Dr. William P. Baker (Member)

Date

Abstract

The objective of this research is to establish a better representation of the components utilized in a gouging event being considered in research leading to a better understanding of the Holloman High Speed Test Track. Gouging occurs when two metals are traveling at a slight incline to each other at velocities nearing 1.5 kilometers per second, and results in a structural failure of both the metals. The gouging process occurs at very high strain rates, which results in non-linear stress-strain relations.

The coefficients that lead to the Johnson-Cook equations have been determined by the Split Hopkinson Bar test for 1080 steel and VascoMax 300. The Split Hopkinson Bar test was conducted using various strain rates and temperatures to produce meaningful stress-strain relations for both of the steels. These relations allowed a fit of the data to yield specific material coefficients defined in the Johnson-Cook constitutive model. Both the 1080 steel and Vascomax 300 models showed excellent approximation of the plastic region. Verification of the constitutive models was conducted through the use of Taylor tests. A Taylor test model utilizing the constitutive equations was developed in CTH and produced deformation profiles that closely resembled specimens taken from experimental Taylor tests. The end result of this work will be utilized in further studies toward overall high energy impact evaluation.

Acknowledgments

I would like to express my sincere appreciation to my thesis advisor, Dr. Anthony Palazotto, for his unwavering support and dedication to the completion my thesis. His knowledge and experience proved to be invaluable and necessary for my success. Dr. Theodore Nicholas' immense background in the Split Hopkinson Bar test and constitutive models guided me in understanding the behavior of materials under dynamic loading. Without his class notes and office time, I would have been completely lost in the art form known as constitutive modeling. I would also like to thank Major John Cinnamon for his constant vigil over my progress and additions to this thesis, which would have been less in-depth without his help. His Taylor test data proved invaluable to the verification of the Johnson-Cook models for 1080 steel and VascoMax300. For the generous financial support of this endeavor, I thank Dr. Neil Glassman of AFOSR and Dr. Michael Hooser of 846th TS/TGTM. Finally, but not least, I would like to thank my parents, brother, and sister for their endless hours of motivation and support.

Zachary A. Kennan

Table of Contents

	Page
Abstract	iv
Acknowledgments.....	v
Table of Contents	vi
List of Figures	viii
List of Tables	xii
Nomenclature	xiii
Chapter 1 – Introduction	1
Chapter 2 - Background and Theory.....	6
2.1 Conservation Equations.....	6
2.2 Stress Waves in a Continuum.....	8
2.3 Split Hopkinson Bar	21
2.4 Constitutive Equation.....	30
Chapter 3 – The Use of the Split Hopkinson Bar Technique in Evaluating the Johnson- Cook Constitutive Model for 1080 steel and VascoMax 300.....	34
3.1 Tension Split Hopkinson Bar Technique	34
3.2 Determination of 1080 Johnson-Cook Constitutive Model	43
3.3 Determination of VascoMax 300 Johnson-Cook Constitutive Model	64
Chapter 4 – Evaluation of the Johnson-Cook Coefficients for 1080 steel and VascoMax 300.....	87
4.1 Taylor Test and CTH Model	87
4.2 Verification of the Johnson-Cook coefficients for 1080 steel.....	92
4.3 Verification of the Johnson-Cook coefficients for VascoMax 300.....	104
4.4 Comparison of 1080 and VascoMax 300 to Iron and VascoMax 250.....	112

	Page
Chapter 5 – Conclusions and Recommendations.....	119
5.1 Conclusions	119
5.2 Recommendations for Future Research	123
Appendix 1.....	125
Appendix 2.....	141
Appendix 3.....	144
Appendix 4.....	156
Appendix 5.....	159
Appendix 6.....	164
Vita.....	170

List of Figures

	Page
Figure 1 - Rocket Sled at HHSTT.....	1
Figure 2 - Slipper/Rail Attachment.....	2
Figure 3 – Gouge Section	3
Figure 4 - Schematic View of Gouge	4
Figure 5- Rod Impact	9
Figure 6 - Material Element.....	11
Figure 7 - Rod Impact Experiment before Reflection	14
Figure 8 - Rod Impact Experiment after Reflection	15
Figure 9 - Lagrangian Diagram for Rod Impact Problem.....	16
Figure 10 - Bilinear Stress-Strain Curve and Corresponding Wave Profile.....	18
Figure 11 - Shock Formation	19
Figure 12 – Flow Stress Behavior at Different Strain Rates.....	20
Figure 13 - Tension Split Hopkinson Bar	24
Figure 14 - Tensile SHB Wave Propagation.....	25
Figure 15 - Lagrangian Diagram for Tensile SHB	25
Figure 16 - UDRI Split Hopkinson Bar Schematic	35
Figure 17 - SHB Specimen Dimensions	36
Figure 18 - UDRI Split Hopkinson Bar Apparatus.....	37
Figure 19 - Strain Gage on SHB	38
Figure 20 - UDRI Oscilloscope/Amplifier Setup	39

	Page
Figure 21 - Sample Strain Gage Trace.....	39
Figure 22 - Induction Coil Apparatus	42
Figure 23 - Quasi-static Tension Test for 1080 Steel	44
Figure 24 - 1080 Steel Quasi-static test 474-2.....	46
Figure 25 - 1080 Steel Quasi-static test 474-3.....	47
Figure 26 - Plastic Region Fit of 1080 Test 474-2.....	48
Figure 27 - Plastic Region Fit of 1080 Test 474-3.....	49
Figure 28 - Sample Time-History Plot.....	52
Figure 29 - Quasi-static test 474-2 J-C Fit.....	53
Figure 30 - Quasi-static test 474-3 J-C Fit.....	54
Figure 31 - Strain Rate Sensitivity of 1080 Steel	55
Figure 32 - m Coefficient for 1080 steel at 500/s	57
Figure 33 - 1080 J-C Fit of Dynamic Loading	59
Figure 34 – UDRI 1080 J-C fit of Dynamic Loading	60
Figure 35 - J-C Fit of 1080 steel at 500F at 500/s	61
Figure 36- J-C Fit of 1080 steel at 500F at 1000/s	62
Figure 37 - J-C Fit of 1080 steel at 500F at 1500/s	63
Figure 38 - Necking in VascoMax 300.....	64
Figure 39 - Quasi-static Tension test for VascoMax 300	65
Figure 40 - Taylor-Hobson Profilometer	68
Figure 41 - Specimen Setup on Profilometer.....	69

	Page
Figure 42 - Ultra Raw Profile of VascoMax 300 Test 11	70
Figure 43 - Comparison of Uncorrected and Corrected VascoMax 300	73
Figure 44 - Data Averaging Correction to VascoMax 300.....	74
Figure 45 - VascoMax 300 Quasi-static test 474-5	76
Figure 46 – Plastic Region Fit of VascoMax 300 test 474-5	77
Figure 47 - Plastic Region Fit of VascoMax 300 test 474-6.....	78
Figure 48 - Strain Rate Sensitivity of VascoMax 300	79
Figure 49 - m Coefficient for VascoMax 300 at 500/s	80
Figure 50 - VascoMax 300 J-C Fit of Dynamic Loading	82
Figure 51 – UDRI VascoMax 300J-C Fit of Dynamic Loading.....	83
Figure 52 - J-C Fit of VascoMax 300 at 750F at 500/s	84
Figure 53 - J-C Fit of VascoMax 300 at 750F at 1000/s	85
Figure 54 - J-C Fit of VascoMax 300 at 750F at 1500/s	86
Figure 55 - Taylor Test Experimental Setup.....	88
Figure 56 – Taylor Test Grid	90
Figure 57 - 1080 Steel test S8 Initial Contact.....	94
Figure 58 - 1080 Steel test S8 Final Contact	95
Figure 59 - Comparison of CTH model and Taylor test S8.....	96
Figure 60 – Rod Diagram	97
Figure 61 - 1080 steel CTH test S8 Nose Deformation	98
Figure 62 - 1080 steel CTH test S8 Change in Length.....	98

	Page
Figure 63 - 1080 steel CTH test S8 Undeformed Length	99
Figure 64 - 1080 steel CTH test S9 Nose Deformation	100
Figure 65 - 1080 steel CTH test S8 Change in Length	101
Figure 66 - 1080 steel CTH test S8 Undeformed Length	101
Figure 67 - VascoMax 300 test V7 Initial Contact	105
Figure 68 - VascoMax 300 test V7 Final Contact	106
Figure 69 – Comparison of CTH model and Taylor test V7	107
Figure 70 – VascoMax 300 CTH test V7 Nose Deformation.....	108
Figure 71 - VascoMax 300 CTH test V7 Change in Length	108
Figure 72 - VascoMax 300 CTH test V7 Undeformed Length	109
Figure 73 – 1080 Strain Rate for test S8.....	116
Figure 74 - 1080 Temperature for test S8.....	116
Figure 75 – VascoMax 300 Strain Rate for test S8	117
Figure 76 - VascoMax 300 Temperature for test S8.....	117

List of Tables

	Page
Table 1 - 1080 and VascoMax Test Matrix	43
Table 2 - 1080 Johnson-Cook Coefficients from Quasi-static tests	49
Table 3 - J-C Coefficients for 1080 Steel	57
Table 4 - VascoMax 300 Diameter Change.....	71
Table 5 - Correction of VascoMax 300	72
Table 6 - J-C Coefficients for VascoMax 300	81
Table 7 - 1080 Taylor Test Results.....	88
Table 8 - VascoMax 300 Taylor Test Results	89
Table 9 - 1080 steel Johnson-Cook Coefficients	92
Table 10 - VascoMax 300 Johnson-Cook Coefficients	93
Table 11 - Comparison of 1080 steel Taylor tests	102
Table 12 - 1080 steel J-C Coefficients with and without 0.08 Strain.....	103
Table 13 - 1080 steel Deformation Comparision.....	104
Table 14 - Comparison of VascoMax 300 Taylor tests	110
Table 15 - Comparison of VascoMax 300 Taylor Tests.....	111
Table 16 - Iron Johnson-Cook Coefficients.....	112
Table 17 - Iron vs. 1080 Taylor Tests.....	113
Table 18 - VascoMax 250 Constutive Model in CTH.....	114
Table 19 - VascoMax 250 vs. VascoMax 300 Taylor Tests.....	114

Nomenclature

V	volume
dV	differential volume
ρ	material density
F	force
m	mass
dv	differential velocity
dt or Δt	differential time step
I	impulse
v_o	initial velocity
v_l	final velocity
E_0	initial internal energy source
E_l	final internal energy source
$W_{0 \rightarrow 1}$	work done on a system in going from state 0 to state 1
A	area
c_o	material speed of sound
c_p	plastic wave speed
dA	differential area
x	position
dx	differential length
σ	stress
U	wave velocity
u	particle velocity
$\frac{d\sigma}{d\varepsilon}$	slope of stress-strain curve
E_m	elastic modulus
L	length
ε	strain
$\dot{\varepsilon}$	strain rate
$\dot{\varepsilon}_p$	plastic strain rate
$f()$	function of
τ	pulse duration in striker bar
V_o	striker bar velocity
v_i	striker/incident bar interface velocity
v_{st}	reduce velocity of the striker bar due to impact
σ_{st}	striker bar stress
ε_i	incident strain pulse in SHB

ε_t	transmitted strain pulse in SHB
ε_r	reflected strain pulse in SHB
$u_{1,2}$	displacement of bars in SHB
ε_s	strain specimen in SHB
$P_{1,2}$	forces in SHB

Johnson-Cook Constitutive Equation

A, B, C, m, n	Johnson-Cook coefficients
T^*	homologous temperature
T_{room}	room temperature
T_{melt}	material melting temperature
T	absolute temperature

V_{impact}	velocity of rod at impact on rigid wall in Taylor test
--------------	--

Steinberg-Guinan-Lund Constitutive Equation

Y	yield strength in Steinberg-Guinan-Lund constitutive equation
Y_T	thermally activated component in Steinberg-Guinan-Lund constitutive equation
Y_A	yield strength at Hugoniot Elastic Limit in Steinberg-Guinan-Lund constitutive equation
G_o	initial shear modulus
$A, B, \beta, \varepsilon_b, C_1, C_2, a, \gamma$	Constants in Steinberg-Guinan-Lund constitutive equation
Y_P	Peierl's Stress
$2U_k$	energy required to form two kinks in a dislocation segment

DETERMINATION OF THE CONSTITUTIVE EQUATIONS FOR 1080 STEEL AND VASCOMAX 300

Chapter 1 – Introduction

Extremely high velocity impacts have been of considerable interest in recent years. These tests yield results that affect such research as deep penetrating bombs, armour piercing capabilities and other high velocity. The primary agency to conduct high velocity experiments has been the United States Air Force (USAF), who has spent considerable effort and money to improve the understanding and methodology of very high velocity impacts. To conduct these tests, the USAF has chosen Holloman Air Force Base (AFB) in New Mexico. The relatively dry, flat land and isolated location allows the facility to perform the majority of the advanced very high velocity tests. The general set up of the test area consists of a ten mile long narrow gauge rail system, on which a rocket sled is guided to a target, seen in Figure 1 [1].



Figure 1 - Rocket Sled at HHSTT

In Figure 2, a schematic shows the narrow gauge rail, which is constructed with 1080 steel, and one of the four shoes that attaches the sled to the track [1]. The shoes or slippers are made of VascoMax 300, which is heat treated to create a high strength steel. Currently, the 846th Test Squadron, who operate the Holloman High Speed Test Track (HHSTT), are working to achieve impact velocities of 3048 m/s or approximately 3 km/s. [1] To date, the 846th Test Squadron hold the world speed record of 2884.9 m/s, which was reached in April 2003.

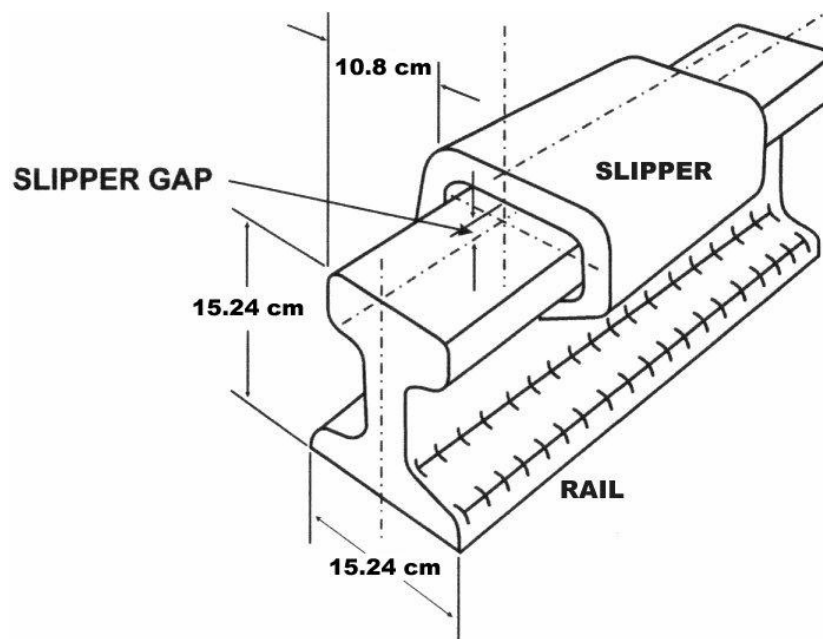


Figure 2 - Slipper/Rail Attachment

During the 846th Test Squadron's effort to reach 3048 m/s, they have encountered a problem known as gouging and are looking for methods to reduce its effects. This phenomenon occurs at velocities in excess of 1.5 km/s and can cause damage to the track in the form of a shallow gouge or loss of the vehicle from total structural failure of the track/sled assembly. Gaps between the shoes and the rail provide the means for

horizontal movement, however, these gaps allow for movement in all three axes in the form of roll, pitch, and yaw. Any of these relative motions can cause gouging when the shoe impacts the rail at very high velocities. Figure 3 presents a typical gouge encountered at Holloman. [1]

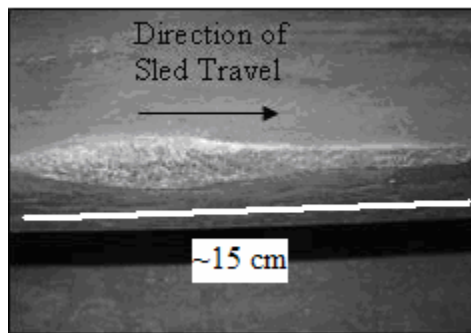


Figure 3 – Gouge Section

Laird [2] provides a more scientific explanation, stating that gouging occurs “when inertial forces are so great that the materials exhibit fluid like behavior. Shock induced pressure creates a region of plasticity under the location of impact. Tangential motion of one body with respect to the other deforms or shears material at these points and results in deformation of the parallel surfaces that impinge on each other in a continuous interaction.” In the gouging case at Holloman AFB, the shoe initiates the gouging process by forming a ridge of material on the rail before the contact point and proceeds to develop a dramatic drop in the actual gouge. As the shoe rebounds off of the rail, the gouge becomes shallower and ends with complete separation of the rail/shoe assembly. Common to most gouges is a teardrop shape approximately 15.0 cm long by 6 inches deep. A diagram of a common gouge is presented in Figure 4. [3]

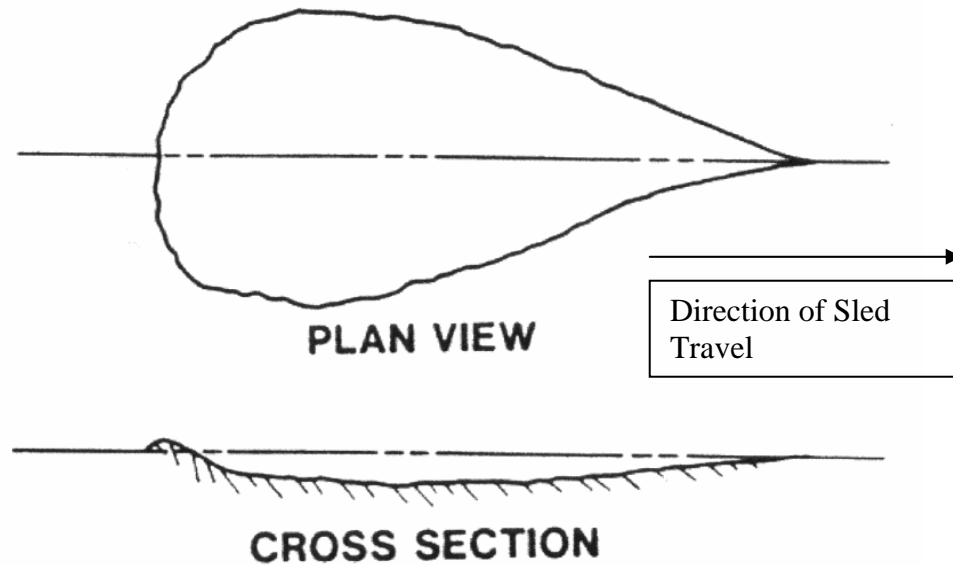


Figure 4 - Schematic View of Gouge

With gouging process occurring at velocities in excess of 1.5 km/s horizontally to the track, Hooser [4] set out to understand the vertical component of velocity's effect on bringing about the development of the gouge. Using the Dynamic Analysis and Design System (DADS), Hooser found that vertical velocities were around 1-2 m/s when simulating a test run at 1.5 km/s. From this information, Hooser showed that the HHSTT experienced gouging from impacts of the shoe at angles near 0.03 degrees.

The interactions between the shoe and the rail have been studied by Laird and Szmerekovsky analytically through the use of the Sandia National Laboratory hydrocode CTH. Both works have provided a greater understanding of the gouging phenomena and the physics involved during the gouging process, but the Szmerekovsky model has been accepted as the standard due to his use of actual test sled conditions. However, neither of these models has been experimentally verified, due to their complexity. To solve this, Rickard developed a simplified gouging model that could be experimentally verified

through compressed gas gun tests at Wright-Patterson AFB. In his model development, Rickerd used CTH to model a simple direct impact test known as a Taylor test to verify future CTH parameters. Rickerd's model is not an entirely accurate simulation of the gouging at HHSTT, due to the lack of a constitutive model for both VacoMax 300 and 1080 steel. To provide a more meaningful model of the gouging process and therefore a better understanding of the gas gun tests at Wright-Patterson, a constitutive model explaining the behavior of both steels at high strain rates and temperatures is needed.

Chapter 2 - Background and Theory

2.1 Conservation Equations

Mechanics, dynamics and their associated areas of study can be explained by three general laws. These three laws of conservation are the conservation of mass, the conservation of momentum, and conservation of energy. The laws of conservation turn out to be highly important when inertia is evident in the problem being studied. Inertia is relevant to this work due to the stress waves formed in the materials from both the Taylor test and Split Hopkinson Bar test, and are provided here for completeness.

In a given volume of material, the conservation of mass states that mass cannot be created or destroyed.

$$\int_V \rho dV = \text{constant} \quad (1)$$

In this mathematical expression, ρ is density and V is the volume of the material.

The second law of conservation dictates that momentum must be conserved in a system. One way of expressing the law is that force must equal the mass of the object multiplied by its acceleration. This can be shown as,

$$F = m \frac{dv}{dt} \quad (2)$$

where F is the force applied to the object, m is the mass acted upon, v is the velocity of the mass, and t is the time of the event. As stated before, the conservation of momentum can take on many forms, including one defined by the mass's velocities. Both the Hopkinson Bar and Taylor tests utilize velocity to produce results that allow the understanding of a material's properties; hence a form of conservation of momentum in terms of velocity is very useful. Taking Equation 2 and multiplying both sides by dt and integrating over a period of time yields,

$$I = \int F dt = \int m dv = mv_f - mv_o \quad (3)$$

where I represents the impulse applied over some period of time by the applied force, v_f and v_o are the initial and final velocities of the mass. Equation 3 defines the conservation linear momentum as the change of momentum over some period of time.

The third equation of the law of conservation is the conservation of energy. It takes the following form when written for a set of j masses as,

$$\sum_j \left(E_o + \frac{1}{2} \rho v_o^2 \right) = \sum_j \left(E_1 + \frac{1}{2} \rho v_1^2 \right) + W_{0 \rightarrow 1} \quad (4)$$

where E is the internal energy source, the $\frac{1}{2} \rho v^2$ terms are the kinetic energy, and $W_{0 \rightarrow 1}$ is the work done on the system. The subscript 0 represents the initial state and the subscript 1 represents the final state.

2.2 Stress Waves in a Continuum

When pressure is applied to a material, stress waves of some magnitude develop and propagate within that material. In very low strain rate problems, such as static or quasi-static testing, these waves can be ignored due to the fact that loads are applied very slowly. However, these stress waves must be accounted for in high velocity impact dynamics studies such as Taylor and Hopkinson Bar tests.

Any instantaneously applied load on a material will cause the development of a stress wave. This process begins by the particles in the local area of the load supporting all of the pressure via local acceleration [1]. These particles that were initially accelerated cause other particles nearby to develop compressive stresses in the form of a wave. Compressive stresses continue to increase as the initial particles move further to accommodate the applied load. Once the applied load is satisfied or equaled by the build up of compressive stresses, the relative motion can stop and the remaining portion of the material will experience the stress wave, via the same process [5]. The law of conservation of momentum dictates that the velocity of these particles is dependent upon the velocity of the impact, but the speed of the stress wave will be shown to be a function of material properties [1].

In the following two subsections, two types of dynamic impacts will be described to understand the effects of impact velocities on stress wave propagation. The first type of impact occurs at low velocities and will cause only an elastic wave to form. At higher velocities, both an elastic wave and a plastic wave will form. The plastic wave trails the elastic wave and will cause permanent plastic deformation in a portion of the material.

To define both of these waves, a simplified Taylor test or uniaxial rod impact test will be used.

2.2.1 Elastic Stress Waves

In order to calculate the elastic stress wave, a case where a static, thin rod will be impacted by a rigid, semi-infinite plate moving with a constant velocity of v_0 . For simplification, this case will only be examined one dimensionally. However, understanding the propagation of a 1-D stress wave in a material is useful in understanding the Split Hopkinson Bar, as will be shown later in this chapter. This velocity is less than the material sound speed c , to ensure that only elastic deformation is obtained. With all mediums, sound waves will propagate with a defined velocity. This velocity for elastic materials will be shown later. Figure 5 depicts the rod impact case.

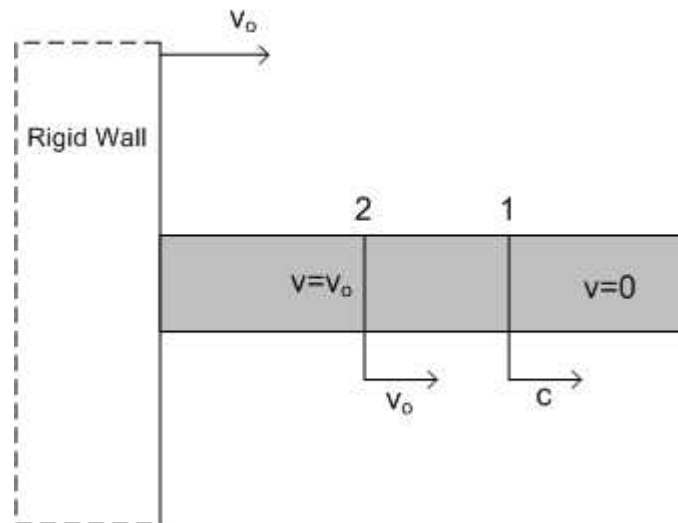


Figure 5- Rod Impact

As stated before, the elastic stress wave will propagate to the right at the material sound speed, while the particles behind the wave will travel at velocity equal to that of the impact velocity. Knowing that the particles behind the stress wave are in motion, a impulse-momentum balance can be shown by,

$$\rho A c \Delta t v_o \quad (5)$$

where $c \Delta t$ is the length of the rod which is moving with a particle velocity of v_o and A is the cross sectional area of the rod. Therefore $A c \Delta t$ is the volume of material moving with a particle velocity of v_o . [1]

With the momentum defined, an expression for the impulse acting on the material is needed to define the elastic stress wave. From basic physics, an impulse is defined as a force applied over a period of time. Knowing that,

$$\sigma = \frac{P}{A} \quad (6)$$

where σ is the compressive stress due to the stress wave, P is the force acting on the material, and A is the cross-sectional area the force is acting over, a solution for the impulse can be found in terms of stress times the area for a given amount of time. This gives,

$$\sigma A dt \quad (7)$$

Equating the two equation above through the use of the conservation of momentum, allowing for a infinitesimal time step, and dividing out both the area and time step, the elastic stress wave can be defined as,

$$\sigma = \rho c v_o \quad (8)$$

where c is the material sound speed.

Understanding the speed of sound for a material is essential to obtain results for both the Taylor and Hopkinson Bar test. The rod impact case allows a function defining the material sound speed to be determined and will be applicable for both of the tests. From the rod, an infinitesimal element of area experiences the passage of the stress wave, as shown in Figure 6.

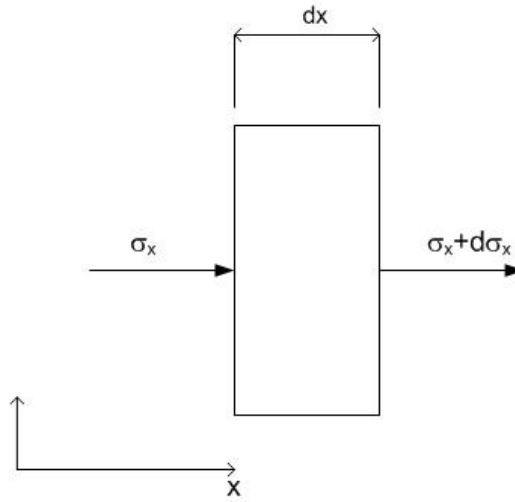


Figure 6 - Material Element

From Figure 6, tension is assumed to be in the positive x direction, yielding $-\sigma_x$ for the left side of the area and $\sigma_x + \frac{\partial \sigma_x}{\partial x}$ for the right side. Applying the conservation of momentum to the infinitesimal area A ,

$$A(-\sigma_x)dt + A\left(\sigma_x + \frac{\partial \sigma_x}{\partial x}\right)dt = (\rho A)dv \quad (9)$$

where the entire left hand side of the equation represents the impulse from the stresses on the left and right sides of the area, and momentum imparted over a time step on the right side of the equation. To simplify this expression, Adt can be dropped from both sides to give,

$$\frac{\partial \sigma_x}{\partial x} = \rho \frac{dv}{dt}. \quad (10)$$

To obtain the material sound speed purely in terms of material properties, velocity must be related to position. Knowing the basic equations of strain and velocity as,

$$\varepsilon = \frac{\partial u}{\partial x} \quad \text{and} \quad v = \frac{\partial u}{\partial t} \quad (11)$$

it can be shown that

$$\frac{\partial \varepsilon}{\partial t} = \frac{\partial v}{\partial x}. \quad (12)$$

From equation 10 and 12, the one-dimensional wave equation can be developed if stress assumed to be entirely dependent on strain; yielding,

$$c^2 \frac{\partial^2 u}{\partial x^2} = \frac{\partial^2 u}{\partial t^2} \quad (13)$$

where

$$c^2(\varepsilon) = \frac{d\sigma/d\varepsilon}{\rho}. \quad (14)$$

Since this case is being conducted as an elastic impact, then stress over strain in equation 14 is merely the elastic modulus or Young's Modulus of the material in the linearly elastic region. Hence,

$$c = \sqrt{\frac{E_m}{\rho}} \quad (15)$$

where E_m is the elastic modulus of the material and ρ is the density of the material. [2]

With the propagation of the elastic stress wave defined both in terms of its magnitude and velocity, the case of the free end of the impact rod must be examined. This analysis will later be important for explaining the stress wave in Taylor tests conducted in CTH and the application of the Hopkinson Bar to conduct tension tests. Using the same impact rod case as stated earlier and the equations developed for the elastic stress wave, an understanding of the stress wave interaction with the free end of the rod will be achieved.

Before impact the rod is moving with constant velocity v_o and there is no internal stress. The moment the rod impacts the rigid, semi-infinite wall, a stress wave is formed and begins to propagate down the rod at the material sound speed define in equation 15. As before, the particles behind the wave will have a magnitude of stress shown in equation 8. In order for the continuity to be maintained at the boundary of the rod and the wall, velocities of both objects must be equal [1]. Since the wall is rigid, this

forces the rod to have zero velocity on the impact end instantaneously, while the free end is still moving with the original velocity. The free end does not experience this abrupt change immediately due to the fact that the information of the stress wave takes a finite time to travel the length of the rod. Figure 7 depicts the different conditions at either end of the rod [1]. The fact that a time delay exists between when the left side of the bar experiences the stress wave and when the right side experiences the stress waves is important to the Hopkinson Bar test and will be described later.

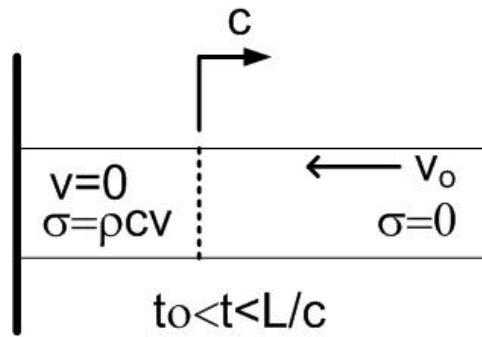


Figure 7 - Rod Impact Experiment before Reflection

Once the stress wave has reached the free end of the rod, the rod is now under constant particle compressive stress and has temporarily stopped due to the kinetic energy of the applied load converted into internal strain energy. [1] The time it takes the stress wave to reach the free end from the point of initial impact is a simple calculation if the material sound speed is known. It is defined as $t = L/c$, where L is the length of the rod. In relation to the Hopkinson Bar test, knowing the time it takes the wave to travel between two points is vital for correct experimental setup and data collection. This will be discussed later.

At the free end of the rod, the stress wave experiences a physical law defined in any basic structural course or text. A free end by definition cannot support stress and therefore the resultant force in the free end of the rod must equal zero. The only mechanism that can exist at the free end is a reflection of the stress wave back towards the impact end. During the reflection, the oncoming stress wave is canceled out by the reflected stress wave, allowing zero stress at the free end and doubling the surface velocity [6]. In this reflection, the sign of the stress changes from compression to tension. Here again is another important characteristic of stress waves in materials that gave rise to the Hopkinson Bar test, particularly the tension test. Figure 8, provided by Rickerd, depicts the propagation of the reflected tension stress wave down the rod, while the rod continues to move away from the impact point [1].

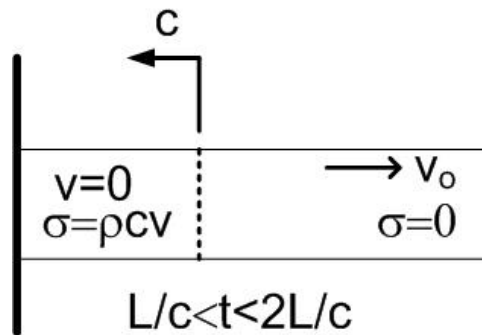


Figure 8 - Rod Impact Experiment after Reflection

The eventual end game to this reflection of stress waves, is that the impacted end will break from the rigid wall. It will be shown later that for this work's analysis, the Hopkinson Bar test is not concerned with rebounding and the CTH model of the Taylor test will not require separation to generate proper deformation. This is true due to the

slide condition utilized in CTH and the knowledge of approximate impact duration of the Taylor specimen. This will be explain in more detail in chapter 4.

The Lagrangian diagram provides another approach to understand the stress wave interactions in a material. By plotting the relative position of the wave as it moves down the length of the material over a period of time, the Lagrangian diagram provides a visual representation of the reflection occurring. Figure 9 depicts the rod's stress waves from initial impact to release from the rigid wall [1].

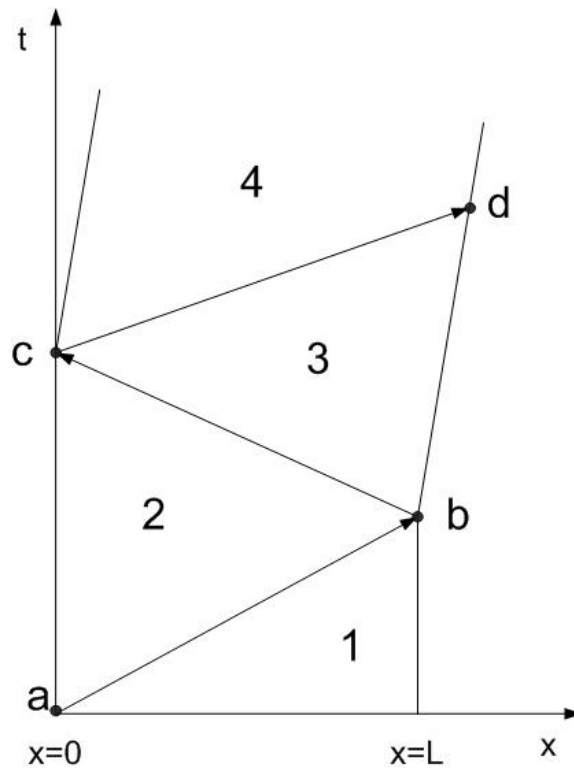


Figure 9 - Lagrangian Diagram for Rod Impact Problem

From the diagram, time is increasing in the positive y-axis and the rod's length is described along the x-axis. In the bottom right triangle, region 1, the rod is unstressed and traveling towards the wall. At impact the compressive stress wave travels

from $x=0$ to the right until it hits the free end at $x=L$ or point b. Here, as stated before, the free end dictates zero stress and results in a reflected tension wave traveling back to the right. The particle velocity is zero in region 2. At point C, a compression wave is reflected from the impact end due to the wall and the rod not being physically joined in any manner.

2.2.2 Plastic Stress Waves

Understanding the elastic behavior of a material is fundamental for any study that is investigating the characteristics and properties of that material in a multitude of different scenarios. However, the elastic portion of the stress-strain relation only defines low strains and cannot explain the linear and non-linear effects at higher strains. This segment of higher strains is known as the plastic region. Again, this will be a 1-D case for similar reasons as stated for the elastic study. When a material is quasi-statically or dynamically loaded, the stress-strain curve at some point will discontinue its linearly elastic behavior and the material will become permanently deformed. This plastic deformation occurs at a point known as the yield stress or elastic limit. The plastic region will be the main focus of this work in both the Taylor test and the Hopkinson Bar test. Plastic deformation will yield measurable changes in dimensions of specimens in Taylor tests and will allow the construction of a constitutive model from the plastic curves obtained from Hopkinson Bar tests.

As discussed earlier, the plastic stress wave follows the initial elastic stress wave as particle stress approaches the yield stress for the material. In addition, the plastic

stress wave travels at a slower velocity than that of the elastic wave. This gives rise for the need to redefine the material sound speed in terms of the plastic stress wave as,

$$c_p = \sqrt{\frac{E_p}{\rho}} \quad (16)$$

where c_p is the plastic wave speed and E_p is the slope of the stress strain curve in the plastic region. In addition the magnitude of the stress wave will change and is given by,

$$\sigma_p = \rho c_p v_o \quad (17)$$

where σ_p is the plastic stress wave magnitude.

Two different theories exist on the behavior of materials when they undergo plastic deformation. The first theory, called rate-independent theory, assumes that strain rate does not affect the stress-strain curve at any strain and that a single bilinear curve explains the entire stress-strain development in a material. Equation 16 comes from the rate dependent theory and when coupled with the Equation 15, describing the elastic region, a diagram such as Figure 10 is produced [7].

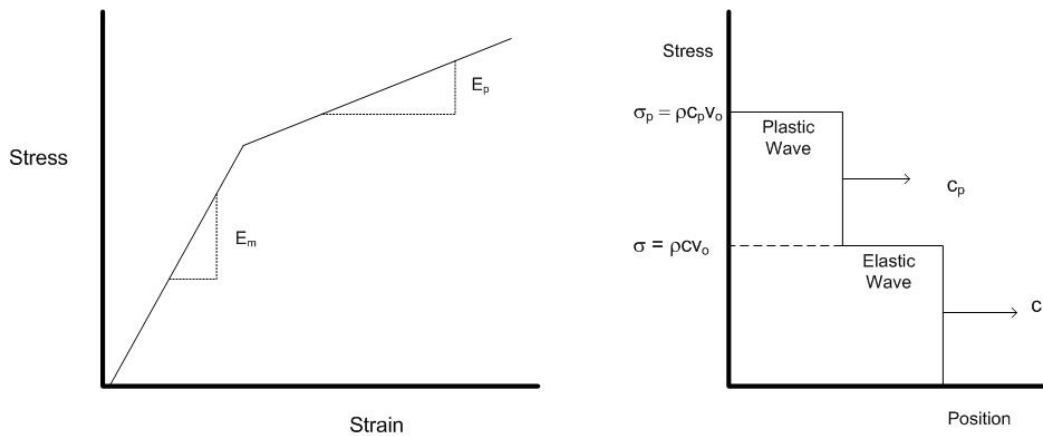


Figure 10 - Bilinear Stress-Strain Curve and Corresponding Wave Profile

Again, the plastic wave is shown to follow the elastic wave, while traveling at lower velocity.

For the most part, the plastic region exhibits nonlinear behavior. Equation 18 solves this by defining the slope of the plastic region in terms of a specific point in,

$$c_p = \sqrt{\frac{\partial \sigma / \partial \epsilon}{\rho}} \quad (18)$$

where $d\sigma/d\epsilon$ is the slope of the stress-strain curve at a given strain. Given this form of plastic wave speed, it can be shown that for some materials, a stress point will be reached where the plastic slope will be greater than that of the elastic slope. The result of this will cause the plastic wave speed to be greater than that of the elastic wave speed, causing a shock to form when the plastic wave reaches the elastic wave. Figure 11 depicts this shock event [7].

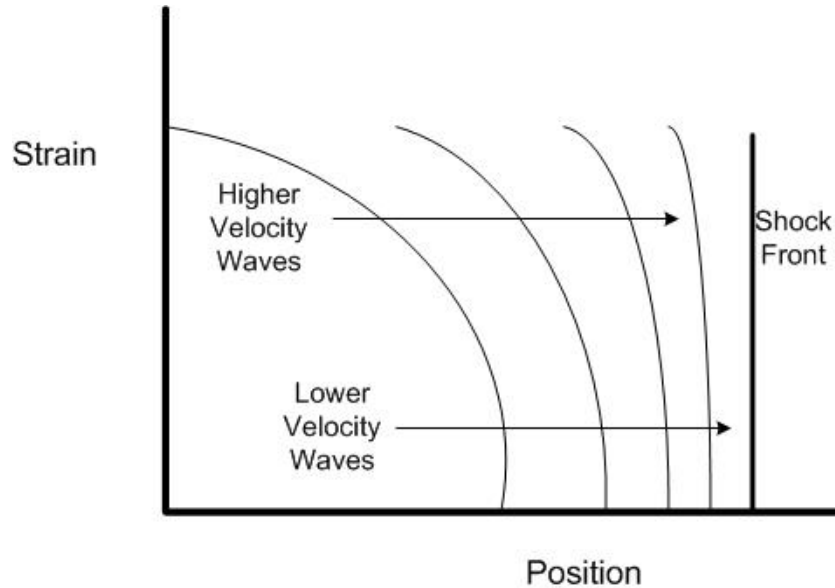


Figure 11 - Shock Formation

The second theory of plastic stress waves, states that the wave propagation is dependent on the strain rate developed by the impact. This theory is known as the rate-dependent theory and more accurately approximates the true plastic stress-strain curve found in experimentation. Figure 12 shows how higher strain rates will lead to greater values of stress for a given strain in a material.

STRAIN RATE SENSITIVE FLOW STRESS BEHAVIOR

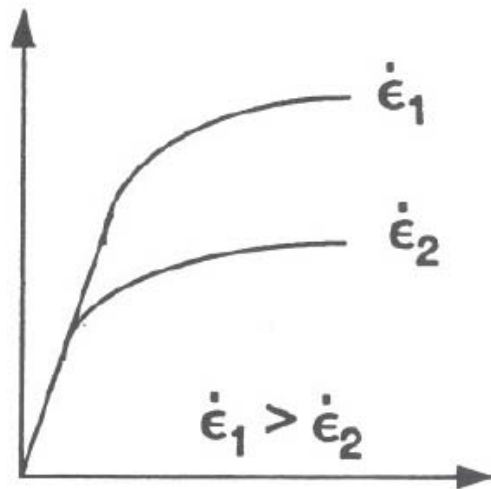


Figure 12 – Flow Stress Behavior at Different Strain Rates

From Figure 12, the slope of the elastic region or elastic modulus, remains the same for both strain rates, however a higher yield stress is reached for $\dot{\epsilon}_1$. Higher flow stress is a result of increasing strain rate [6]. This higher stress denotes an overstress, which Malvern first attempted to explain the effect of higher strain rates on stress in,

$$\sigma = f(\varepsilon) + \ln\left(1 + b \dot{\varepsilon}_p\right) \quad (19)$$

where $f(\varepsilon)$ is the stress in a quasi-static test and $\dot{\varepsilon}_p$ is the plastic strain rate.

The overstress is defined as $\sigma - f(\varepsilon)$, and is the difference between a stress at a strain rate greater than quasi-static and a quasi-static test.

In this work, plastic deformation dependent on strain rate will be utilized to understand the strain rate sensitivity of 1080 steel and Vascomax 300. From the split Hopkinson Bar test data, it will be shown that higher strain rates will affect the characteristics of the plastic region.

2.3 Split Hopkinson Bar

The split Hopkinson Bar (SHB) or Kolosky apparatus was created to enhance the understanding of mechanical properties of materials at high strain rates due to the lack of reliable techniques. The original SHB was utilized to examine material properties at higher strain rates while in compression. As described by Nicholas [8], a specimen is placed between two long bars and “a compressive pulse, generated by impact of a third bar..., propagates down one of the long bars and through the specimen into the second bar. The bars remain elastic, although the specimen is deformed into the inelastic region because of the impedance mismatch.” Impedance mismatch is defined as the area difference between the bars and the specimen. Testing of material properties of strain rates exceeding $10^4 s^{-1}$ have been documented using the SHB, but some contend the

validity of the results at these strain rates. For this work, strain rates will not exceed 1500/s.

To understand the development of the pulses in the SHB, the interaction between the striker and the incident bars needs to be defined. Two interface conditions exist between the striker and incident bars. First, continuity must be satisfied by requiring the two bars to remain in contact during loading. Like the direct rod impact, the one-dimensional wave equation will be used to solve for the stress waves produced.

With equation 8, the velocity of the striker bar can be assumed as V_o before it impacts the incident bar. By defining the velocity at the striker/incident bar interface as v_i , we can show that,

$$v_i = V_o - v_{st} \quad (20)$$

where v_{st} is the reduce velocity of the striker bar due to impact .

The second condition existing at the interface states that the forces across the interface must be equal [9]. These forces are represented as the striker bar compressive force, P_{st} , and the incident bar force, P_i . As in most SHB tests, the striker and incident bars are constructed from the same material, thus allowing the velocity and stress relationships to be,

$$v_{st} = v_i = \frac{1}{2}V_o \quad (21)$$

$$\sigma_{st} = \sigma_i = \frac{1}{2} \rho c_o V_o \quad (22)$$

From the direct impact case mentioned earlier, it is known that a compressive pulse in the striker bar will reach the free end and be reflected to satisfy the zero stress condition at the free end. This mechanism then can be used to determine the pulse duration, τ , in the striker bar. It will take the compressive pulse $t = L / c_o$ to reach the free end and the reflected tension pulse will therefore require the same time period to zero out the stress and velocity of the bar. Hence the pulse duration is,

$$\tau = \frac{2L}{c_o} \quad (23)$$

and will take the form as a square stress pulse. The amplitude of this pulse is dictated by the striking velocity and the duration is controlled by the striker bar length [9]. This interaction between the striker and incident bars will be the same for any variation of the SHB.

Over the years, many researchers have investigated the potential use of the SHB to generate tensile tests at high strain rates. An example of a tensile Hopkinson Bar set up uses a normal compression technique with a hollow tube. In this tube is a joint that connects an inner rod to the tube and the specimen is placed in between the inner rod and an outer rod. Figure 13 provides a diagram of this test [10].

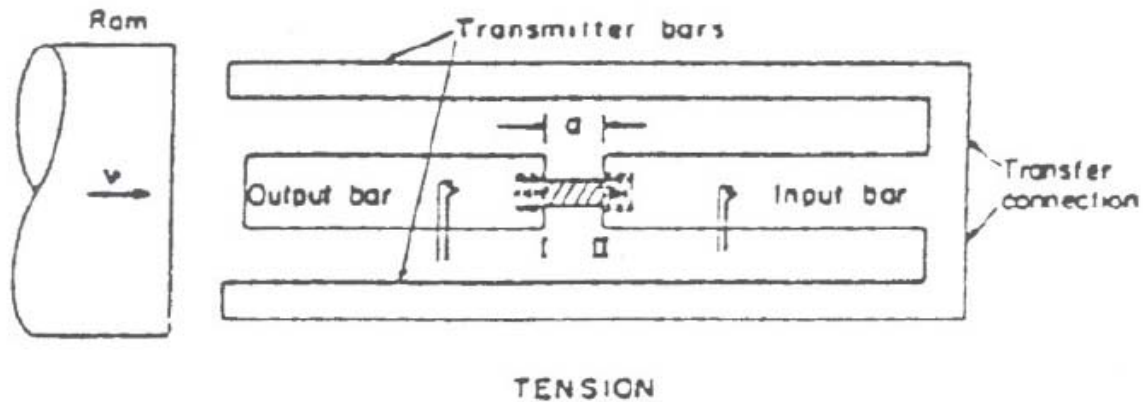


Figure 13 - Tension Split Hopkinson Bar

One set back to this tension test is that it cannot produce tensile waves with short rise times due to wave dispersion at the joint [8].

To overcome this issue and increase the strain rate capabilities of the test past 1000/s, a tensile version of the split Hopkinson bar test has been developed. The tensile SHB has been used very successfully for a multitude of metals since its induction into the field [8]. This work will utilize this experiment to conduct the tensile tests and will be explained in specific details later. The basic operation of the tensile SHB is exactly like the compression model described earlier, except that the usage of pulses within the system is different.

As mentioned before, understanding the stress wave propagation and reflections is vital to obtaining data that is accurate to the test at hand. Figure 14 below is a depiction of the wave interactions in the specimen [11]. This diagram has the incident bar being struck from the left.

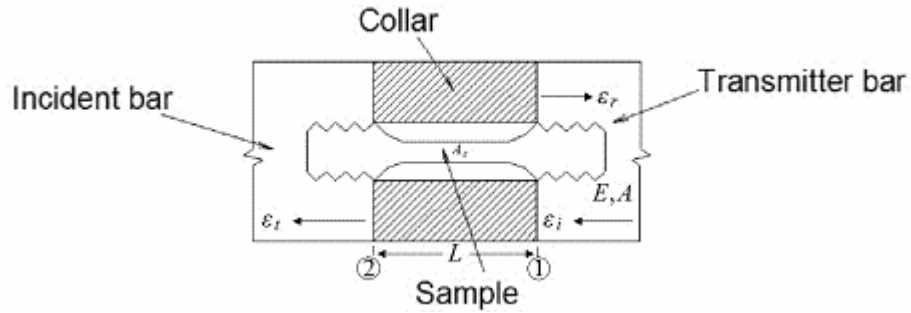


Figure 14 - Tensile SHB Wave Propagation

For a tensile test to be conducted, a compression wave has to be reflected off the transmitter bar. This reflected wave will be designated ϵ_i or the incident wave that will pass through the specimen. Figure 15 shows how waves travel in the two rods and the specimen connected between them for a tensile SHB test [8].

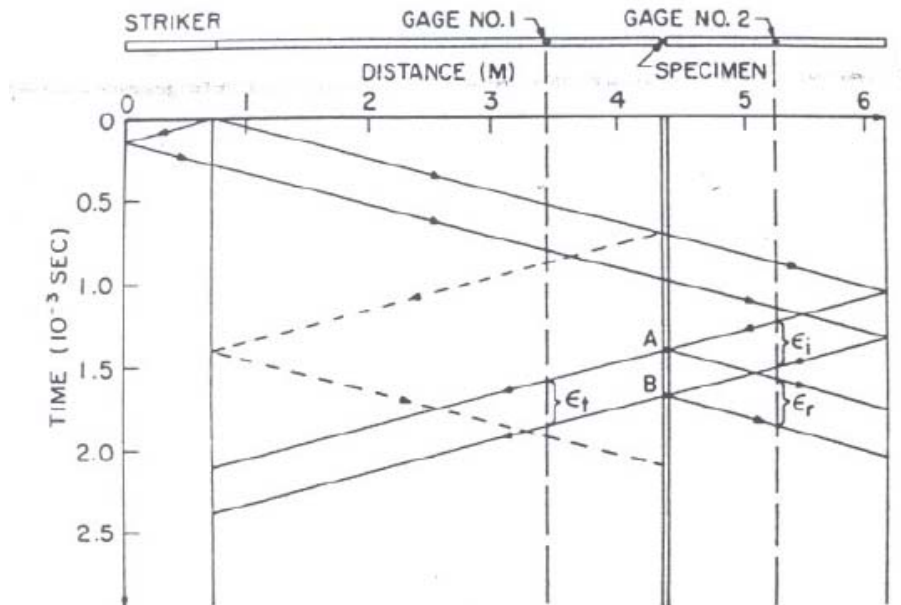


Figure 15 - Lagrangian Diagram for Tensile SHB

In this diagram, the incident bar is twice as long as the transmitter bar. When the striker bar impacts the incident bar, a stress wave will propagate at the material sound speed through the incident bar. In order for the specimen not to undergo compression stress from the wave, a collar of made from the same material as the bars is placed around the specimen. This allows the pulse to travel through the specimen without any significant loss of wave intensity due to only elastic compression being felt by the specimen. The stress wave will then reflect as it reaches the free end of the transmitter bar. As explained earlier, the free end cannot support stress and causes a compression wave to reflect as a tension wave. This tensile wave now produces the tensile data to be obtained. Once the wave has traveled back through the transmitter bar, it will reach the specimen and the collar, which is loose from the first incident wave. At point A in the diagram, a portion of the tension wave will pass through the specimen and be registered on a strain gage on the incident bar. This is the transmitted strain pulse, ε_t . The remaining portion of the tension wave will reflect as a compression wave and will be measure on a strain gage positioned on the transmitter bar. This pulse is the reflected pulse, ε_r . From the strain data at these two points, a stress can be calculated. With a visual understanding of the waves in the tensile SHB, relationships can be introduced to find the stress experienced in the specimen.

From the direct rod impact test shown earlier, a one-dimensional wave equation was developed and is restated here for convenience,

$$c^2 \frac{\partial^2 u}{\partial x^2} = \frac{\partial^2 u}{\partial t^2} . \quad (24)$$

Knowing that,

$$\varepsilon = \frac{\partial u}{\partial x} \quad (25)$$

and,

$$\sigma = E\varepsilon \quad (26)$$

and solving for the Equation 19, the following displacements at ends 1 and 2 of the specimen in Figure 15 can be found as,

$$u_1 = \int_0^t c_o \varepsilon_1 dt \quad (27)$$

$$u_2 = \int_0^t c_o \varepsilon_2 dt \quad (28)$$

where c_o is the elastic wave speed, $\varepsilon_{1,2}$ is the strain at points 1 and 2 of the specimen.

Equations 27 and 28 can be rewritten to utilize the known wave reflections occurring in the SHB by,

$$u_1 = c_o \int_0^t (\varepsilon_i - \varepsilon_r) dt \quad (29)$$

$$u_2 = c_o \int_0^t \varepsilon_t dt \quad (30)$$

Using equation 25, the strain in the specimen can be determined from,

$$\varepsilon_s = \frac{u_1 - u_2}{L} \quad (31)$$

where L is the gage length of the specimen. This is important to note, because the specimen was milled down from the threading to the test diameter, constituting the gage length. A diagram of the test specimen is given in the chapter 3 of this work. Again, displacement can be expressed in terms of the transmitted pulses and allow a strain for the specimen to be defined as,

$$\varepsilon_s = \frac{c_o}{L} \int_0^t (\varepsilon_i - \varepsilon_r - \varepsilon_t) dt \quad (32)$$

With the strain in the specimen defined in terms of all three pulses in the SHB, it is needed to reduce the number of variables to one pulse. Looking at the pressures in the specimen's ends yields,

$$P_1 = EA(\varepsilon_i + \varepsilon_r) \quad (33)$$

$$P_2 = EA\varepsilon_t \quad (34)$$

If it is assumed that $P_1 = P_2$, meaning that forces on both ends of the specimen are equal, then using equation 33, 34, and 32 it can be shown that,

$$\varepsilon_t = \varepsilon_r + \varepsilon_i \quad (35)$$

$$\varepsilon_s = \frac{c_o}{L} \int_0^t (\varepsilon_t - \varepsilon_r - \varepsilon_r - \varepsilon_t) dt = \frac{-2c_o}{L} \int_0^t \varepsilon_r dt \quad (36)$$

Knowing the cross section area of the specimen, A_s , and the area of the bars, A, the stress and strain rate in the specimen are found to be,

$$\sigma_s = E \frac{A}{A_s} \varepsilon_t \quad (37)$$

$$\dot{\varepsilon}_s = \frac{-2c_o}{L} \varepsilon_r \quad (38)$$

An important note is that the stress, strain, and strain rate relations are average values and all are calculated with the assumption of uniaxial stress-state [7].

An understanding of the methods needed to obtain a material's properties, both elastic and plastic at varying strain rates, has been developed and now can be used to

explain the dynamic response of that material. To do this, a constitutive model that can approximate the material's characteristics based on strain rate, temperature and other variables needs to be constructed from the stress-strain curves.

2.4 Constitutive Equation

As stated before, the stress-strain relation in most metals produces two distinct area of response to a loading. The elastic region, with its linear curve is relatively easy to define and reproduce for estimation of loading effects. Hooke's Law is a common model used to understand the stress-strain curve below the yield stress. It is defined here as,

$$\sigma = f(\varepsilon, E_m) \quad (39)$$

where σ is the stress, ε is the strain, and E_m is the modulus of elasticity. In this work, Hooke's Law is only applicable to the quasi-static tests conducted on VascoMax 300 and 1080 steel, but it provided vital results necessary to construct a more complete constitutive model.

Once a material is loaded beyond its yield point, the effects of dynamic loading must be accounted for. This is done by including strain rate in the stress function, shown here as,

$$\sigma = f\left(\varepsilon, \dot{\varepsilon}, E_m\right) \quad (40)$$

where $\dot{\varepsilon}$ is the strain rate desired for the test. Not all materials respond in a similar fashion to varying strain rates, so a strain rate sensitivity parameter is employed to accurately predict the plastic curve for a given material. The constitutive equation used in this work defines this parameter. It should be noted that determining the appropriate constitutive model for a given material is usually a semi-empirical process, which requires an understanding of the physical mechanisms controlling plastic deformation and the use of experimental data [12].

For this study, the Johnson-Cook constitutive equation was chosen to model the plastic curves evident in 1080 steel and VascoMax 300. Its relatively basic break down of the variables controlling the analysis of dynamic loading and its wide use were ideal in verifying the results this work was trying prove. In addition, this model already existed in CTH and allowed an easy implementation of the coefficients from the equation to be input into the Taylor test model. Johnson and Cook themselves have been successful in describing Taylor tests for a variety of materials using a Lagrangian material dynamics code EPIC-2, in which their constitutive model was utilized [13]. The Johnson-Cook constitutive model is most common expressed as,

$$\sigma = (A + B\varepsilon^n)(1 + C \ln \dot{\varepsilon}_p)(1 - T^{*m}) \quad (41)$$

where A is the yield stress, B is the strain hardening factor, n is the strain hardening index, C is the strain rate sensitivity parameter, T* is the homologous temperature, and m

is the thermal softening coefficient. T^* is defined below and accounts for heating of the tested material before the dynamic loading. In chapter 3, the heating of specimens will be described. Equation 42 defines T^* as,

$$T^* = \frac{T - T_{room}}{T_{melt} - T_{room}} \quad (42)$$

where T_{room} is the room temperature during the test and T_{melt} represents the known melting temperature of the material [5].

From equation 41, a piecemeal approach can be taken to determine the coefficients of the Johnson-Cook constitutive model. The first set of brackets contain coefficients that are only developed through analysis of a quasi-static stress-strain curve. As defined before, A is the yield stress and can be readily determined from a percent offset of some accepted value. It should be noted that the practice of .2% offset for determining the elastic limit of a material was based purely on the need to understand Cooper's elastic behavior and does not imply that all metals will exhibit such percent offset. This will be discussed further in the Methodology section. The B and n coefficients complete the quasi-static analysis by fitting the plastic region of the curve. Using a log fit of the plastic stress and strain will yield the necessary values. The strain rate sensitivity parameter, C , is found by taking varying strain rates at room temperature. The final value needed to complete the model is the thermal softening coefficient, m , which is acquired from data taken at varying strain rates and temperatures. A more complete analysis of the coefficients for 1080 steel and VascoMax 300 steel is provided subsequently.

Like any curve fit of data, the Johnson-Cook model does have disadvantages. One minor disadvantage is that strain rate sensitivity parameter and temperature are independent of one another. This is not the case in real world experimentation. However, by being uncoupled, the piecemeal construction of the equation is possible. A second set back to the Johnson-Cook model is that it is a mathematical expression used to fit data and has no justification through physics. [1] This work however, shows that these disadvantages are outweighed by its ability to readily produce close fits to the experimental data.

Chapter 3 – The Use of the Split Hopkinson Bar Technique in Evaluating the Johnson-Cook Constitutive Model for 1080 steel and VascoMax 300

3.1 Tension Split Hopkinson Bar Technique

With the basic fundamentals of SHB defined in chapter 2, an examination of the experimental setup and techniques used at the University of Dayton Research Institute (UDRI) can be shown. UDRI and its research staff are very experienced in material properties, especially testing done in the high velocity regime and have completed many research projects for the government and military. The SHB used at UDRI consists of a striker bar and two pressure bars mounted and aligned longitudinally in bearings that support the bars in a horizontal plane [14]. All three bars are .5 in (12.7mm) in diameter and made of Inconel 718. The striker bar is .76 m long and is fired from a gas gun. This impacts an incident bar, with a length of 3.56 m. The transmitter bar is 1.82 m long. Figure 16 is a schematic of the SHB setup at UDRI [14].

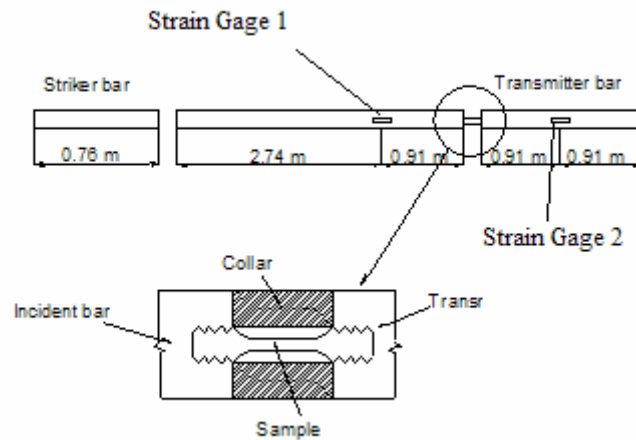


Figure 16 - UDRI Split Hopkinson Bar Schematic

The test specimens for both Vascomax 300 and 1080 steel were machined by HHSTT. The 1080 steel specimens were created from a stock rail section from the manufacture. The Vascomax 300 specimens were heat treated developed in the same manner that the shoes of the vehicle are created through heat treatment of the steel. Figure 17 displays the specimen's dimensions for both steels.

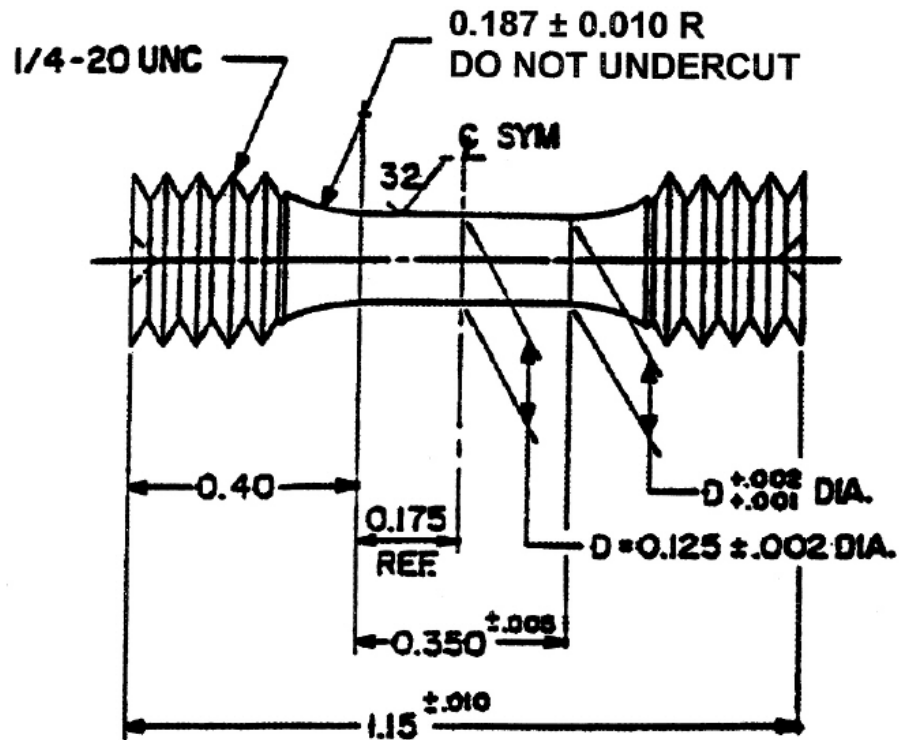


Figure 17 - SHB Specimen Dimensions

It is important to note here that the pulse duration, as stated in chapter 2, is

$$\tau = \frac{2L}{c_o} \text{ and ensures that the compression and tension waves in the SHB won't cancel out.}$$

Knowing that the elastic modulus for Inconel 718 is $1.95 \times 10^5 \text{ MPa}$ and the density is 7900 Kg/m^3 , the material sound speed can be found as $4.97 \times 10^3 \text{ m/sec}$. From this the pulse duration becomes $306 \mu\text{sec}$. In addition, the incident bar has been chosen to be relatively long compared to the others to ensure that the strain gauges do not detect any small wave reflections at from gaps between the collar and the bars [8]. However, care has to be taken in aligning the collar with the bar, so that any wave dispersion is minimal. Below is a picture of the actual SHB used at UDRI for this research.



Figure 18 - UDRI Split Hopkinson Bar Apparatus

The experimental method used by UDRI is consistent with accepted practices for determining the stress-strain relation. Two strain gauges were placed on the incident bar and the transmitter bar, equidistance from the specimen/bar boundary on either side of the specimen. For this setup, the distance was .91 m. The strain gage placement was determined to be .91 m from the specimen to ensure that the transmitted and reflected waves were time coincident and due to the transmitter bar needed to be half the length of the incident bar [8]. Figure 19 depicts the position and orientation of one of the strain gauges on the bar.

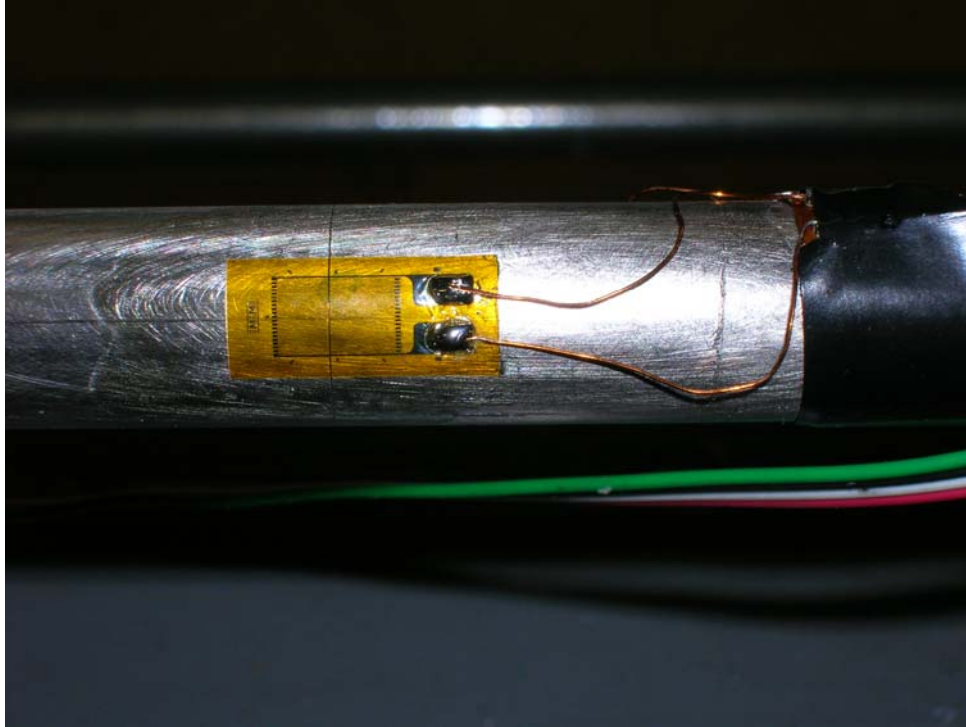


Figure 19 - Strain Gage on SHB

All three strain pulses, ε_t , ε_i , and ε_r are record on a dual beam oscilloscope after passing through a amplifier to allow for better amplitude response of the relatively weak strain signal. Both ε_t and ε_r occur at the same time and are recorded by using the chopped mode of the oscilloscope preamplifier. The chopped mode is when a small portion of one channel, followed by a portion of the other channel, is repeatedly applied to the amplifier during the same cycle of the sweep. Figure 20 shows the oscilloscope and amplifier used a UDRI. A typical strain-gage trace is shown in Figure 21.



Figure 20 - UDRI Oscilloscope/Amplifier Setup

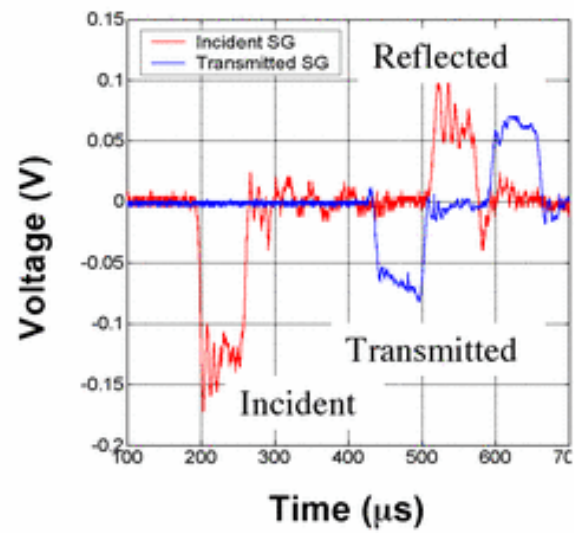


Figure 21 - Sample Strain Gage Trace

The trace in Figure 21 is for a pressure SHB and not a tension SHB. A trace of the UDRI data was not available, but this sample is applicable. The incident wave is detected first in strain gage 1 on the SHB, followed by the transmitted wave detected in strain gage 2 and the reflected wave detected in strain gage 1.

When varying the strain rates through the experimentation, as dictated by the Johnson-Cook model, a relationship between the striker bar velocity and strain rate was employed. From equation 38 it is seen that the strain rate is a function of the reflected pulse, ε_r , which is in itself a function of the incident pulse, ε_i and transmitted pulse, ε_t . In chapter 2, it was shown that the higher velocities of the striker bar, the greater the compressive stress would be. Years of experience with the SHB have given the researchers at UDRI the ability to understand what velocities will produce certain strain rates in the specimen. To explain this mathematically, the flow stress in the material is defined in equation 42 and restated here as,

$$\sigma_s(t) = E \frac{A}{A_s} \varepsilon_{(t)}(t) . \quad (43)$$

Assuming that the flow stress is constant, then ε_r can be directly related to ε_i to yield,

$$\varepsilon_i = \frac{1}{2E} c_o \rho V_s \quad (44)$$

where V_s is the velocity of the striker bar [14]. Appendix 1 contains the flow stress values for 1080 steel and VascoMax 300 determined by UDRI. Here it is seen that there are two ways to change the strain rate in the specimen. One way is to increase the

velocity of the striker bar and the other way is to change the specimen gage length. At UDRI, the velocity of the striker bar was increased to produce higher strain rates. Using a compressed air system at the facility, UDRI would charge a pressurized tank at one end of the HSB. From experience, a known pressure could produce a certain velocity for the striker bar and hence given a good approximation of the strain rate to be produced.

Another variable needed to create an understanding of the Johnson-Cook model is temperature. By viewing the effects of temperature on the plastic deformation of the steel, a thermal coefficient, m , could be defined in the equation to satisfy the stress-strain curve under elevated heating conditions. This is important given the very high temperatures seen at HHSTT during gouging. Even though the exact temperature is not known to date, UDRI obtained data in a range of temperature that would allow the construction of a model that could “fit” a larger range of temperature conditions.

To heat the specimens to the desired test temperatures, an induction coil was used. The induction coil is made by Lindbergh/Cycle Dyne and operates on a line power of 240 volts obtained from a step up transformer rated at 5000 VAC [14]. Flowing water continuously cooled the induction coil. In Figure 22, the induction coil is seen surrounding the specimen and collar.

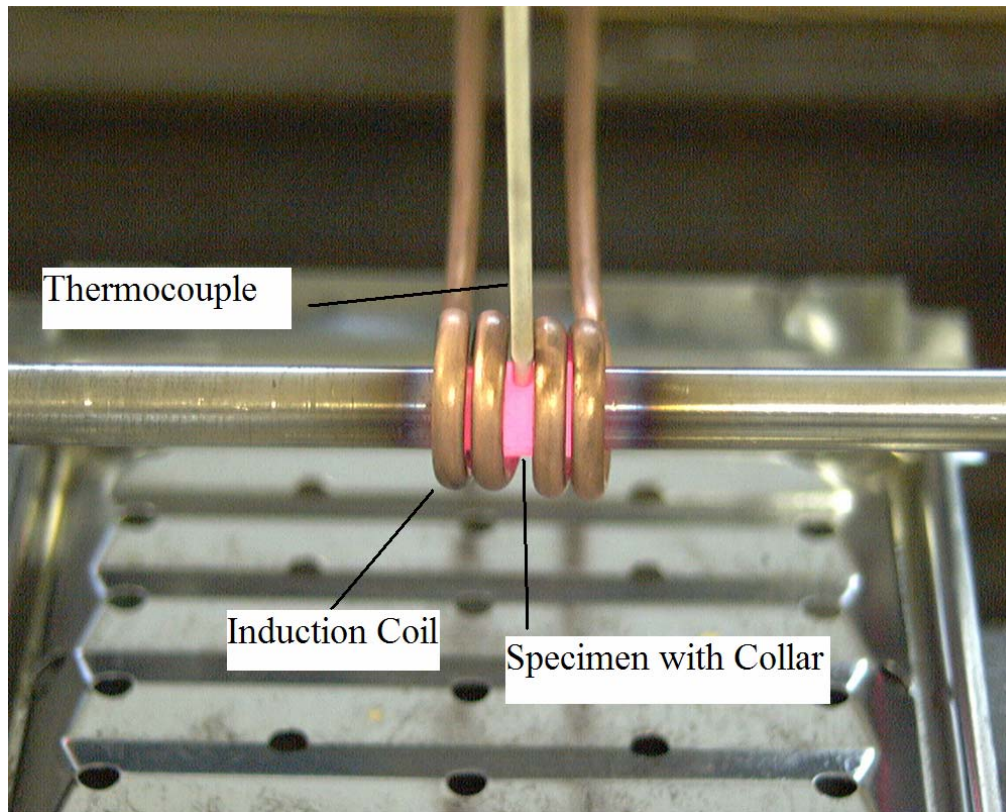


Figure 22 - Induction Coil Apparatus

Before conducting a given experiment and having secured the specimen and collar into the SHB apparatus, the induction coil was turned on and allowed to heat the specimen to the desired temperature. A thermocouple was inserted into a hole in the collar to ensure proper values were obtained. Once the specimen reached the necessary temperature, the induction coil was turned off and removed from the immediate testing area. This was done to mitigate the effects of the current in the induction coil that would skew the results obtained from the strain gages due to their weak signal amplitude.

3.2 Determination of 1080 Johnson-Cook Constitutive Model

Using the explained equipment and methods above, UDRI conducted numerous tests on both VascoMax 300 and 1080 steel. A test matrix is provided in for both quasi-static and dynamic loading. A more detailed table of the tests run for both 1080 steel and VascoMax 300 is shown in Appendix 1.

Table 1 - 1080 and VascoMax Test Matrix

Material	Temp.	No. of tests at ~1/s	No. of tests at ~500/s	No. of tests at ~1000/s	No. of tests ~1500/s	Total No. of tests
1080 steel	RT (70°F)	2	2	2	2	8
1080 steel	300°F		2	2	2	6
1080 steel	500°F		2	2	2	6
1080 steel	7500°F		2	2	2	6
Vascomax 300	RT (70°F)	2	2	2	2	8
Vascomax 300	500°F		2	2	2	6
Vascomax 300	750°F		2	2	2	6
Vascomax 300	1000°F		2	2	2	6

To begin, UDRI obtained quasi-static data from a tensile strength test done on an Instron machine. Each specimen was loaded till failure and a stress-strain relation was obtained from this data. Figure 23 shows the typical stress strain curve for 1080 steel at a strain rate of quasi-static, in which the engineering stress-strain values were converted to true stress-strain utilizing the following two equations [14].

$$\mathcal{E}_{true} = \ln(1 + \mathcal{E}_{eng.}) \quad (45)$$

$$\sigma_{true} = \sigma_{eng.} (1 + \mathcal{E}_{eng.}) \quad (46)$$

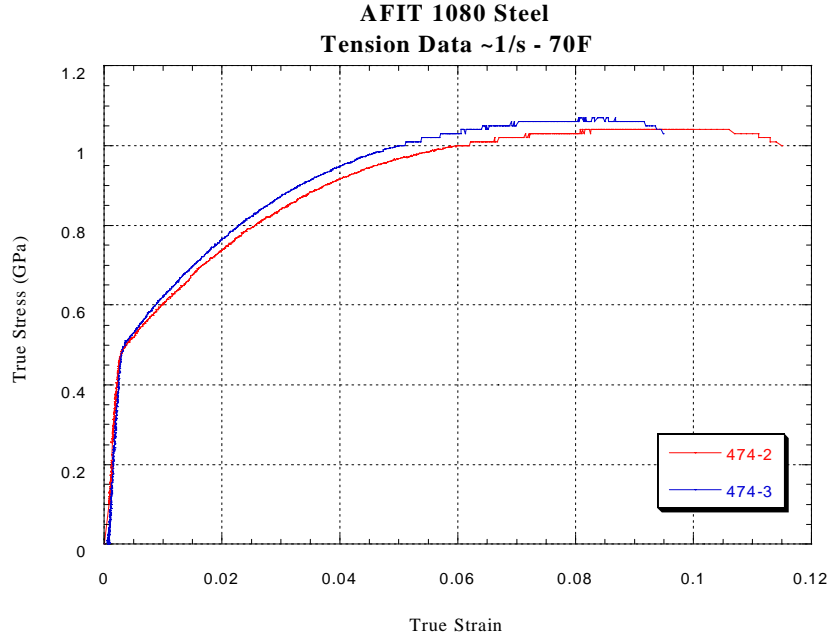


Figure 23 - Quasi-static Tension Test for 1080 Steel

VascoMax 300 also was tested quasi-statically, but it is shown later in this work that its stress-strain relations needed to be corrected, for both quasi-static and dynamic tests.

The 1080 steel data from UDRI required no modifications to allow the Johnson-Cook constitutive model to fit the data. As described earlier, the methodology of determining the coefficients is a three step process, which looks at the elastic and plastic regions separately. Equation 44 restates the Johnson-Cook equation for reference.

$$\sigma = (A + B\varepsilon^n)(1 + C \ln \dot{\varepsilon}_p)(1 - T^{*m}) \quad (47)$$

Again the first pair of parentheses contains the coefficients for quasi-static states and the other two pairs allow for the understanding of dynamic and temperature effects.

For 1080 steel, the two quasi-static tests were used to obtain the A, B and n coefficients of the equation. To determine the yield stress, A, only the elastic region was to be analyzed. For both quasi-static tests 474-2 and 474-3, the linear slope of the elastic region was found by a linear fit of the data acquired from the UDRI tests. The slopes or elastic modulus of 474-2 and 474-3 were 175.57 GPa and 230.1 GPa, respectively. This work used a .2% offset yield limit for 1080 steel. Historically, .2% has been used for numerous metals, but was originally used to understand the behavior of steel having an upper and lower yield point. For VascoMax 300, a different offset was used and will be explained later.

With the elastic modulus for both the quasi-static tests identified, the usage of .2% offset allowed the yield stress to be found from the intersection of the .2% offset and the experiment data. Figure 24 and Figure 25 display the results of this effort.

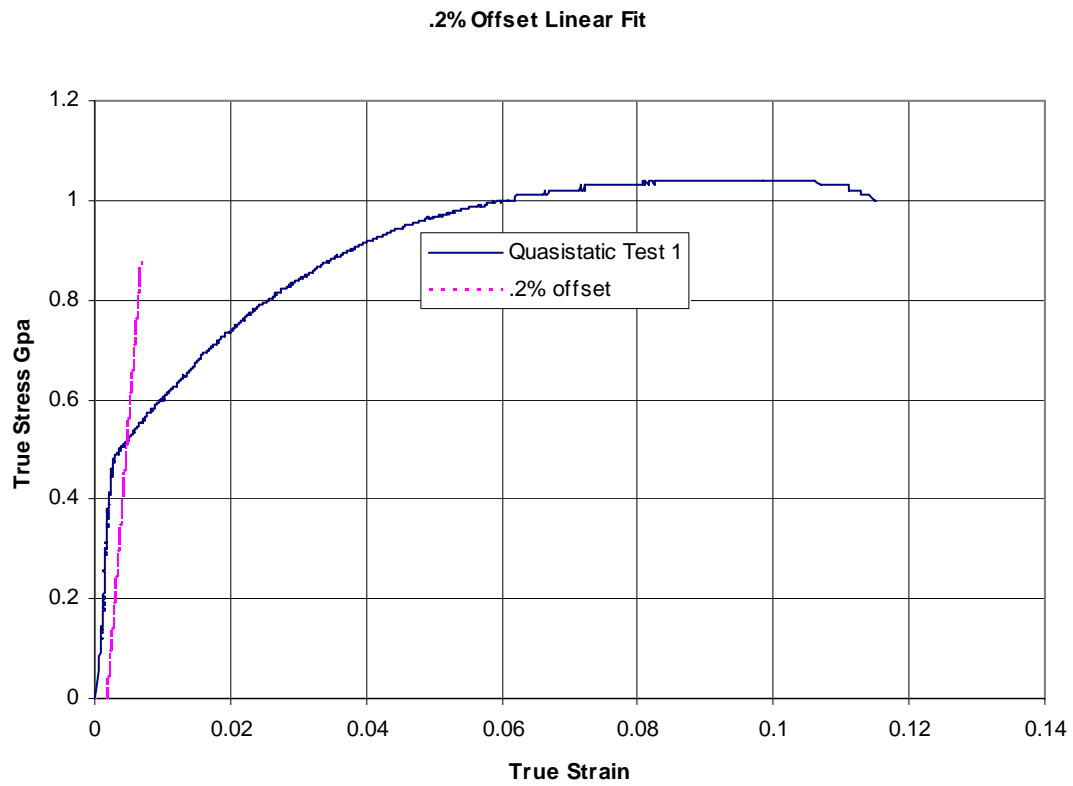


Figure 24 - 1080 Steel Quasi-static test 474-2

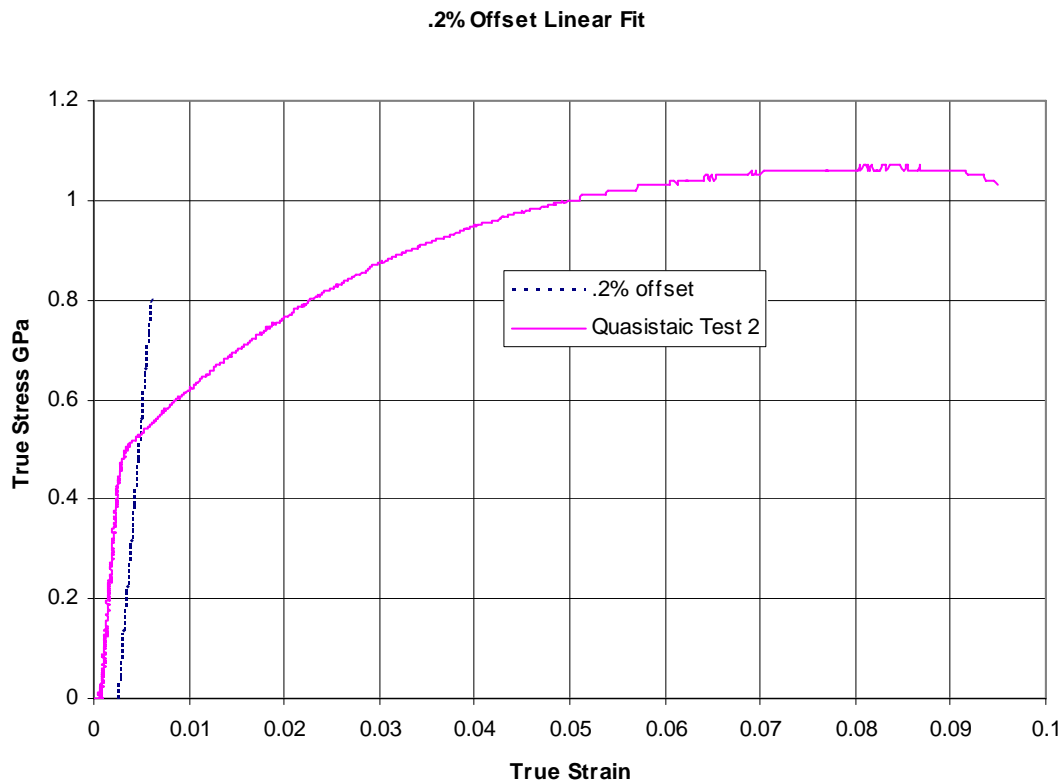


Figure 25 - 1080 Steel Quasi-static test 474-3

Once the A coefficient was solved for, the strain hardening factor, B, and the strain hardening index, n, were found. These two values had to be found simultaneously. To accomplish this, the plastic region of the quasi-static curves needed to be defined in terms of only plastic strain and stress. The effective stress difference (ESD), or stress obtained after the yield stress, was defined as the total stress minus the yield stress. The plastic strain equaled the total strain minus the linear equation found for .2% offset using the known ESD.

Taking the log of both the ESD and plastic strain allowed a linear fit to be applied to the plot. Figure 26 and Figure 27 show the linear equations found to fit the log plots. These linear fits are a least square fit of the data points. It should be noted here that the strain after 0.08 was found to be negligible because it skewed the B and n coefficients away from fitting the experimental data. This will be shown later in this chapter. To see the difference caused by the usage of strain past 0.08, the Taylor test model in CTH used both B and n values before and after the correction made concerning the 0.08 strain limit.

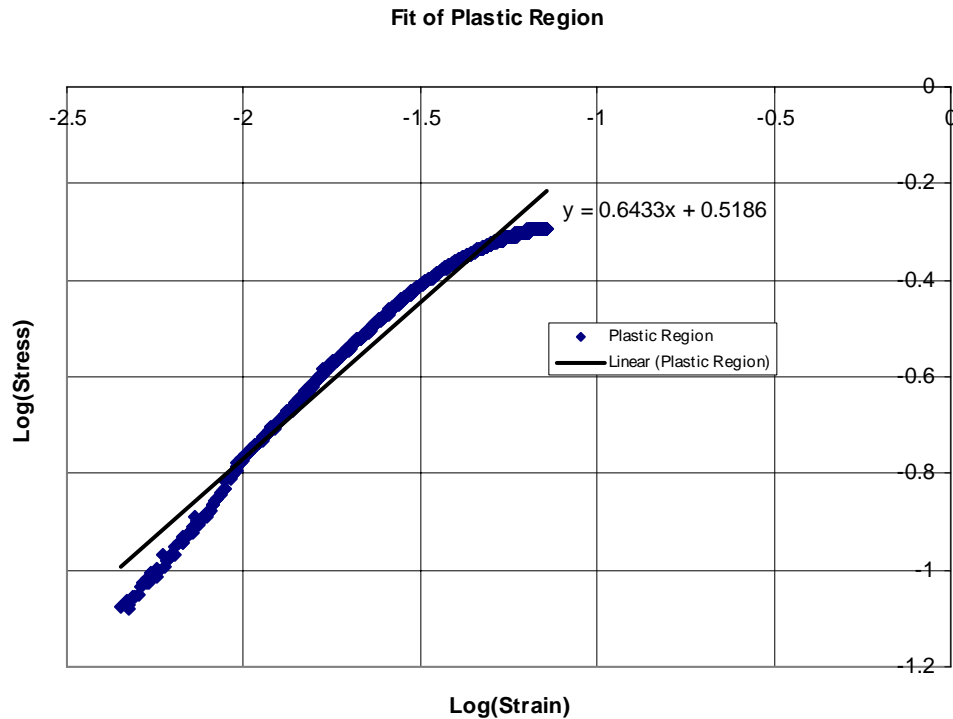


Figure 26 - Plastic Region Fit of 1080 Test 474-2

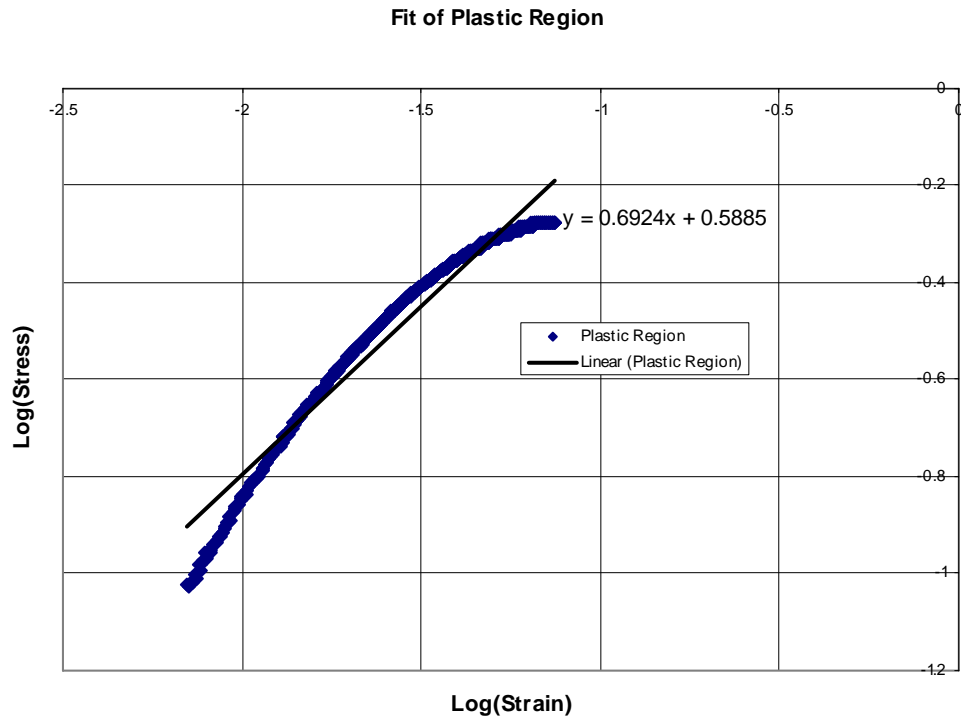


Figure 27 - Plastic Region Fit of 1080 Test 474-3

From linear equations on these plots, n is the slope of the line and B is determined from 10 raised to the y intercept. Table displays the Johnson-Cook coefficients for the first parenthesis of the equation found in this work and those determined by UDRI (for comparison).

Table 2 - 1080 Johnson-Cook Coefficients from Quasi-static tests

Test Facility	Test Number	A (GPa)	B (GPa)	n
AFIT	474-2	0.520	3.300	0.643
	474-3	0.530	3.880	0.692
	Average	0.525	3.590	0.753
UDRI	474-2	0.513	2.960	0.646
	474-3	0.514	2.700	0.578
	Average	0.514	2.830	0.612

The quasi-static tests defined the general curve of the plastic region fit, but this needed to be refined to account for strain rate and temperature effects. To explain the effects of strain rate, the strain rate sensitivity parameter, C , was found from varying strain rates at room temperature. This parameter is found by analysis of the second pair of parenthesis, $(1 + C \ln \dot{\varepsilon}_p)$. To produce a value explaining the strain rate sensitivity of a material, the strain rate must be related to the ESD at a certain strain value. This relationship comes from the knowledge of the strain pulses in the SHB. From equation 43, we see that,

$$\varepsilon_i = \frac{1}{2E} c_o \rho V_s \quad (48)$$

and is ε_i is constant when V_s is known from the SHB test. It is also known from chapter 2 that,

$$\sigma(t) = E \frac{A_b}{A_s} \varepsilon_t(t) \quad (49)$$

which also can be written as,

$$\varepsilon_t(t) = \frac{A_s}{A_b E} \sigma(t) \quad (50)$$

to allow the transmitted pulse to be defined. To define the reflected strain pulse, we see from chapter 2 that,

$$\dot{\varepsilon}(t) = \frac{2 \cdot C_o}{L} \varepsilon_r(t) \quad (51)$$

and can written also as,

$$\varepsilon_r(t) = \frac{L}{2C_o} \dot{\varepsilon}(t) \quad (52)$$

where L is the specimen gage length.

Remembering from chapter 2 that a relationship between the strain pulses can be given as,

$$\varepsilon_t = \varepsilon_r + \varepsilon_i \quad (53)$$

the relationship becomes,

$$\frac{A_s}{A_b E} \sigma(t) = \frac{L}{2C_o} \dot{\varepsilon}(t) + \frac{1}{2E} c_o \rho V_s \quad (54)$$

where every parameter is constant except for the predetermined striker bar velocity yielding a constant strain rate. With these values known the flow stress can be solved for in equation 52 as,

$$\sigma(t) = \left(\frac{L}{2C_o} \dot{\varepsilon}(t) + \frac{1}{2E} c_o \rho V_s \right) * \left(\frac{EA_b}{A_s} \right). \quad (55)$$

A typical value of flow stress for 1080 steel is 1.05 GPa at 0.08 true strain for quasi-static testing. Other test values are shown in Appendix 1. By plotting the strain rate, flow stress, and strain versus time, it is shown that at an average strain rate, a correlating flow

stress and strain can be deduced. This is critical to determining the C coefficient because it directly relates the strain rate to a strain and stress values from which C will be examined at. Figure 28 depicts the determination of the flow stress and strain at an average strain rate [8].

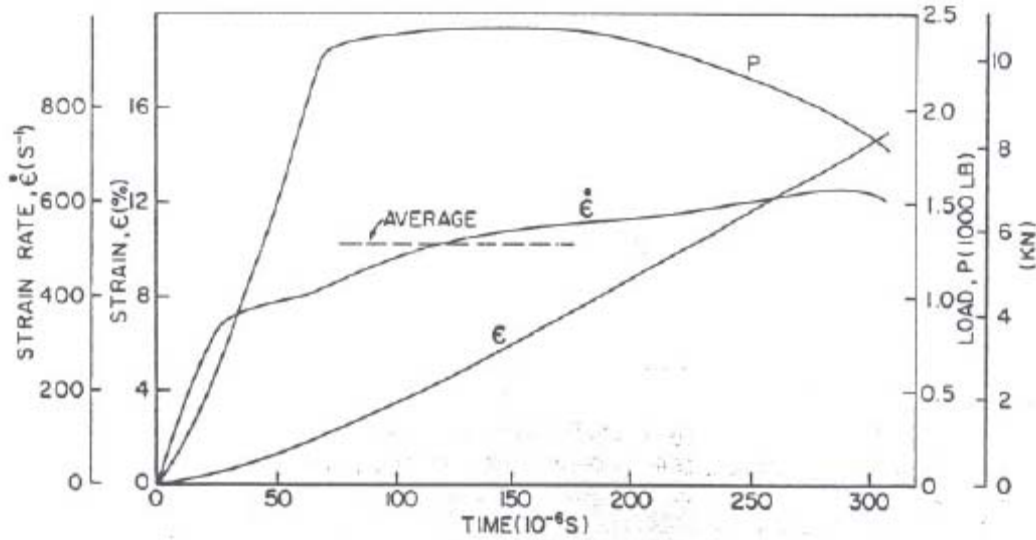


Figure 28 - Sample Time-History Plot

From the three constant strain rates used in this work, a constant value of strain can be used to find the flow stress values. This work deemed the flow stress and strain values determined by UDRI to be inaccurate of the relationship defined by the Johnson-Cook model. UDRI chose a value of 0.08 strain to determine flow stress. Strain of 0.08 marks the fracture point in 1080 steel and also represents a departure from the normal true stress-strain relation. The 1080 steel stress-strain curve at 0.08 tends to flatten out, which does not agree with an increasing true stress-strain relation. A comparison of UDRI's ability to fit the SHB data and this work's results are shown later in this chapter. To choose a constant value of strain, however, this work took another approach.

A value of 0.062 strain was chosen to define the value of flow stress for determination of both C and m coefficients. This was due to an analysis of the curve fit from the average A, B, and n coefficients and is shown in Figure 29 and Figure 30.

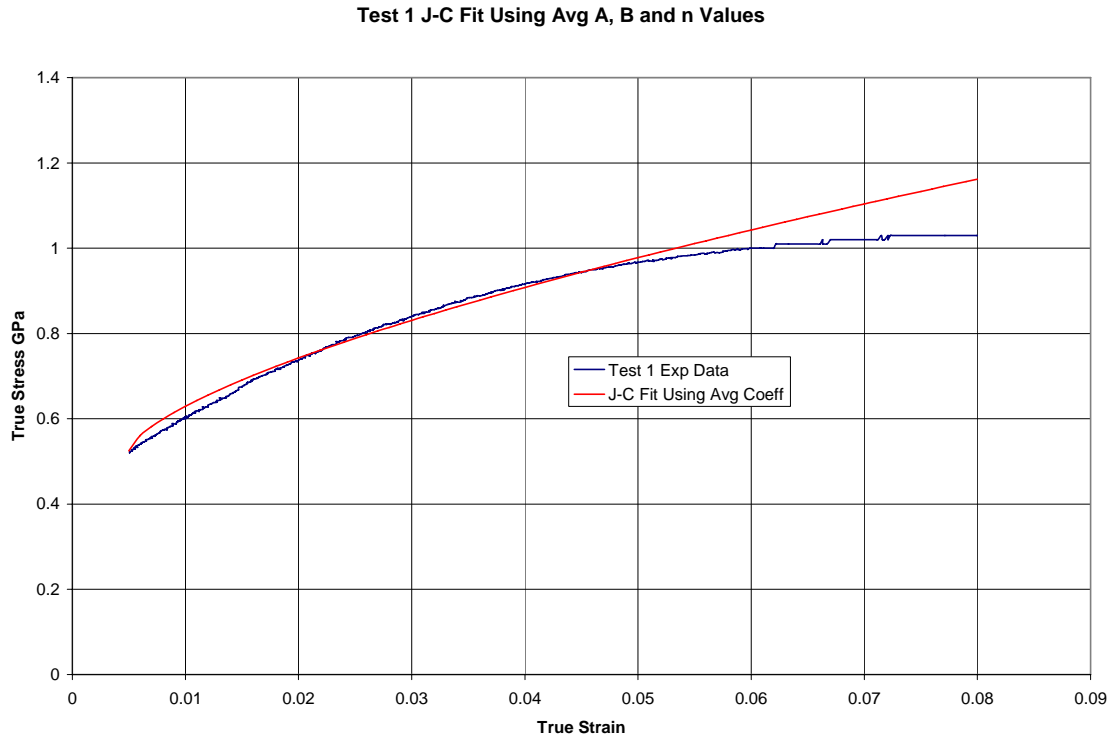


Figure 29 - Quasi-static test 474-2 J-C Fit

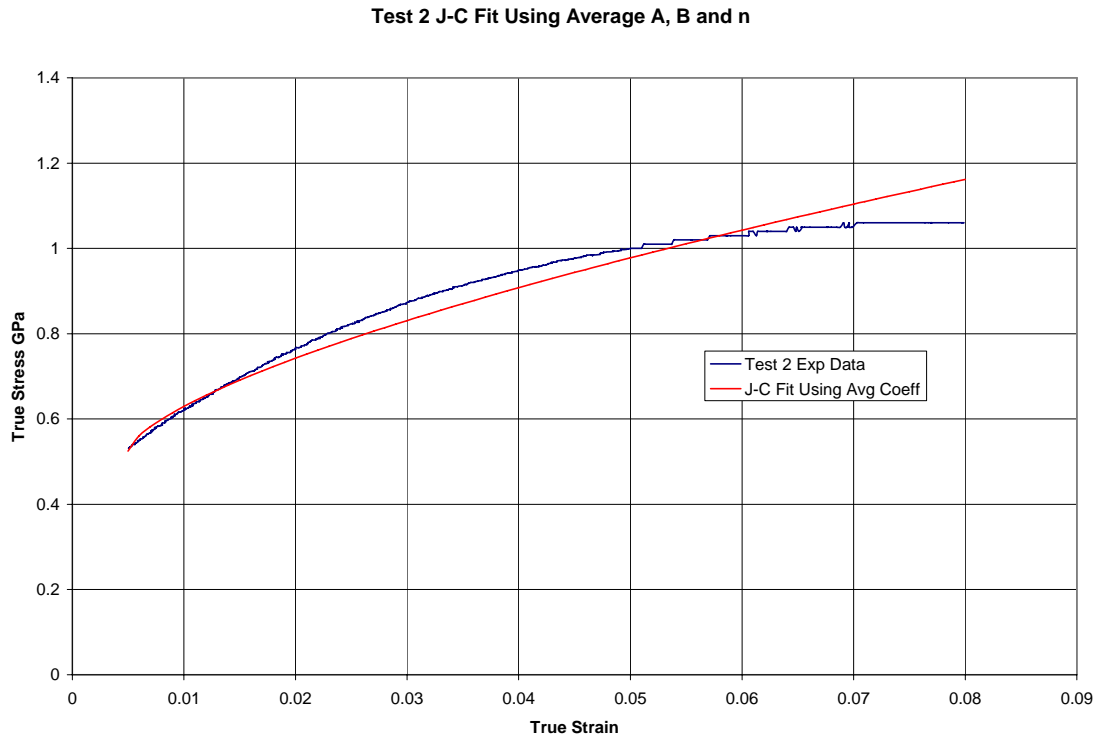


Figure 30 - Quasi-static test 474-3 J-C Fit

These plots show that 0.062 strain represents an area of interest in the plastic region due to the average Johnson-Cook coefficients fitting the experimental data for both tests well. Also, 0.062 is a relatively high strain, but does not occur too close to the fracture region of the 1080 steel stress-strain curve. Again, the value of 0.08 used by UDRI was found by this work to be near the fracture strain and was in an area not approximated well by the Johnson-Cook model.

From the experimental data obtained from the SHB tests, stress values were interpolated to 0.062 strain and then averaged for the two tests at each strain rate. This stress is the dynamic stress. By plotting the dynamic stress divided by the static stress versus the Ln of strain rate, a series of data points were created. A least square fit of

these points produced a slope that described the C coefficient. Fixing the y intercept to the quasi-static point at (0,1) dictated the C coefficient be in agreement with the curve fit already produced by the A, B and n coefficients. Figure 31 shows the determination of C.

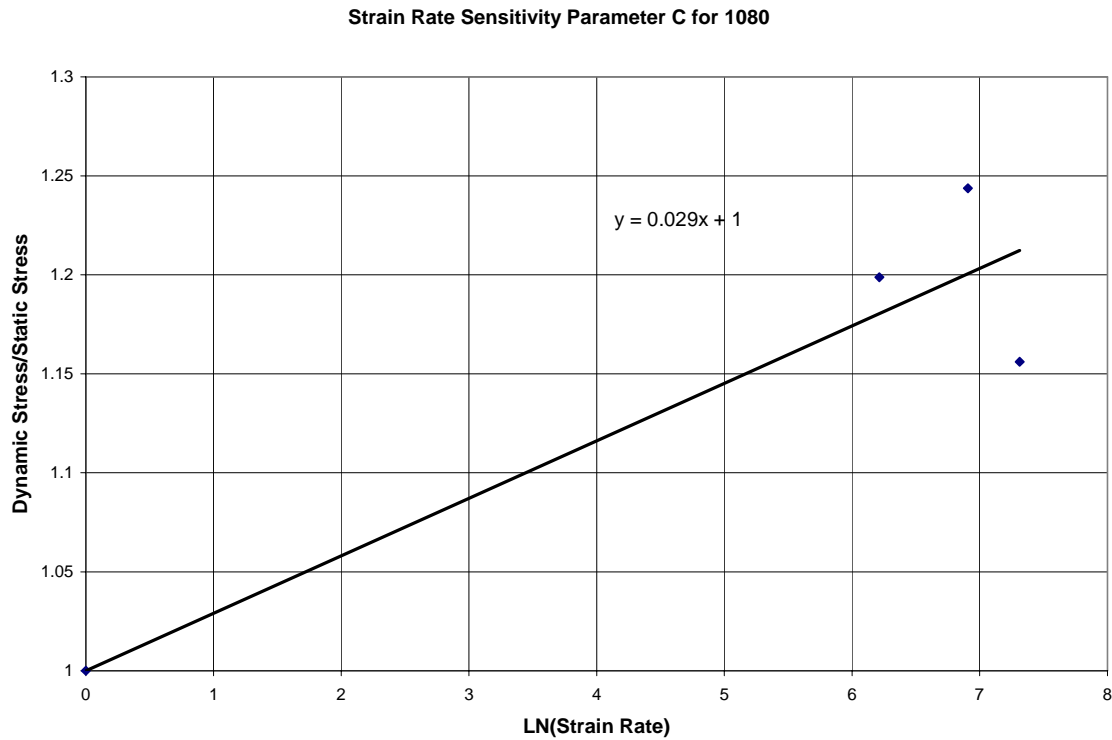


Figure 31 - Strain Rate Sensitivity of 1080 Steel

The slope of the least square fit gives a C coefficient of 0.029 for 1080 steel. Again, each point in the plot represents two tests at each of the strain rates. Appendix 2 contains the interpolation of stress at 0.062 strain for each strain rate.

To understand the effects temperature causes on the dynamic response of the 1080 steel, the Johnson-Cook constitutive model employs the softening coefficient, m, and T*,

as in the third pair of parenthesis, $(1 - T^{*m})$. T^* is easily calculated for each temperature tested at and is shown in Appendix 2. It is noted here that room temperature was taken as $60^\circ F$ to allow the specimen temperature of $70^\circ F$ to be used when finding m . This was done to have a non-zero T^* , which would have resulted in the log of zero and is shown later in this section. The melting temperature for 1080 is $2550^\circ F$ and was provided in the UDRI report [14]. With T^* for each temperature defined, m could be found for varying temperature and strain rate. Again, flow stress was found at 0.062 through interpolation of the experimental stress. With A , B , n , and C defined at a certain strain rate, it can be assumed that first two parts of the Johnson-Cook equation are a constant and from this it can be shown that a plot of $\log(1 - (\sigma_{dynamic} / \sigma_{static}))$ vs. $\log(T^*)$ yields points that correlate to m . Note that the dynamic stress is at the test temperature and the static stress is at room temperature. Appendix 2 contains the other two plots for determining m at the three strain rates. Here, Figure 32 depicts the determination of m for a strain rate of 500/s. A least square fit was used to find the fit of the data points and represents the value of m . Each data point represents one of the two tests at each of the three temperatures.

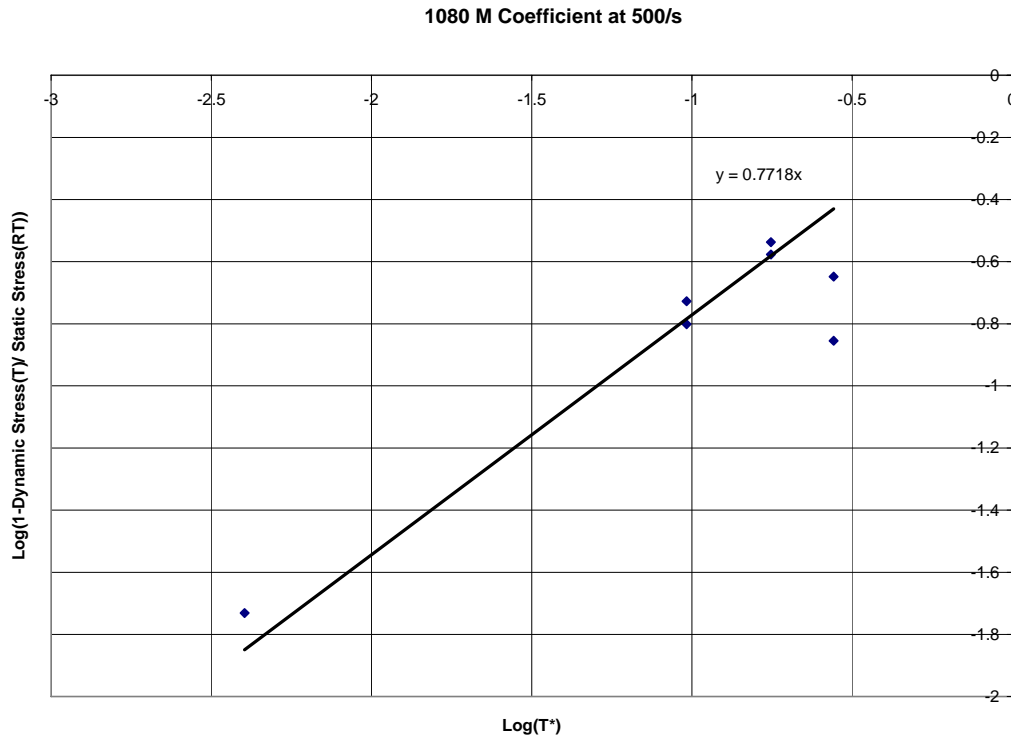


Figure 32 - m Coefficient for 1080 steel at 500/s

From all three plots, an average m coefficient was found to be 0.6677. Below in Table 3 are all of the coefficients for 1080 steel. Appendix 2 contains all calculations and plots for the determination of the m coefficient at 1000/s and 1500/s.

Table 3 - J-C Coefficients for 1080 Steel

Test Facility	Test Number	A (GPa)	B (GPa)	n	C	m
AFIT	474-2	0.520	3.300	0.643		
	474-3	0.530	3.880	0.692		
	Average	0.525	3.590	0.668	0.029	0.753
UDRI	474-2	0.513	2.960	0.646		
	474-3	0.514	2.700	0.578		
	Average	0.514	2.830	0.612	0.031	0.8903

From an initial examination of the coefficients developed by this work, it is shown that there is good agreement between the two models (AFIT and UDRI)

developed for the quasi-static coefficients A, B, and n. For coefficients C and m a small difference exists between the AFIT and UDRI model due to the selection of strain to study the flow stress at. UDRI chose 0.08 strain, while this work looked at the flow stress at 0.062 strain. This resulted in a slightly higher stress values for the study conducted by UDRI, causing the C and m coefficients to increase. This work chose 0.062 to understand the flow stress due to the curve fit provided by the A, B and n coefficients.

With an accurate fit for the quasi-static tests as shown in Figure 29 and Figure 30, the dynamic loading tests were examined to ensure that the Johnson-Cook model approximated the full range of material behavior. A successful method used by other researchers to define the effectiveness of a constitutive model to fit a wide range of dynamic loadings is to examine the flow stress at a certain strain. By plotting the flow stresses versus the strain rate, a graphic estimation of the curve fit is obtained. Figure 33 displays this plot. This work used 0.062 strain as described earlier to find the flow stress values at each strain rate and temperature to create the plot below. The constant Johnson-Cook lines seen in the plot were obtained by using the previously stated A, B, n, and C coefficients and varying T^* for each specified temperature. Then increasing strain rate on the x-axis produced the constant model lines.

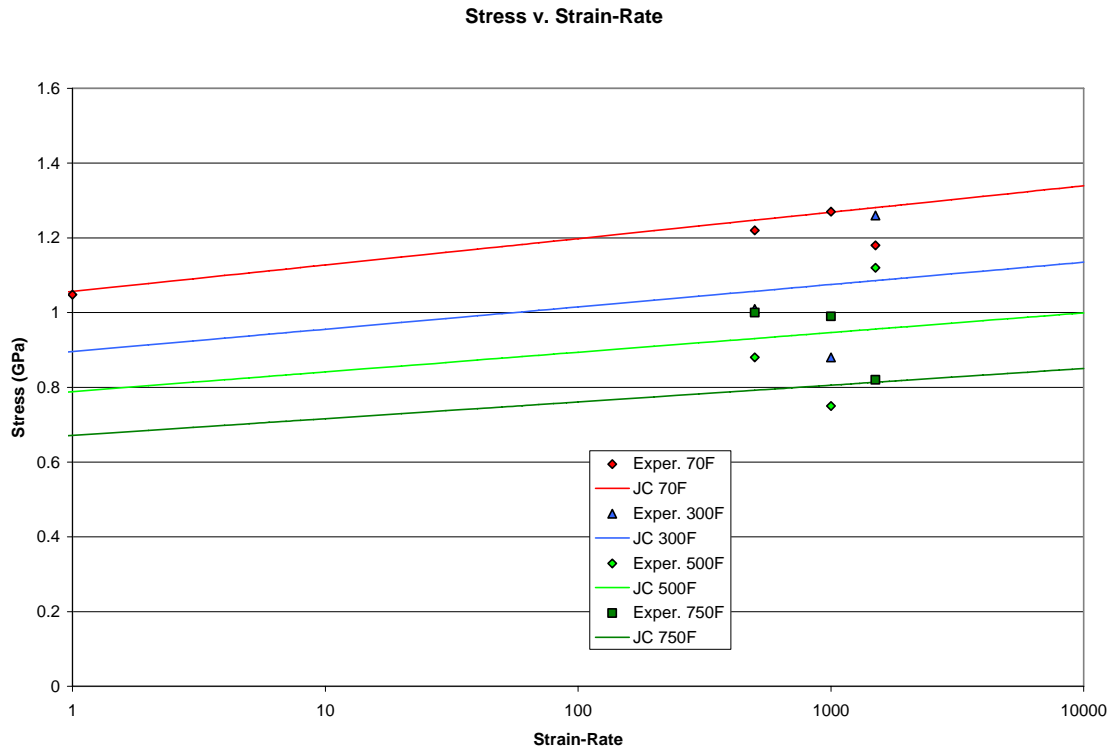


Figure 33 - 1080 J-C Fit of Dynamic Loading

In this plot, it is shown that the Johnson-Cook model follows the relationship between temperature and flow stress. This relationship states that as temperature is increased, the flow stress decreases [6]. The experimental flow stresses at 0.062, shown in the plot, also adheres to this relationship. In addition, the Johnson-Cook constitutive model for each temperature approximates the three strain rates well. It is seen that at low strain rate and low temperature the model develops a better estimate of the material behavior, than at high strain rate and low temperature. In examination of high strain rate and high temperature, the model yields better results than for high strain rate and low temperature. This fact is due to the inability of the Johnson-Cook model to couple the temperature and strain rate sensitivity parameters due to the piecemeal solving technique allowed by the

Johnson-Cook equation. However, it should be noted that the model yields valid results for a wide range of temperatures and strain rates, but further research could produce a better fit for a narrower range of parameters. Figure 34 provides the comparison from the UDRI data.

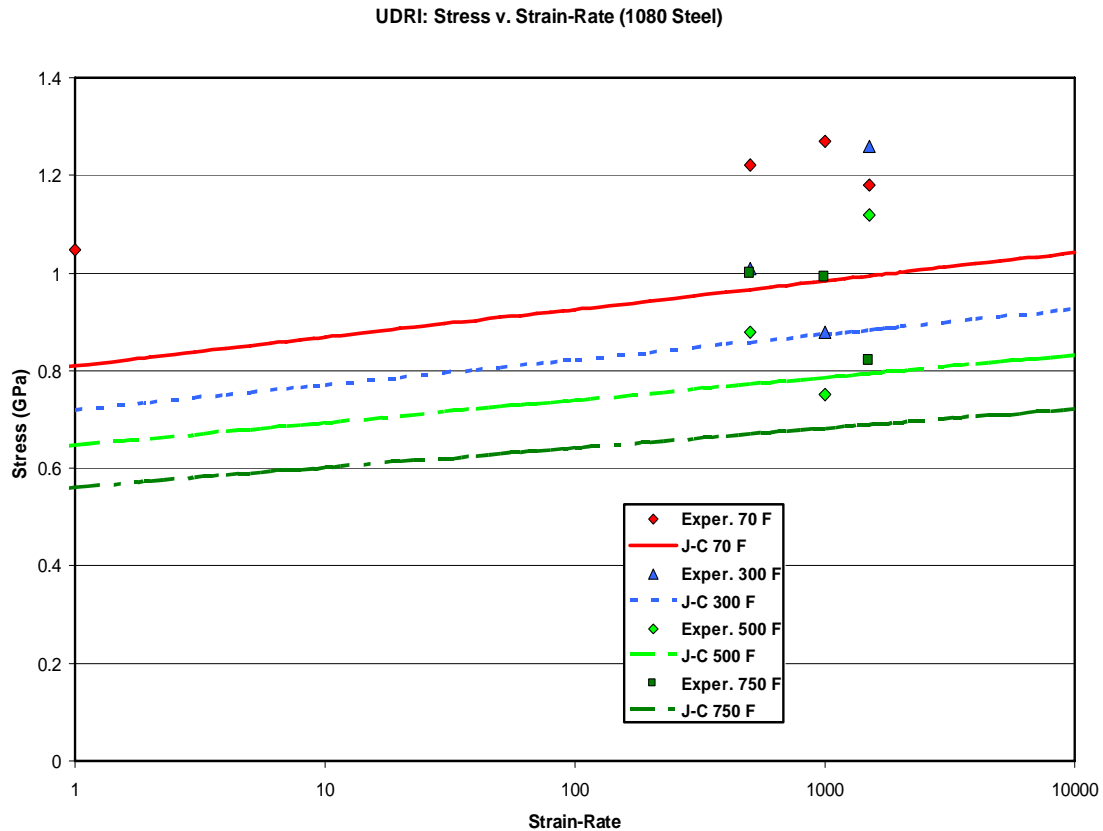


Figure 34 – UDRI 1080 J-C fit of Dynamic Loading

Here it is shown that this work developed a better Johnson-Cook model to approximate the flow stress at a certain strain over various strain rates and temperatures. From the plot of the UDRI model, it displays a constant undershoot of the flow stress at the 0.08 strain.

When comparing the Johnson-Cook model to the entire plastic region of 1080 steel for a given temperature and varying strain rate, we see that it is able to approximate the stress-strain relation. Figure 35, Figure 36, and Figure 37 display the model's effectiveness at $500^{\circ}F$ at strain rates of 500/s, 1000/s and 1500/s.

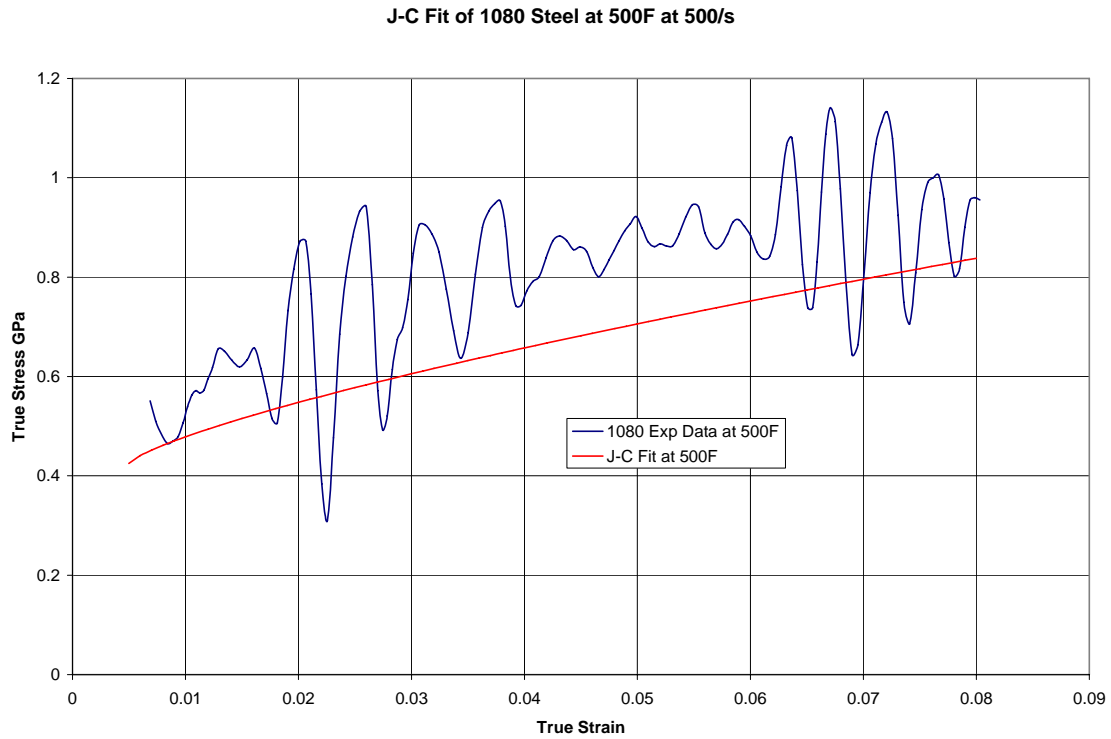


Figure 35 - J-C Fit of 1080 steel at 500F at 500/s

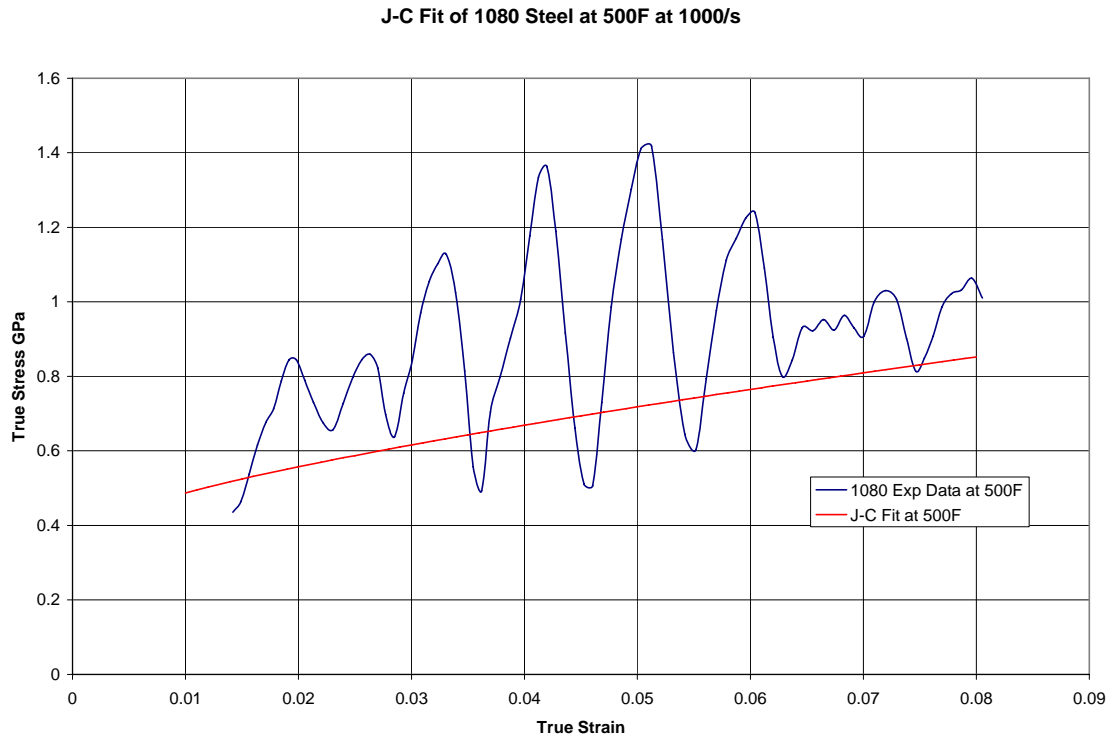


Figure 36- J-C Fit of 1080 steel at 500F at 1000/s

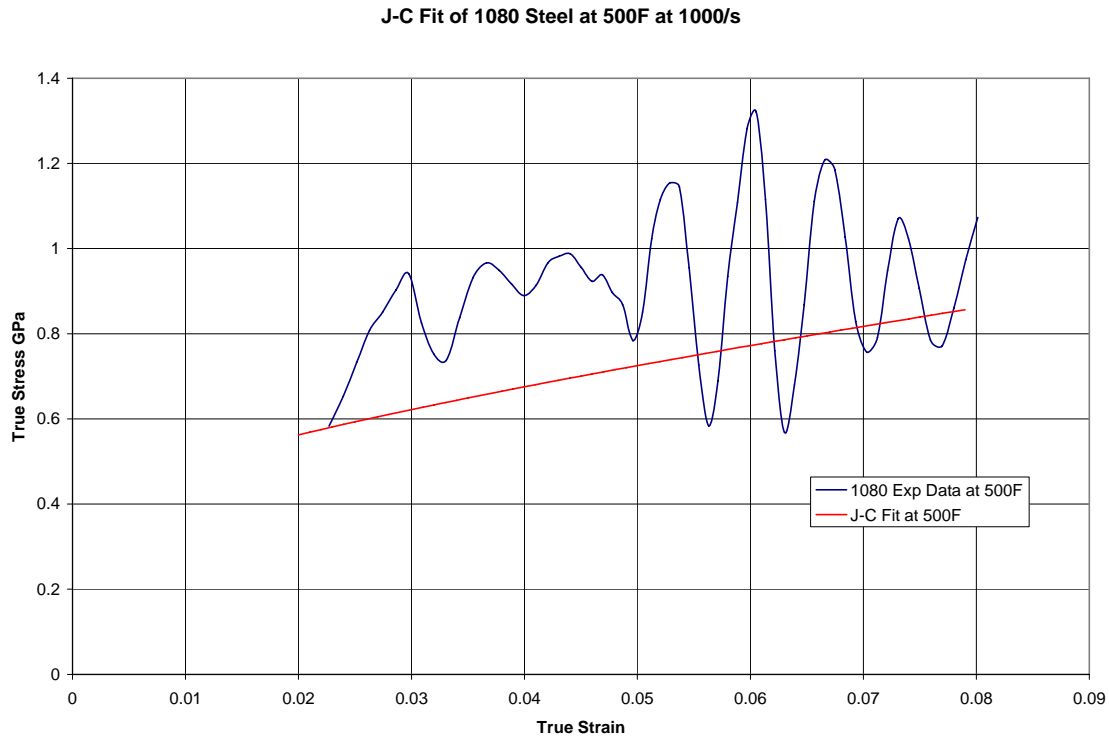


Figure 37 - J-C Fit of 1080 steel at 500F at 1500/s

It is seen that the Johnson-Cook constitutive model underestimates the flow stress in the plastic region for all three cases. This underestimation is better than overestimation because it will not lead investigators to overestimate the material strength capacity during loading. The model from visual inspection of the plots, however, approximates all strain rates with the same amount of accuracy. Again, the Johnson-Cook model was created to explain a multitude of strain rates and temperatures in this work, and it is expected that no case will have greater accuracy over the others due to the equivalent dependence of the model on all the cases.

3.3 Determination of VascoMax 300 Johnson-Cook Constitutive Model

3.3.1 Correction of the VascoMax 300 Data

As stated earlier, the loading of VascoMax 300 produced stress-strain relations that exhibited unusual behavior for steels. The elastic region for VascoMax 300 reacted as expected, giving a constant elastic modulus as the strain on the specimens were increased. However, when the loading on the specimen reached the yield limit, the steel did not strain-harden. Necking occurred as the VascoMax 300 reached its ultimate strength under loading. Figure 38 depicts the typical fracture and necking evident in VascoMax 300 under dynamic loading at 1000/s.

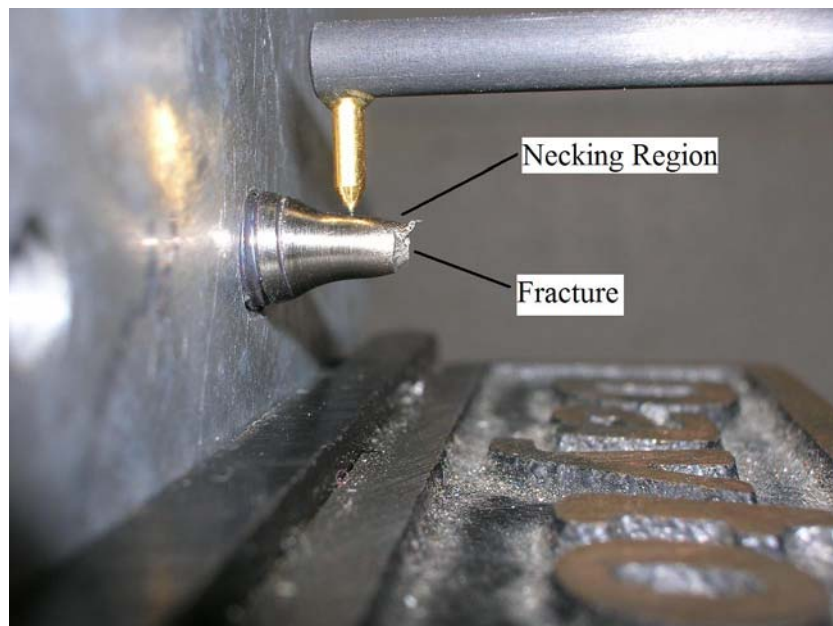


Figure 38 - Necking in VascoMax 300

From Figure 38, the necking occurs in a relatively small region of the gage length, suggesting little strain-hardening of VascoMax 300 before failure. This will be discussed later in this work.

The effect of the necking directly impacted the stress-strain curve produced by the SHB. This occurred because strain is measured and the cross-sectional area is not, resulting in stress values that represent the initial area and not the necked area. Figure 39 depicts the effects of necking on the stress-strain relation. This is the quasi-static tests for VascoMax 300.

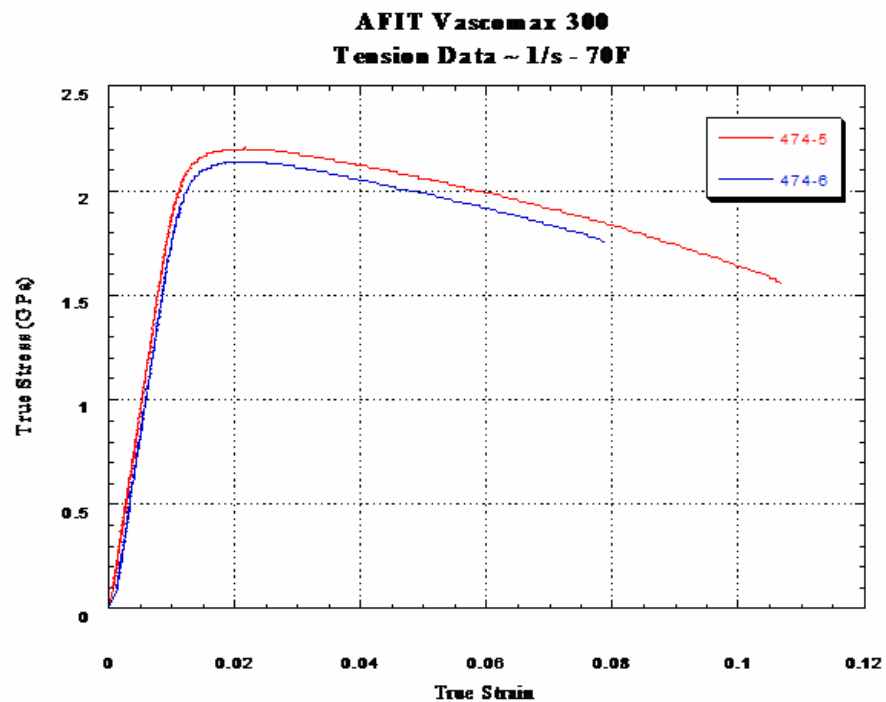


Figure 39 - Quasi-static Tension test for VascoMax 300

It can be seen that for VascoMax 300, material strength only rises for a short period of strain and then decreases. This type of curve will not be compatible with the Johnson-

Cook constitutive model, creating the needed to correct for the change in the cross-sectional area. The Johnson-Cook model cannot approximate a negative curve due to all the coefficients being positive values. Hence, the decreasing part of the stress-strain curve is invalid for the Johnson-Cook equation. Here it should be noted that all stress-strain curves from UDRI for VascoMax 300 are true stress and true strain, even though they display the unusual negative slope due to UDRI's neglect of necking observed in the specimens. This work explored the process of correcting the VascoMax 300 data.

In order to correct the stress and strain at any point in the plastic region, a relation of uncorrected to corrected values needed to be formulated. The employment of the incompressible plastic flow theory solves this relation. It states that volume remains constant for an incompressible material, meaning that density remains constant. Equation 53 represents the law of incompressible plastic flow as,

$$A_f L_f = A_o L_o = V \quad (56)$$

where A_f is the final cross-sectional area of the specimen, L_f is the final length of the specimen, A_o is the original cross-sectional area of specimen, and L_o is the original length of the specimen. Knowing this, it can be shown that a stress relation exists between the undeformed and deformed area as,

$$\sigma^* = \frac{A}{A^*} \sigma \quad (57)$$

where A is the initial cross-sectional area of the specimen, A^* is the deformed area, and σ^* is the corrected stress. A similar relationship is shown to exist for strain as,

$$\varepsilon^* = \frac{A}{A^*} \varepsilon \quad (58)$$

where ε^* is the corrected strain.

To find A^* , the diameter change due to the necking had to be determined. Preliminary techniques included the use of a micrometer to find the largest change in diameter. This was later discarded due to the micrometer's inability to accurately measure the necked area. A profilometer solved this problem and is shown in Figure 40. The Taylor/Hobson Form Talysurf Series 2 profilometer located in the Aero Lab at the Air Force Institute of Technology (AFIT) was selected to measure the VascoMax 300 specimens. A profilometer can measure form of an object, which is defined as deviation away from the intended nominal shape of a surface, ignoring roughness and waviness [15]. For this work, knowledge of the form of the specimens is crucial to understand the nature of the necking.



Figure 40 - Taylor-Hobson Profilometer

The profilometer has a 10mm range of vertical measurement with a resolution of 0.8 nm. Even though the profilometer's capacity is far greater than the requirements needed to measure the specimens, this guaranteed excellent results.

After the Aero Lab at AFIT had constructed a bracket to secure the specimens via the threading used in the SHB tests, the stylus of the profilometer was aligned with the beginning of the gage length on the specimen. Figure 41 shows this setup.

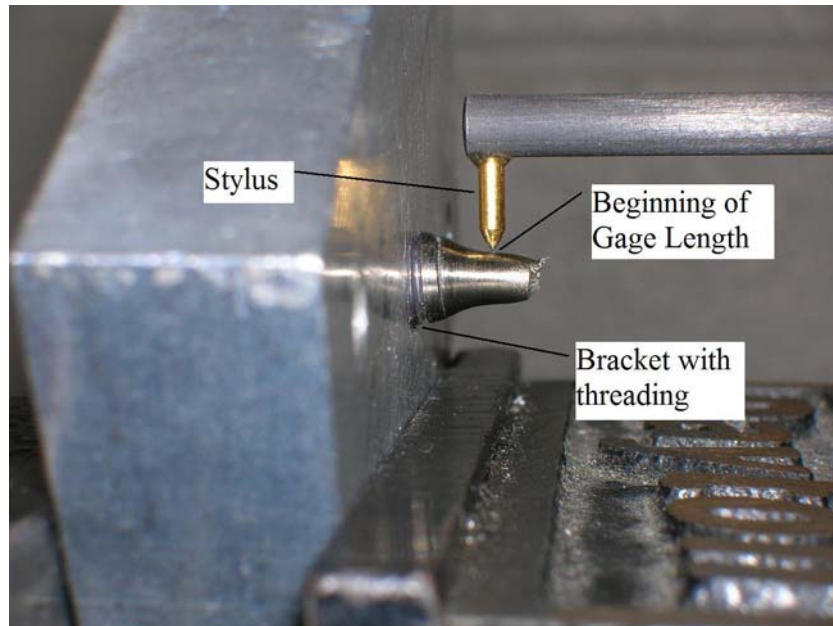


Figure 41 - Specimen Setup on Profilometer

The alignment of the profilometer was done by eyeing the stylus directly on top of the specimen and then determining the approximate measurement length to be taken. This was done by moving the stylus along the intended path of measurement via the joystick. Since most of the fracture in the VascoMax 300 occurred as 45 deg fractures, both sides of the specimen were measured with respect to the longest possible length on each side. This would ensure that the full necked region before the fracture line was accounted for and thus would yield the greatest change in diameter.

Once correct placement of the stylus was complete, the Ultra software provided with the profilometer was utilized to zero the stylus horizontally and vertically. Next the desired length of measurement was entered in the software and the profilometer traced the specimen. Once complete, the Ultra software provided a raw profile view with

change of vertical direction on the y-axis and length measured gage section on the x-axis.

Figure 42 displays the profile generated by Ultra.

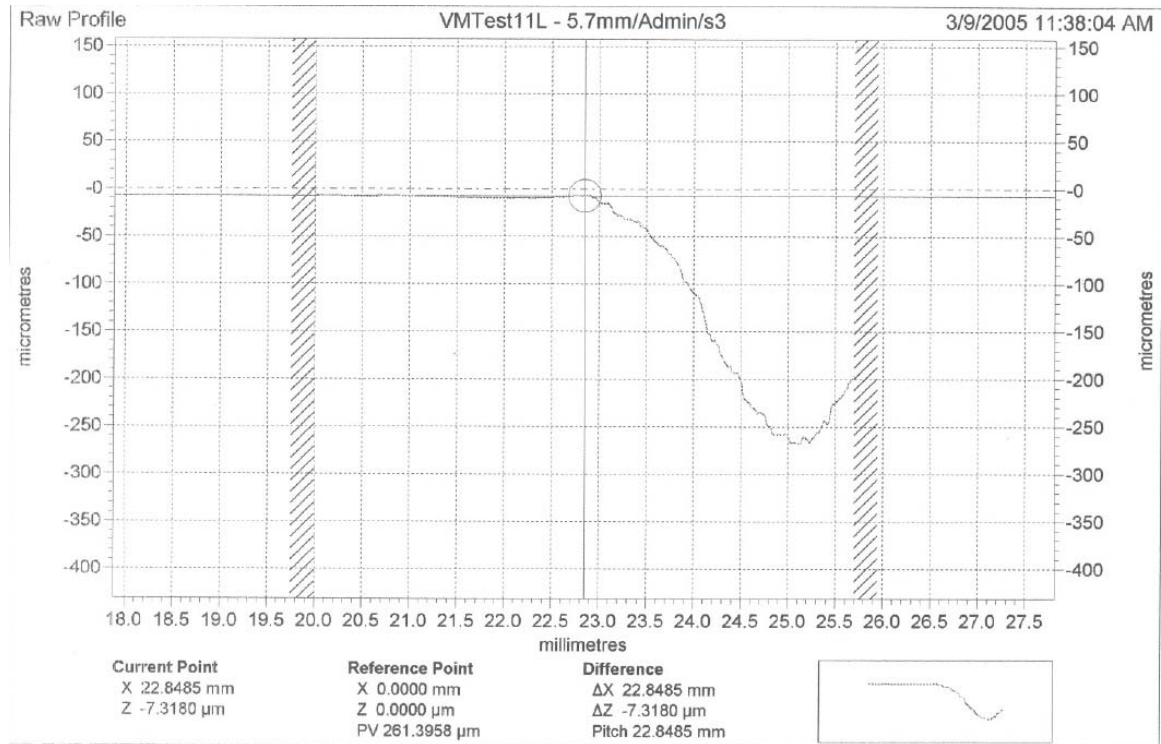


Figure 42 - Ultra Raw Profile of VascoMax 300 Test 11

Along with the raw profile of the specimen's necking, the Ultra software also provided the greatest change in vertical direction, thus mitigating error from having to eye the profile plot for the diameter change. The diameter change for each specimen is given in Table 4.

Table 4 - VascoMax 300 Diameter Change

Test Number	Side 1 um	Side 2 um	Total um
474-5 (quizi)	271.6119	361.9107	633.5226
474-6(quizi)	325.5214	252.3296	577.851
3	346.1834	258.9901	605.1735
4	269.465	316.5222	585.9872
15	385.1566	209.5906	594.7472
16	480.1476	419.7848	899.9324
19	367.1849	354.9376	722.1225
20	357.7897	362.7672	720.5569
17	518.6343	540.0109	1058.645
18	547.6695	707.6166	1255.286
1	317.2911	339.7538	657.0449
2	349.1301	334.0807	683.2108
9	261.5717	267.136	528.7077
28	366.008	360.0125	726.0205
10	393.573	407.0501	800.6231
11	275.8872	390.0948	665.982
12	505.2393	415.2535	920.4928
13	488.8447	501.1523	989.997
6	305.7356	252.3296	558.0652
7	205.1523	196.1984	401.3507
21	493.6504	405.6915	899.3419
23	453.0281	427.8431	880.8712
24	395.629	421.2674	816.8964
25	376.4219	393.9167	770.3386
26	735.368	560.416	1295.784
27	404.8489	408.4615	813.3104

With the change in diameter for each specimen known, the stress and strain can be corrected. It should be noted that these measurements are only valid for correcting a stress-strain point near fracture and cannot correct any other point in the plastic region. This is due to the inability of the SHB test to measure the necking during the test and correlate a change in diameter value to a strain value while the experiment is being run. Hence, it will be shown that the new plastic curves will be linear since only one point in the plastic curve can be corrected.

To a correct the stress-strain relationship of VascoMax 300, a point on the curve that corresponded to the diameter change had to be determined. From engineering judgment, the final data point from the UDRI data is not applicable for correction due to VascoMax 300 failing before this strain. However, some point before this can be used. This author decided to choose a point between 85-95% of the final strain value to correct. From the UDRI data, it is seen in Figure 43 that there is a final spike in stress before failure and denotes the final necking value found earlier. With this point determined and the equations developed under the assumption of incompressible plastic flow, the corrected stress and strain values were found. Table 5 displays the results for VascoMax 300 test 3.

Table 5 - Correction of VascoMax 300

Test 3		
Change in Cross-Sectional Area		
Side 1	0.346183	mm
Side 2	0.25899	mm
Total Diameter Change	0.605174	mm
Original Values		
Original Stress	1.847	Gpa
Original Strain	0.07342	
Original Dia	3.175	mm
Original Area	7.917304	mm ²
Corrected Values		
New Area	5.186776	mm ²
Corrected Stress	2.819335	Gpa
Corrected Strain	0.112071	

With the new stress and strain values known for each test, a linear representation of the plastic region was now possible. The yield stress was chosen to be the final value used from the UDRI data to plot with the corrected stress-strain point for each test. The yield stress method will be discussed later and plots of all dynamic test yield stresses are shown in Appendix 3. Figure 43 depicts the difference between the uncorrected and

corrected data in test 3 for VascoMax 300. Appendix 3 contains comparison plots for all tests.

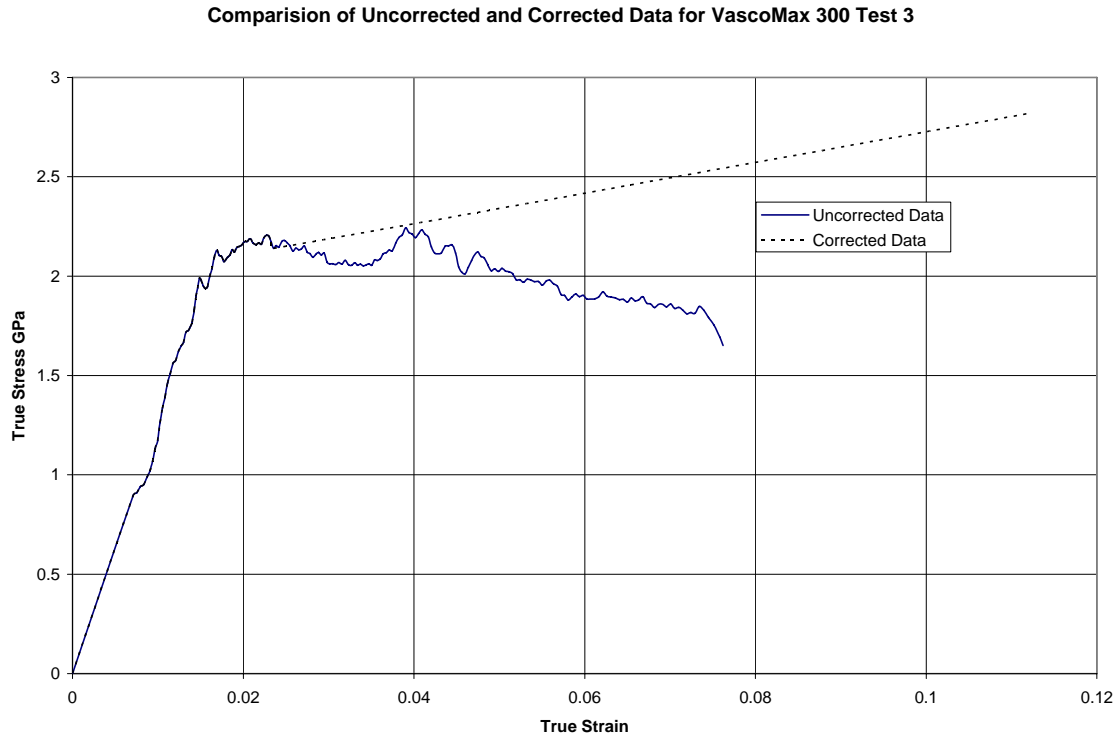


Figure 43 - Comparison of Uncorrected and Corrected VascoMax 300

It is shown in this figure that both the stress and the strain will increase due to the correction. It will be shown later that this correction yield excellent results as confirmed by the Taylor test analysis.

In addition to correcting the plastic curves for VascoMax 300, this work had to correct filtering errors found in the data from UDRI. Eight test in all contained data points that resulted from poor data collection and required a data point averaging method before the plastic region correction could take place. The data point averaging method used in this work involved taking the stress and strain values the peaks and average them

with the stress and strain values at with the corresponding lulls. This means taking a restively high stress value and adding it to a relatively low stress value and dividing the sum by two. A similar process is used in averaging the strain values. The peaks and lulls are evident in the figure below. The eight tests requiring this correction were tests 12, 13, 21, 23, 24, 25, 26, and 27. Figure 44 shows the UDRI data for test 12 and the required correction to give a valid stress-strain curve.

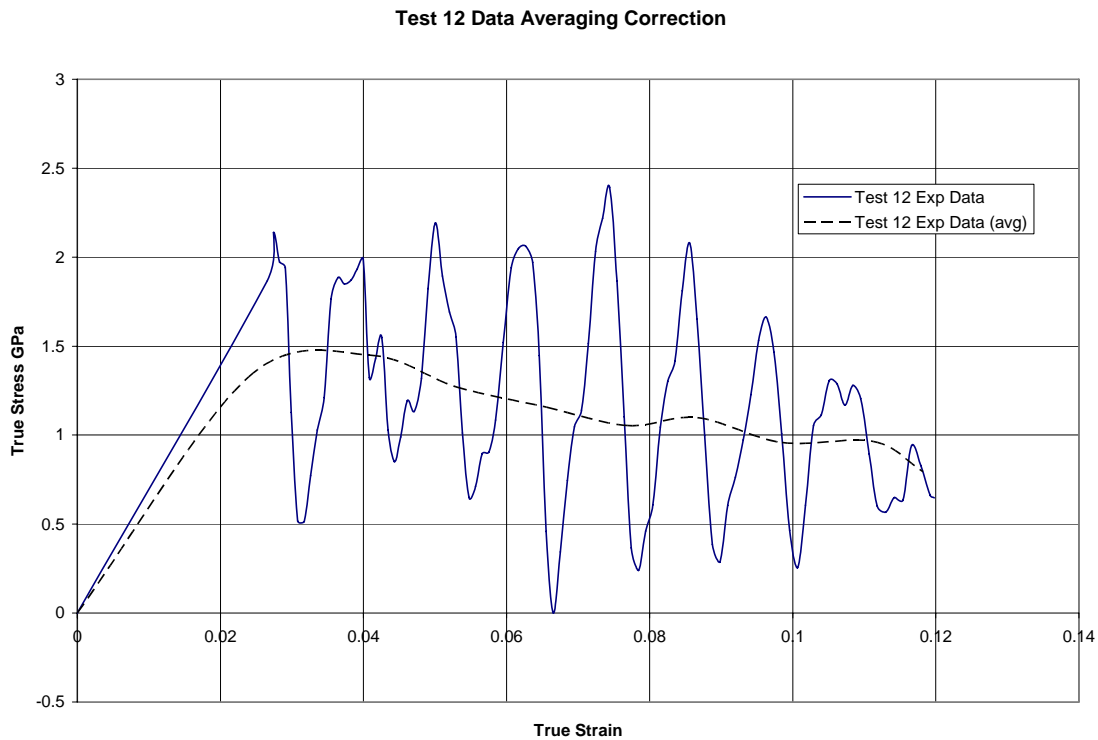


Figure 44 - Data Averaging Correction to VascoMax 300

Here it is seen that the averaged experimental data produces a more realistic stress-strain curve throughout the elastic and plastic regions. The averaged data was then used to find corrected stress-strain point as described earlier.

3.3.2 Johnson-Cook Coefficients for VascoMax 300 steel

Once the VascoMax 300 was corrected to allow a fit using the Johnson-Cook constitutive model, a similar process to that mention earlier for the 1080 steel of determining the coefficients was used. To not repeat the understood process of finding the coefficients, only the changes to the process will be discussed for VascoMax 300. As in 1080 steel, a linear fit of the elastic region was done and the elastic modulus was found to be 190.46 GPa and 170.89 GPa for test 474-5 and 474-6, respectively. An offset of .6% was chosen to approximate the yield stress, instead of the .2% used in 1080 steel. This was done due to VascoMax 300 having a relatively high yield stress, which is close to its ultimate yield strength [11]. Figure 45 shows the determination of A for test 474-5. A similar plot is shown in Appendix 4 for test 474-6.

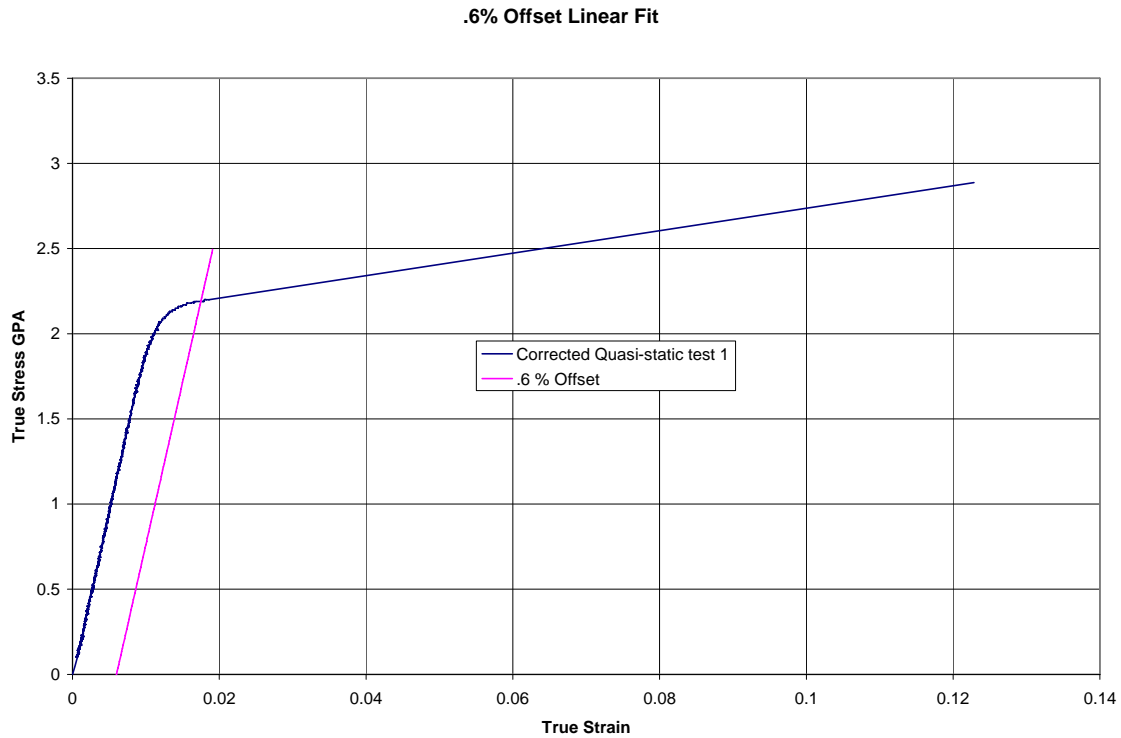


Figure 45 - VascoMax 300 Quasi-static test 474-5

The plastic regions of the quasi-static tests were fitted using B and n. Unlike the 1080 steel quasi-static tests, VascoMax 300 did not have a non-linear plastic region due to the nature of the correction needed for VascoMax 300. Instead, only a linear line needed to be approximated for the plastic region. By finding the ESD in the same manner as 1080 steel was, the plastic strain was determined by using the linear equation from the plastic region correction with the ESD. Again, a log plot of ESD versus strain was used to find B and n. Figure 46 and Figure 47 shows the results of this effort. Note that the stress and strain values in these two figures are ESD and plastic strain, respectively.

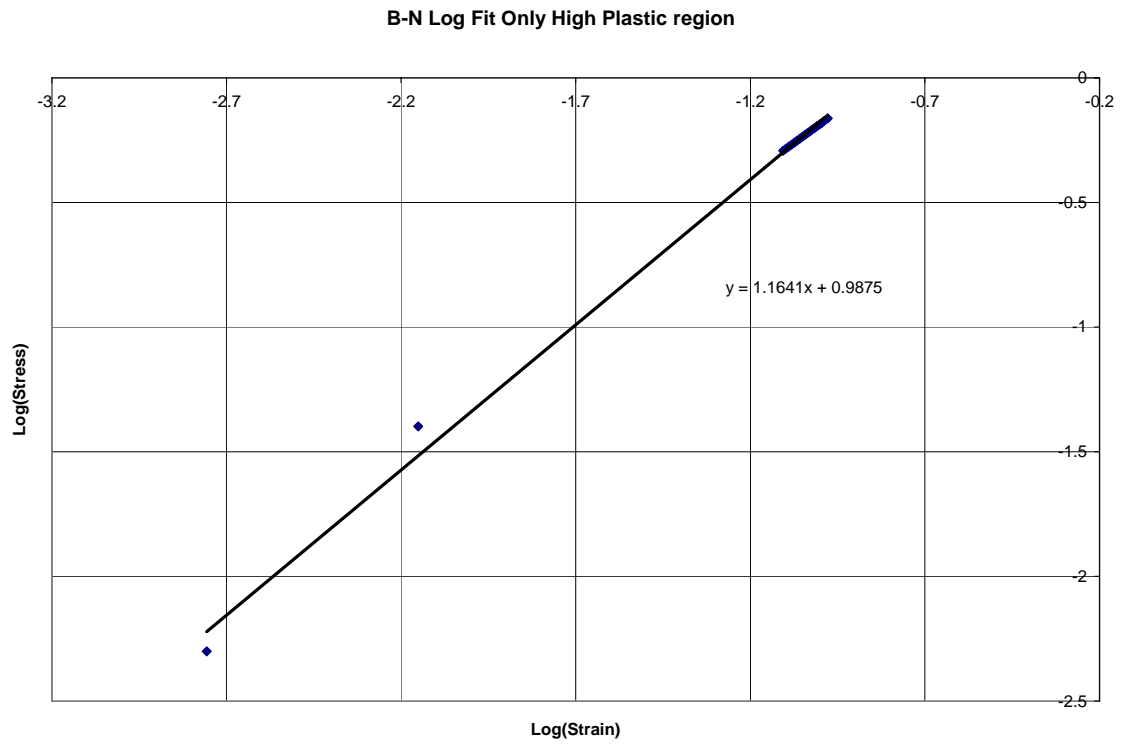


Figure 46 – Plastic Region Fit of VascoMax 300 test 474-5

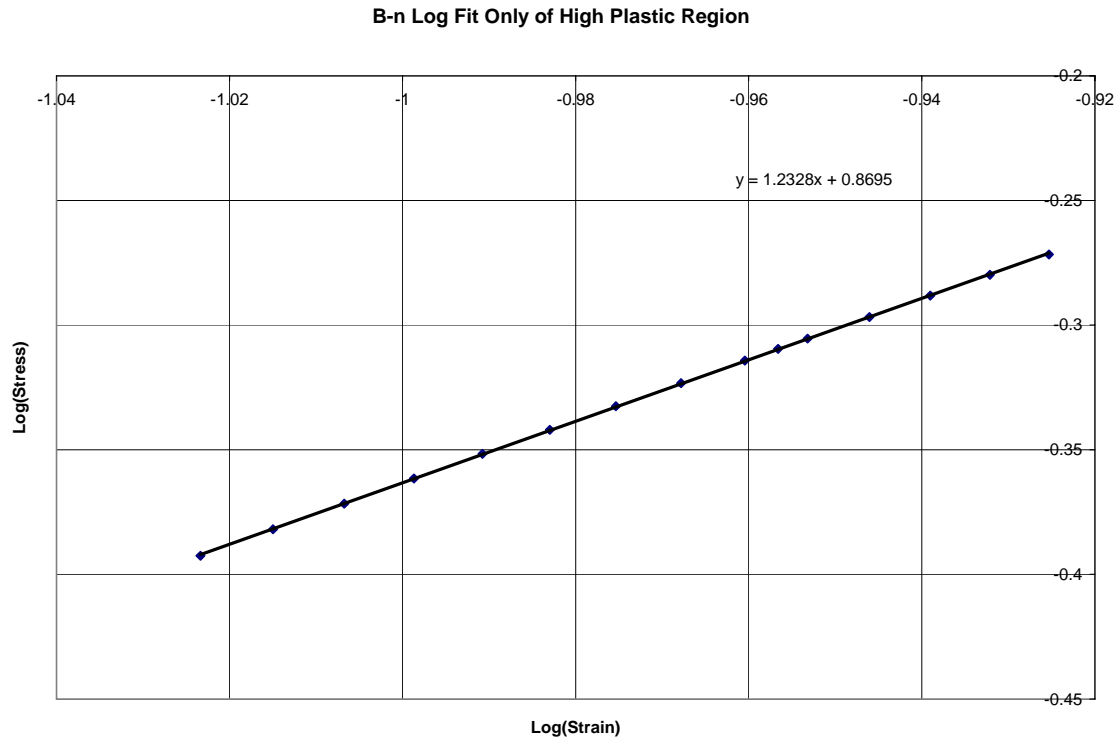


Figure 47 - Plastic Region Fit of VascoMax 300 test 474-6

It should be noted here that linear equations for the plastic regions of all tests, both dynamic and quasi-static, were found to allow determination of the flow stress at any strain. This fact was mentioned before in the correction of the VascoMax 300.

The C coefficient was found in similar fashion to the process used in 1080 steel. However, for VascoMax 300, no interpolation was needed to describe the flow stress at a certain strain due to the plastic region being purely linear. From the curve fit of A, B, and n coefficients, the proper strain to measure flow stress at was at 0.07. This reason is discussed is same as discussed for 1080 steel. A strain of 0.07 provided the best fit from the Johnson-Cook model for the two quasi-static tests. Appendix contains the two plots depicting the curve fit of the quasi-static tests. Also, a table describing the flow stresses

at certain strain rates for 0.07 strain are provided in Appendix 4. Figure 48 depicts the determination of C.

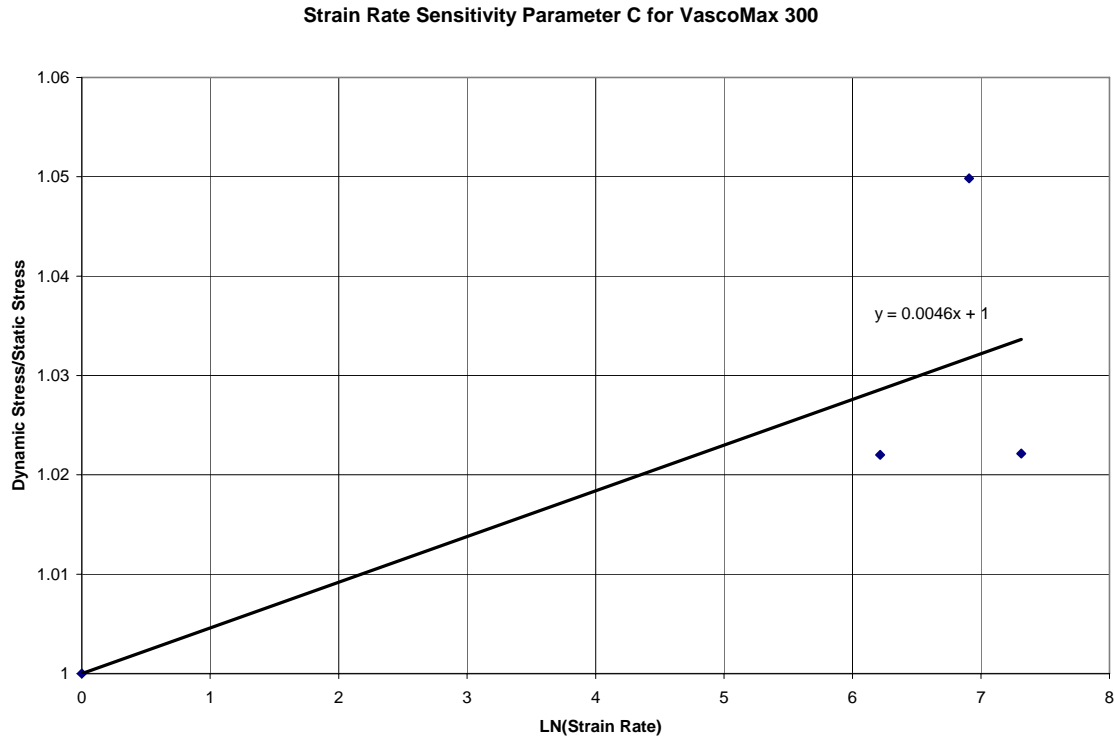


Figure 48 - Strain Rate Sensitivity of VascoMax 300

This work found that 0.0046 represented the strain rate sensitivity parameter for VascoMax 300.

As in 1080 steel T^* is just the homologous temperature at certain test temperatures. The melting temperature for VascoMax 300 is $2575^{\circ}F$ and is reported in the UDRI report [14]. Using the linear equations describing the plastic regions of the dynamic tests, flow stress values were obtained at 0.07 strain. Plotting

$\log(1 - (\sigma_{dynamic} / \sigma_{static}))$ vs. $\log(T^*)$ for each strain rate determined the m

coefficient. Figure 49 shows the m coefficient found for VascoMax 300 at 500/s. All

plots for the determination of m for VascoMax 300 associated tables are shown in Appendix 4.

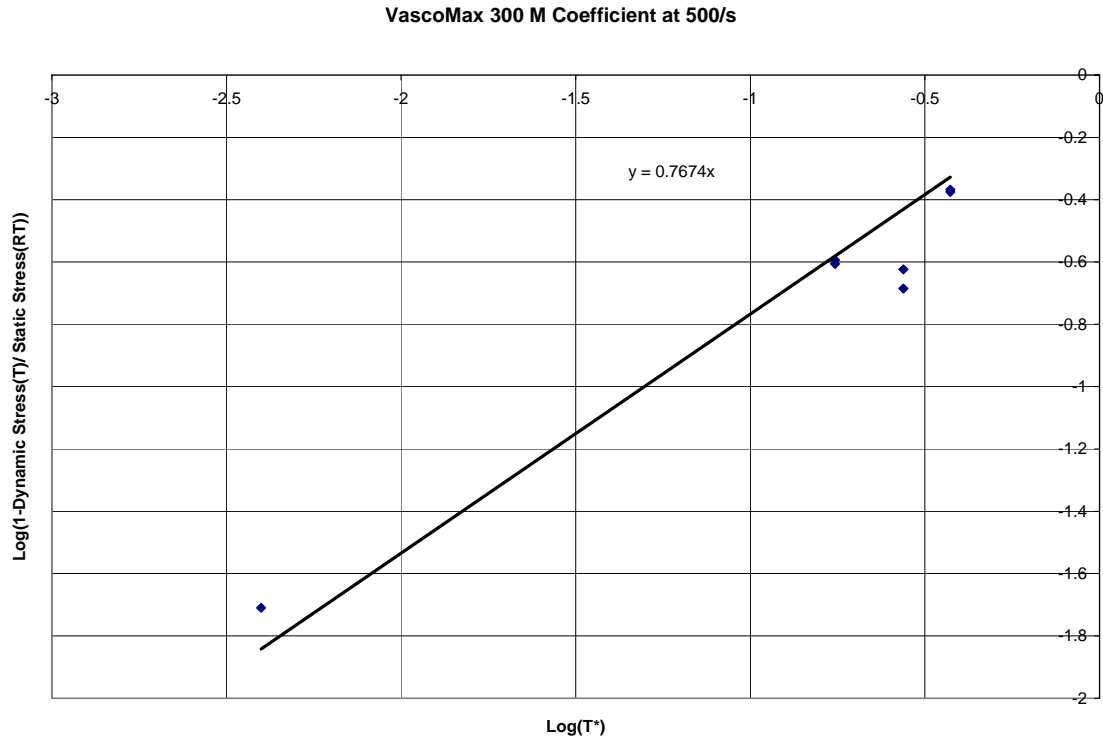


Figure 49 - m Coefficient for VascoMax 300 at 500/s

Here it is shown that the m coefficient for VascoMax 300 at 500/s is .7674. The average value from all three tests is .7799.

As for 1080 steel, UDRI constructed its own Johnson-Cook constitutive model for VascoMax 300. Table displays the results of this work and UDRI's coefficients.

Table 6 - J-C Coefficients for VascoMax 300

Test Facility	Test Number	A (GPa)	B (GPa)	n	C	m
AFIT	474-5	2.2	9.7163	1.1641		
	474-6	2.14	7.369	1.2306		
	Average	2.17	9.4	1.175	0.0046	0.7799
UDRI	474-5	2.120	2.420	0.322		
	474-6	2.030	1.540	0.510		
	Average	2.070	1.980	0.416	0.006	1.41

For the yield stress, both studies found similar values and represents a good verification of the yield limit. However, the other coefficients fail to agree between the two studies. UDRI based their values on the original stress-strain curves obtained and hence their coefficients in the plastic region are based upon the negative slope seen in all VascoMax tests. This work attempted to correct the VascoMax data to account for the necking in the specimens before failure. This correct allowed this study to produce more accurate coefficients and will be displayed in chapter 4 through the use of the CTH model of the Taylor test.

As used for 1080 steel, the method of examining the effects of dynamic loadings is to plot the flow stress at a certain strain. By plotting the flow stresses versus the strain rate, a graphic estimation of the curve fit is obtained. Figure 50 shows the results of this works ability to curve fit the VascoMax 300 data a certain strain. This strain, 0.07, is the same used to examine the C and m coefficients. This strain was chosen in similar fashion to that in 1080. It provided the flow stress where the Johnson-Cook model for VascoMax 300 fit the quasi-static data. Again, this work was with strain rate data and could not confirm a value of strain from dynamic relations as mention in before in the 1080 analysis.

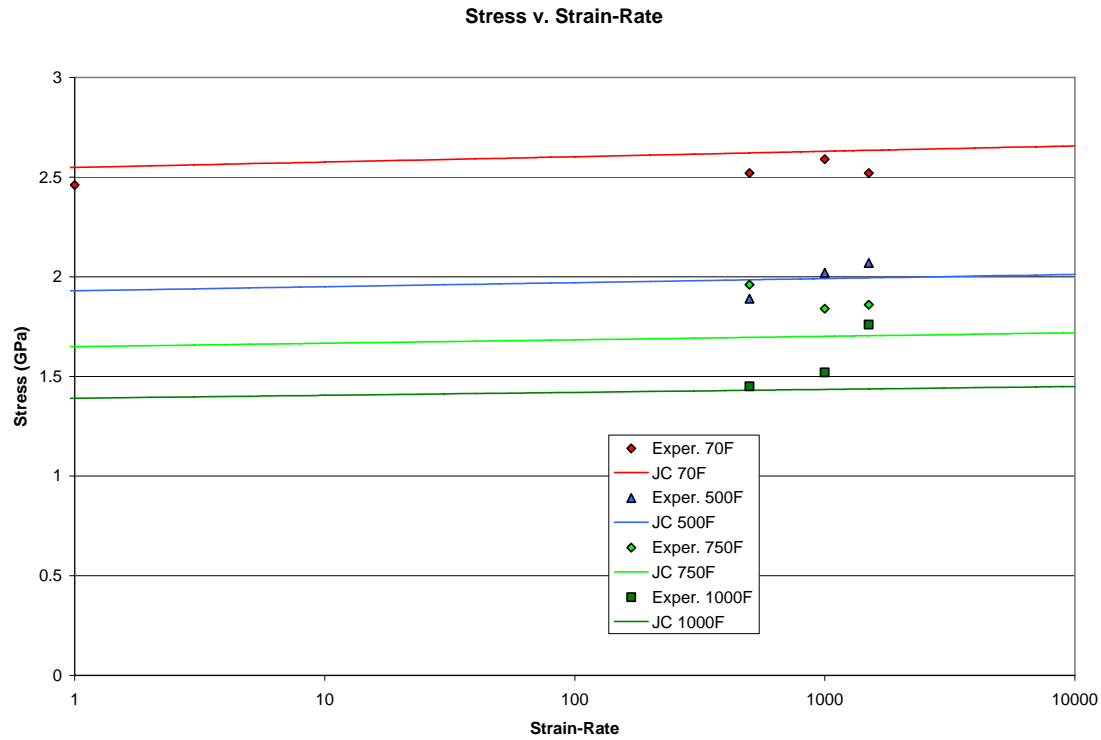


Figure 50 - VascoMax 300 J-C Fit of Dynamic Loading

As with the 1080 steel, excellent agreement exists with the effects of temperature and strain rate on the Johnson-Cook model. It shows that at higher temperatures, the model shows a decrease in flow stress. Also, the experimental data reflects this trend. At higher strain rates, the flow stress increases for both the model and the experimental data. In addition the model approximates the experimental flow stresses very well for all temperatures and strain rates. However, due to the nature of the corrected data and the linear slope of the plastic region, it is expected that the model would be able to fit the data without much deviation. As with the 1080 steel, UDRI's Johnson-Cook model of VascoMax 300 is displayed to emphasize the necessity of the data correction undertaken by this work and the reason why a different strain was chosen to examine flow stress at

for the dynamic and temperature effects on VascoMax 300. Figure 51 displays UDRI's model.

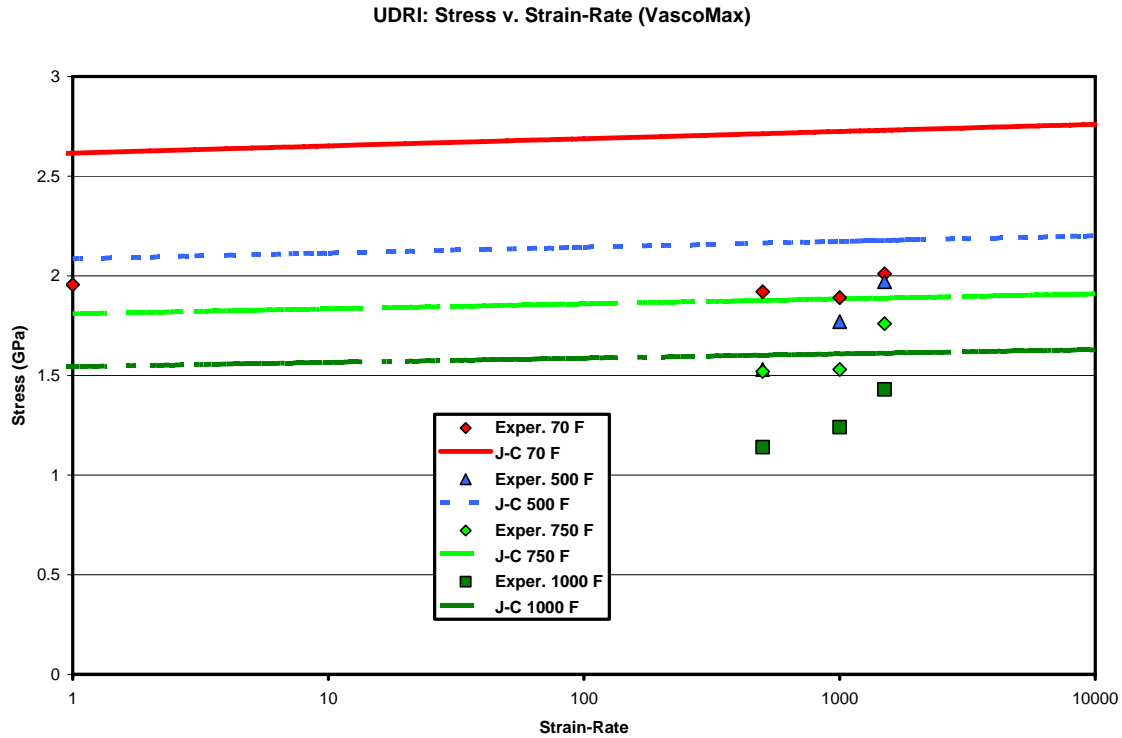


Figure 51 – UDRI VascoMax 300J-C Fit of Dynamic Loading

As with the 1080 steel, it is shown that this work was able to produce a more accurate approximation of the flow stress data for VascoMax 300. Here, UDRI overshoot the intended flow stress values they examined at 0.06 strain. This provides further evidence that this work's data correction yield a stress-strain relation that the Johnson-Cook model could define without much deviation.

When the Johnson-Cook constitutive model is applied to the entire plastic region, there is an underestimation of the flow stress, as with the 1080 steel. Again, we have the same amount of deviation from the experimental data due to the equal dependence of all

strain rates and temperatures. Figure 52, Figure 53 and Figure 54 displays the results of the Johnson-Cook model to fit the VascoMax data at 500/s at all three temperatures.

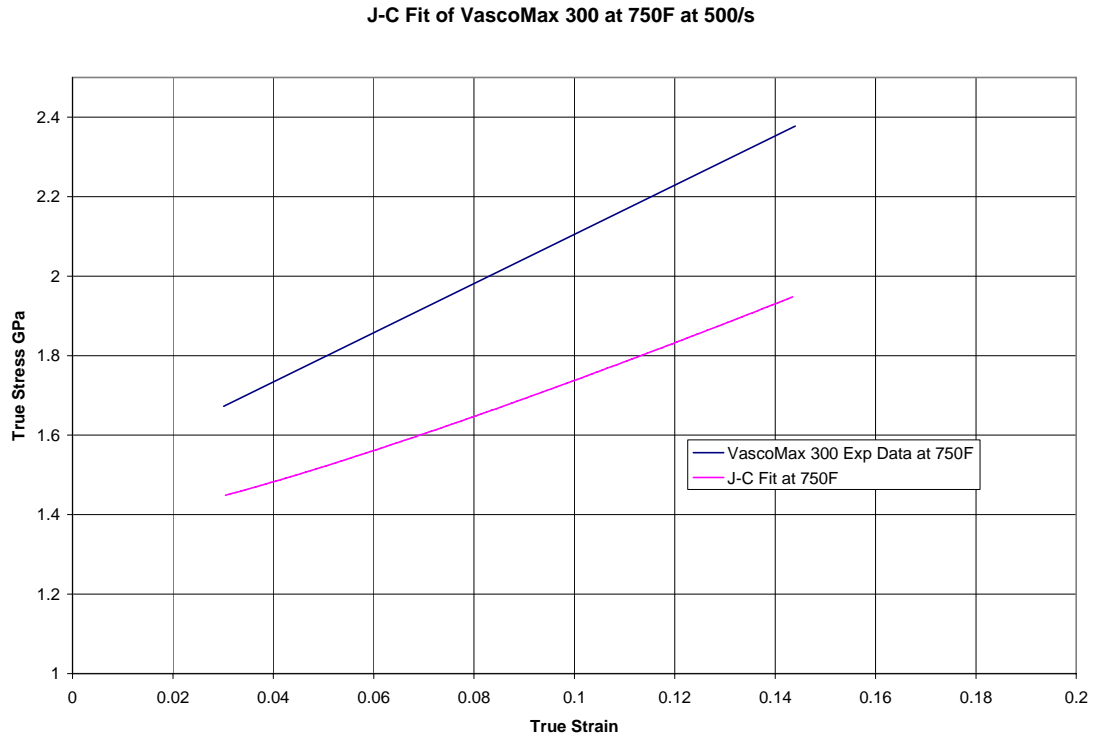


Figure 52 - J-C Fit of VascoMax 300 at 750F at 500/s

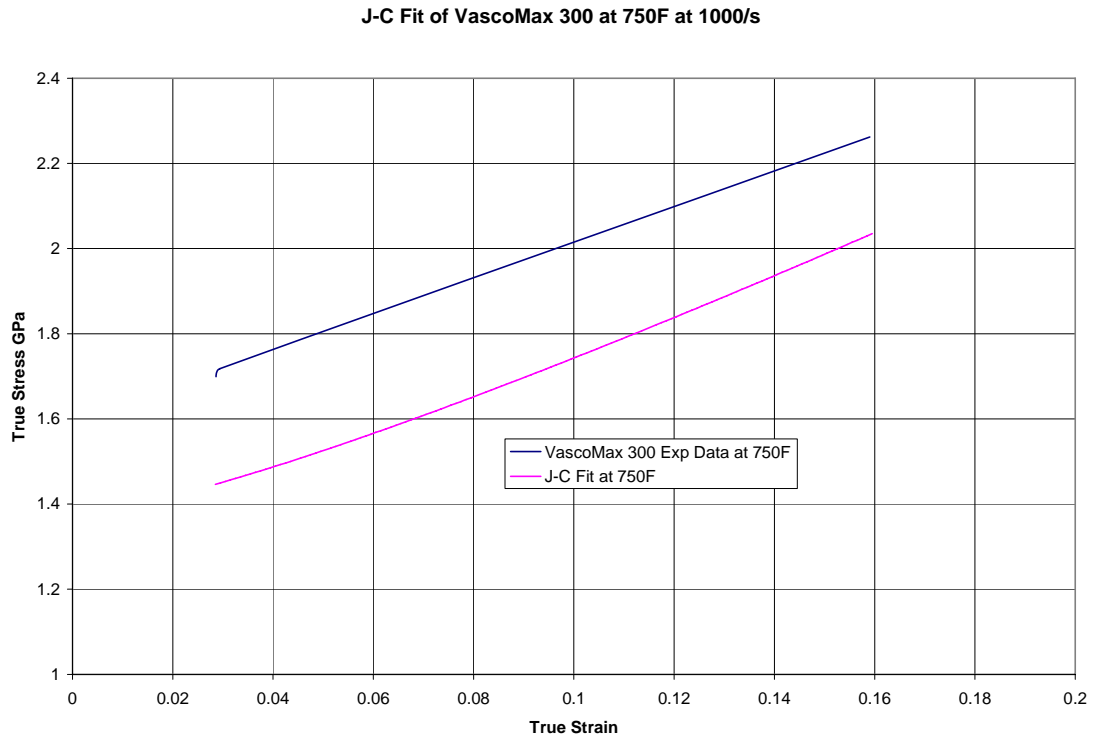


Figure 53 - J-C Fit of VascoMax 300 at 750F at 1000/s

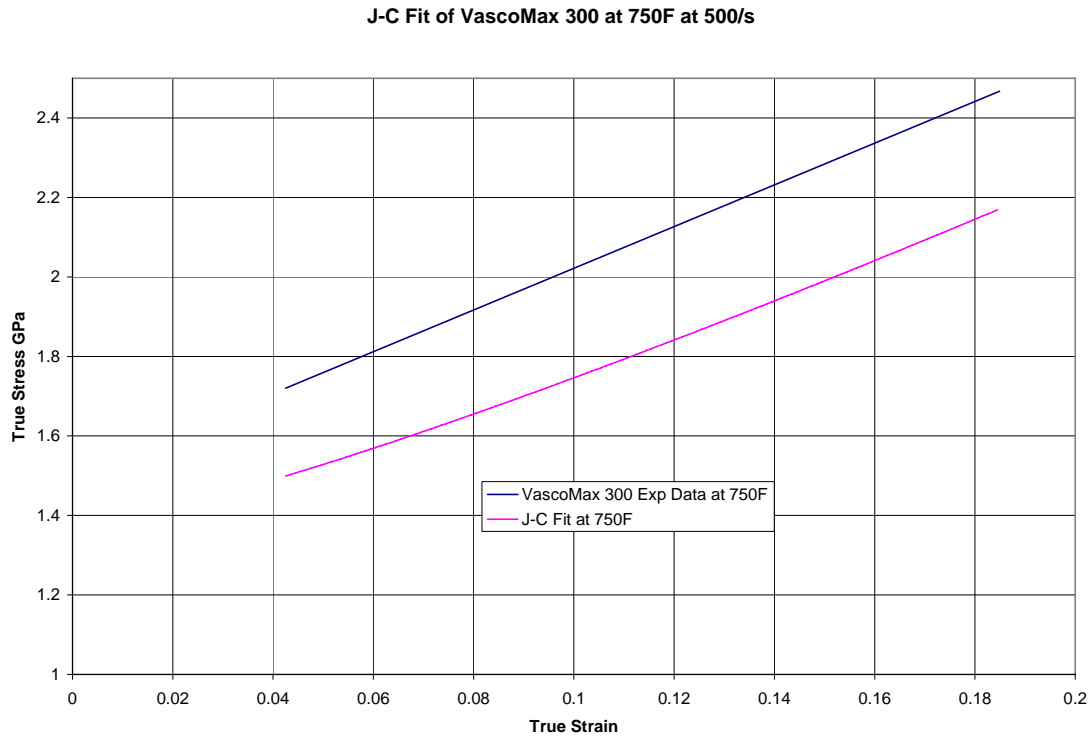


Figure 54 - J-C Fit of VascoMax 300 at 750F at 1500/s

From these three plots of this study's Johnson-Cook model for VascoMax 300, it is shown that the model provides a fair approximation of the experimental data for all three strain rates at constant temperature. However, the model does have a constant undershoot for all three cases. This is likely due to the correction of the data for VascoMax 300 and the inability of the Johnson-Cook model to approximate the data acquired from a linear line, rather than a normal stress-strain curve. However, it will be shown in chapter 4 that this model is able to yield excellent results when it is input in CTH for comparison to Taylor tests conducted.

Chapter 4 – Evaluation of the Johnson-Cook Coefficients for 1080 steel and VascoMax 300

4.1 Taylor Test and CTH Model

The Taylor test is a relatively simple test utilizing a thin rod impact on a rigid wall, as described in chapter 2. This test was chosen to validate the coefficients determined from the SHB test due to its availability to investigators than other costly experiments [17]. However, one of the limitations of the Taylor test is that it can only accurately describe the final deformation without a high speed camera [13]. This work did not have the necessary equipment to take slow motion photography of the deformation during the Taylor test. A camera with a frame rate in excess of 35000-150000 frames per second would capture accurately the deformation over time. Also, there is some concern that the non-uniform stress and strain fields created in the Taylor test produce results that do not accurately depict the material's behavior [16]. However, these facts do not limit the test from producing the results needed to justify the correctness of this work. It will be shown that the relatively low velocities used for both 1080 steel and VascoMax 300 produced symmetric deformation, hence any non-uniform behavior was not evident.

Tests were conducted by Cinnamon at WPAFB, using a gas gun to shoot the specimen rods, both 1080 and VascoMax 300, at a rigid wall made of VascoMax 300. Figure 55 depicts the setup of the Taylor test.



Figure 55 - Taylor Test Experimental Setup

Several tests were run with the 1080 specimens of varying length and velocities. Table 7 shows the results of Cinnamon's work for 1080 steel.

Table 7 - 1080 Taylor Test Results

	From Film	Cylinder Length			Nose Diameter			Undeformed Length
Test #	V_{impact}	L_{init}	L_{final}	ϵL	D_{init}	D_{final}	ϵD	L_{final}
	(m/s)	(cm)	(cm)	(%)	(cm)	(cm)	(%)	(cm)
S3	212	3.000	2.735	8.83	0.600	0.810	35.00	1.443
S6	154	3.000	2.844	5.20	0.600	0.697	16.17	1.71
S9	145	5.995	5.719	4.60	0.589	0.660	12.05	4.226
S8	123	5.991	5.774	3.62	0.600	0.652	8.67	3.996
S2	126	6.000	5.746	4.23	0.600	0.675	12.50	4.132
S11	103	9.001	8.724	3.08	0.595	0.640	7.56	6.562

From this table, only test S8 and S9 were used for justifying the Johnson-Cook Coefficients for 1080 steel. These tests did not experience buckling or asymmetric deformation and allowed an easy comparison to the CTH model, which utilized a 6 cm specimen. The three parameters, change in length, change in nose diameter, and undeformed length were compared to the CTH results and are provided later in this

chapter. It should be noted here that Cinnamon used a micrometer to define the undeformed length for all specimens. He felt that his measurements were accurate within 0.1 mm. This will be discussed further in comparison of the CTH model versus real world Taylor test in evaluating the undeformed length. For the testing of VascoMax 300, a similar table of tests is shown in Table 8. Again only two tests were selected to model.

Table 8 - VascoMax 300 Taylor Test Results

	From Film	Cylinder Length			Nose Diameter			Undeformed Length
Test #	V_{impact}	L_{init}	L_{final}	ϵL	D_{init}	D_{final}	ϵD	L_{final}
	(m/s)	(cm)	(cm)	(%)	(cm)	(cm)	(%)	(cm)
V5	77	6.008	5.995	0.22	0.589	0.607	3.06	5.993
V6	75	6.006	5.978	0.47	0.593	0.610	2.87	5.89
V7	90	6.004	5.952	0.87	0.601	0.625	3.99	5.81
V11	90	5.991	5.940	0.85	0.588	0.601	2.21	5.34
V12	97	6.003	5.948	0.92	0.599	0.620	3.51	5.27
V13	90	8.992	8.904	0.98	0.593	0.612	3.20	8.33
V15	98	8.993	8.888	1.17	0.586	0.611	4.27	8.35

Test V6 and V7 were selected for the same reasons as S8 and S9. It should be noted that slower speeds had to be used to ensure that the VascoMax 300 rods did not fracture on impact. Even though the deformation for VascoMax was relatively small compared to the 1080 steel, it will be shown the CTH model was able to predict this.

With the real world Taylor experimentation from Cinnamon, a CTH model of a Taylor test was created by Szmerekovsky [18] and Rickerd [1]. Based upon their work, this study utilized their simulation to verify the Taylor tests. Appendix 5 contains the code necessary to run all of the simulations. From the original code developed by Rickerd, this work made modifications to better approximate the Taylor test used in this study. Referring to the CTH code in Appendix 5, this work created a mesh for the rod and target block. The mesh for the analysis of the Taylor test was based on a similar design to Rickerd [1] and Blomer [19]. Figure 56 displays the general layout of the mesh

used in CTH. Cells with dimensions of 0.01 cm were used near the impact area due to deformation concerns and 0.1 cm cells were used for areas of less deformation due to the impact.

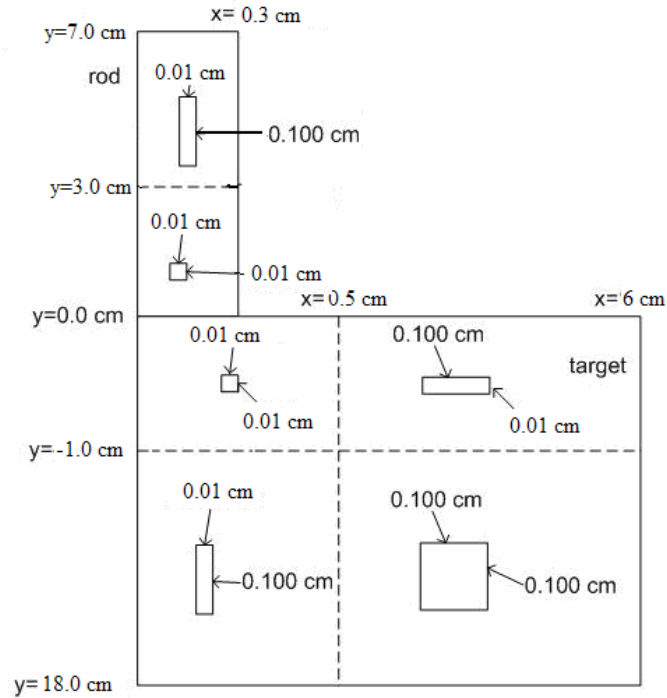


Figure 56 – Taylor Test Grid

A super fine mesh was not needed, due to the interactions between the target block and rod were at relatively low velocities. Also, both steels had relatively high fracture pressure values compared to the stresses present in the CTH runs. It should be noted here that this author chose to set the fracture pressure values to 1.2 times the yield limit for both VascoMax 300 and 1080 steel. The exact values chosen for each metal are shown in Appendix 5. Another parameter that this work incorporated into the code was the velocity of the impact. This is shown in the CTH code as the value of yvel.

When setting up the rod impact in CTH, this author found that better results were obtained when the rod was initially off of the target block at time zero, rather than in contact with the target block. This is due to the fact that the rod does not bounce off of the target block after the end of the impact time found from Cinnamon's experimentation. Even though the rod does not detach from the target block, it will be shown later that the deformation time CTH is approximately the same as the real world tests.

From the SHB data, this work was able to produce coefficients for the Johnson-Cook model. As stated before, CTH allows the insertion of the coefficients of this constitutive model through the command "matep johnson-cook USER". This allows the user to define each coefficient. In order to properly input the coefficients, the A and B coefficients had to be converted from GPa to $\frac{\text{dynes}}{\text{cm}^2}$, which increased each coefficient by a factor of 10. In addition to the constitutive equations, the equations of state needed to be defined. CTH provided the solution to this. The equation of state for VascoMax 300 was already defined within the viscoplastic data file in CTH. For 1080 steel, Rickerd, Blomer, and this author chose the equation of state for Iron to approximate 1080 steel. However, this work found that the temperature of the steels remained relatively low during their deformation in CTH and did not approach their melting temperatures. The temperatures observed in CTH will be explained later in this chapter. Hence, the equations of state for both VascoMax 300 and 1080 steel did not effect the overall deformation with any degree of severity.

The main boundary condition that needed to be defined in this work was the use of the slide condition. Szmerekovsky and Blomer both chose not to use the slide

condition. The slide condition was used in this work to ensure that the interaction of the rod and target block was fluid in nature and not allowed to join in any manner. The slide condition dictates that at the boundary of the two objects, they both take on a fluid property where material is able to enter and exit a cell in the mesh. “Plasticity at the interface developed deviatoric stresses farther from the interface. This option gave good results as well, and matched the experimental conditions that the end of the rod and the target” [1]. It will be shown later that excellent deformation was acquired with the use of the slide condition.

4.2 Verification of the Johnson-Cook coefficients for 1080 steel

This work examined the validity of the Johnson-Cook coefficients and made comparisons with other results to understand the effectiveness of its results. The first CTH runs were done to examine the validity of the final coefficients for 1080 steel that were developed. The final Johnson-Cook coefficients for 1080 steel are restated here for convenience.

Table 9 - 1080 steel Johnson-Cook Coefficients

Test Facility	Test Number	A (GPa)	B (GPa)	n	C	m
AFIT	474-2	0.520	3.300	0.643		
	474-3	0.530	3.880	0.692		
	Average	0.525	3.590	0.668	0.029	0.753

These coefficients were input into the CTH code, shown in Appendix 5 for tests S8 new and S9 new.

It should be noted here that Poisson's ratio was calculated using the elastic modulus from the quasi-static tests and the shear modulus. The elastic modulus was the average from the two tests and found to be 202.84 GPa. The shear modulus is 80 GPa [11]. This produced a Poisson's ratio of 0.27. Another value needed for CTH is T^* . From the equation for T^* in Chapter 2 and restated here for convenience,

$$T^* = \frac{T - T_{room}}{T_{melt} - T_{room}} \quad (59)$$

where T is $70^\circ F$, T_{room} is $60^\circ F$, and T_{melt} is $2550^\circ F$. This yielded a T^* of 0.004016.

To ensure consistence with the tests conducted by Cinnamon, this work chose to use the VascoMax 300 Johnson-Cook coefficients to define the rigid wall material.

Below is a table displaying the final coefficients for VascoMax 300.

Table 10 - VascoMax 300 Johnson-Cook Coefficients

Test Facility	Test Number	A (GPa)	B (GPa)	n	C	m
AFIT	474-5	2.2	9.7163	1.1641		
	474-6	2.14	7.369	1.2306		
	Average	2.17	9.4	1.175	0.0046	0.7799

T^* was chosen to be the same as 1080 steel. Since no shear modulus could be found for VascoMax 300, this work used a Poisson's ratio of 0.283. This value is for VascoMax 250 and represents a close approximation for VascoMax 300.

With all the Johnson-Cook parameters defined for CTH, test S8 and S9 were run using the velocities and rod dimensions defined by Cinnamon. This work chose to produce temperature, plastic strain rate and tracer history plots in addition to the general deformation plots. For test S8, a contact time between the rod and the wall was $63 \mu\text{sec}$, as defined by the real world tests. Below are the CTH deformation frames for the initial

contact at 10 μsec and the final contact time of 70 μsec . Again, this CTH model did not produce a bounce of the rod, so time duration of 60 μsec in CTH yielded an approximate model of test S8. All deformation plots for 1080 steel test S8 are provided in Appendix 6. Due to the volume of plots for all 1080 tests, only test S8 deformation plots with this work's Johnson-Cook model are displayed in Appendix 6. The change in deformation between the tests is too small to appreciate visually.

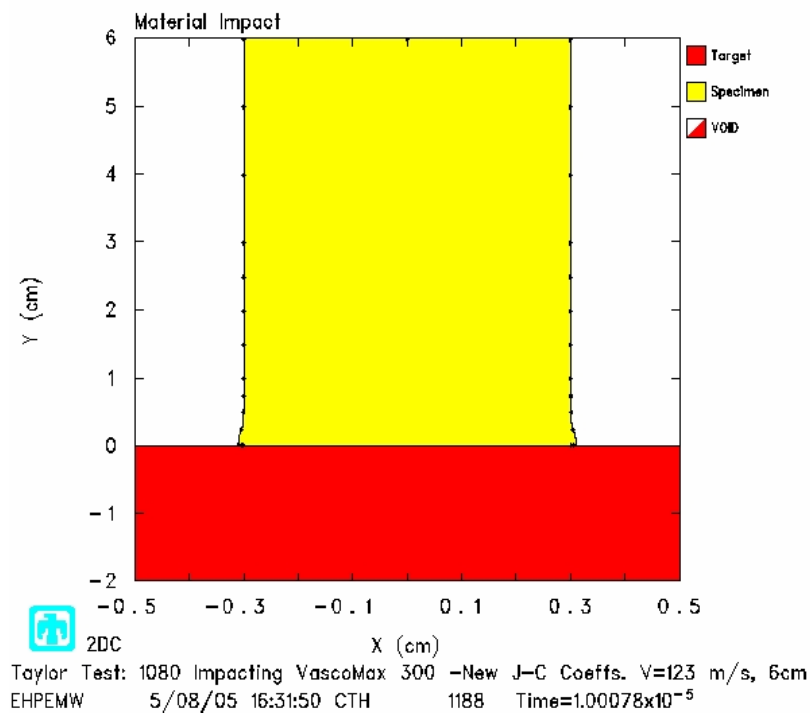


Figure 57 - 1080 Steel test S8 Initial Contact

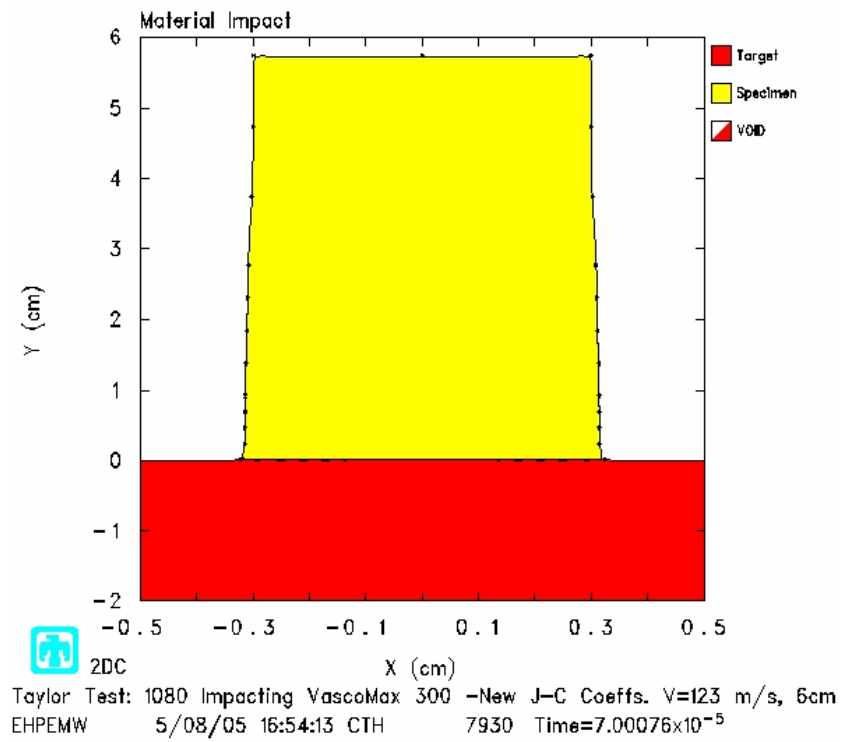


Figure 58 - 1080 Steel test S8 Final Contact

This final frame can be compared to the final deformation of the test done by Cinnamon.

Figure 59 shows a side by side comparison of the CTH model and real world Taylor S8 test.

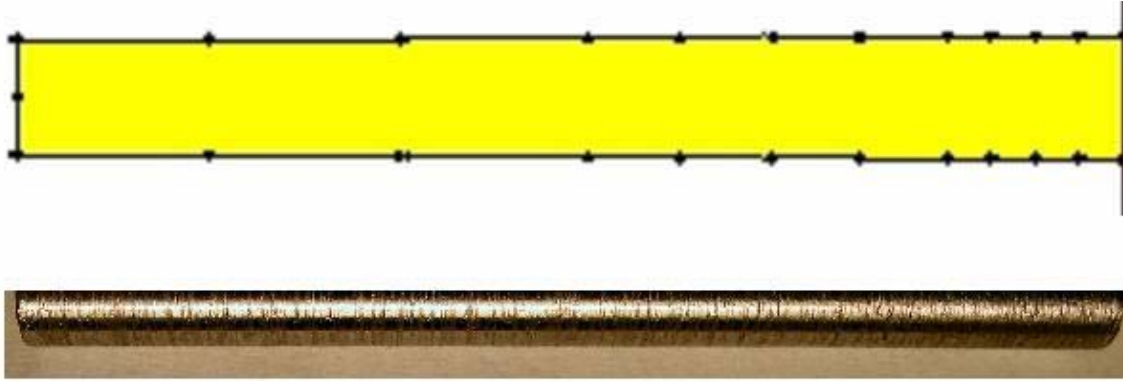


Figure 59 - Comparison of CTH model and Taylor test S8

It is shown here that the CTH model of test S8 approximates the real world test. Notice that the first quarter of both the CTH model and real test rod exhibit most of the total deformation in the specimen.

From this deformation achieved in CTH, this work was able to examine and compare the nose deformation, the change in length and the undeformed length of the specimen in definite values. To do this, 13 tracer points, as defined in the CTH code, were used. Four of these were in equally spaced in the 1 cm of the rod and then spaced at 0.5 cm intervals to 6 cm and one centered at the top. This last tracer point gave the change in length. Figure 60 gives a visual interpretation of the measurements made and the tracer point locations.

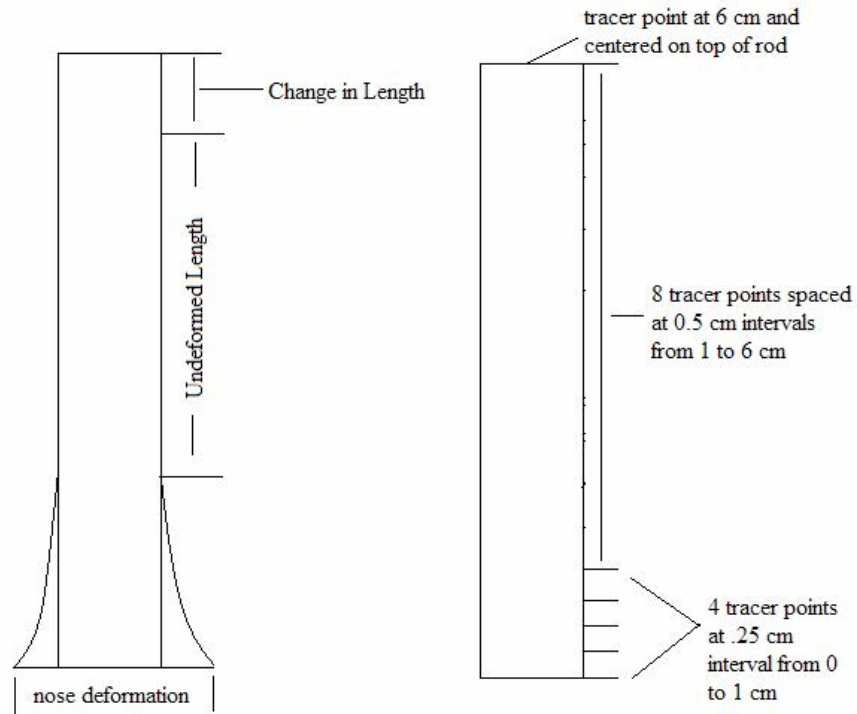


Figure 60 – Rod Diagram

Figure 61, Figure 62, and Figure 63 show the time history plots for deformation at the nose, change in length, and the location where the specimen is considered to have stopped deforming.

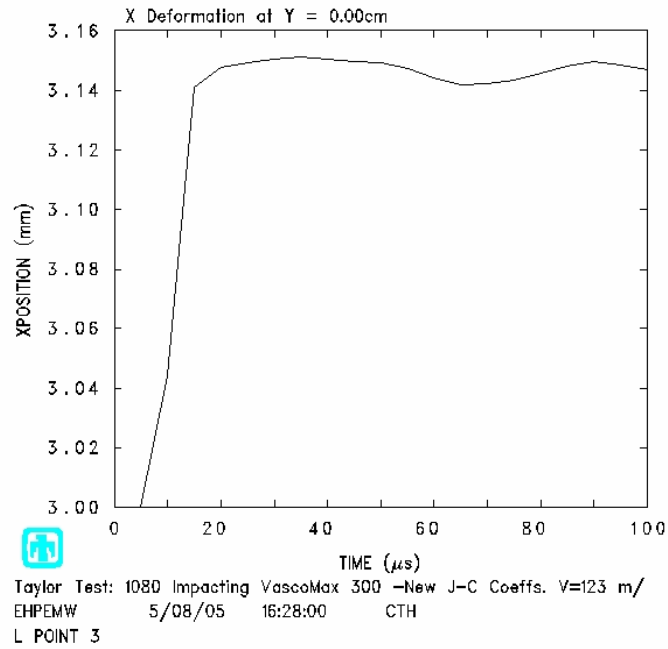


Figure 61 - 1080 steel CTH test S8 Nose Deformation

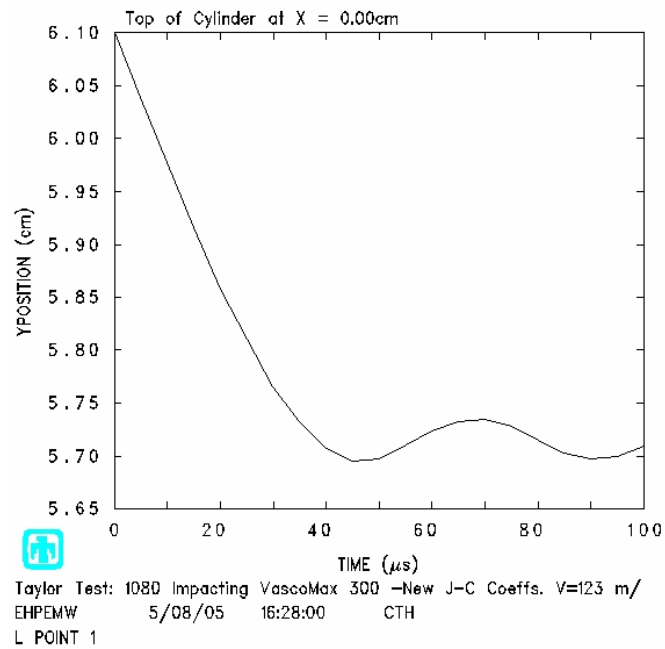


Figure 62 - 1080 steel CTH test S8 Change in Length

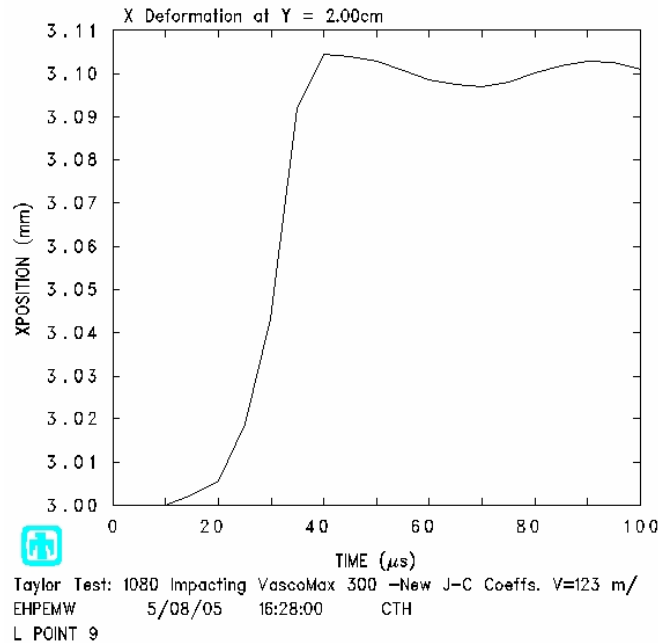


Figure 63 - 1080 steel CTH test S8 Undeformed Length

Again, the change in length plot is determined from the location of the tracer point on top of the rod.

Figure 61 shows the nose deformation to be 0.30 mm at time 70 μ sec . The change in length is approximately 0.26 cm and the location of undeformed length is about 2 cm up from the bottom of the rod. It should be noted here that the change in length is fluctuating somewhat due to CTH's inability to disperse the elastic wave traveling in the rod through heat transfer and other mechanisms. From slow motion photography in Cinnamon's work [17], it is shown that the specimens "ring" or oscillate in shape after the rod has bounced off of the rigid wall. Also, the location of undeformed length is approximate and is chosen in accordance with Cinnamon's accuracy of 0.1 mm deformation measurements. Hence, at 2cm at 70 μ sec , we see a deformation of about 0.1mm, representing the length of the rod that was deformed.

A similar analysis was conducted with test S9. Plots corresponding the nose deformation, change in length, and location of undeformed length for S9 are shown below for convenience. All other time history plots for test S8 and S9 were used only to confirm the location of the undeformed length and are not necessary to explain this analysis.

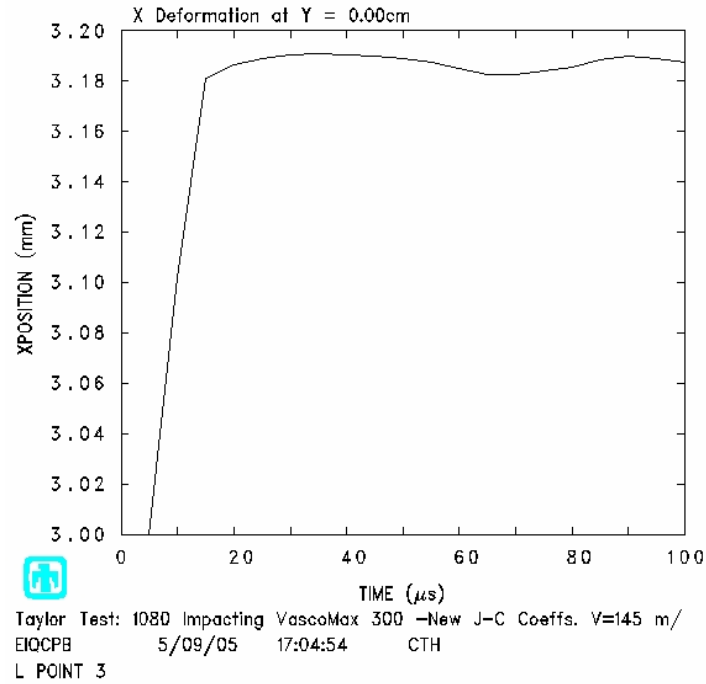


Figure 64 - 1080 steel CTH test S9 Nose Deformation

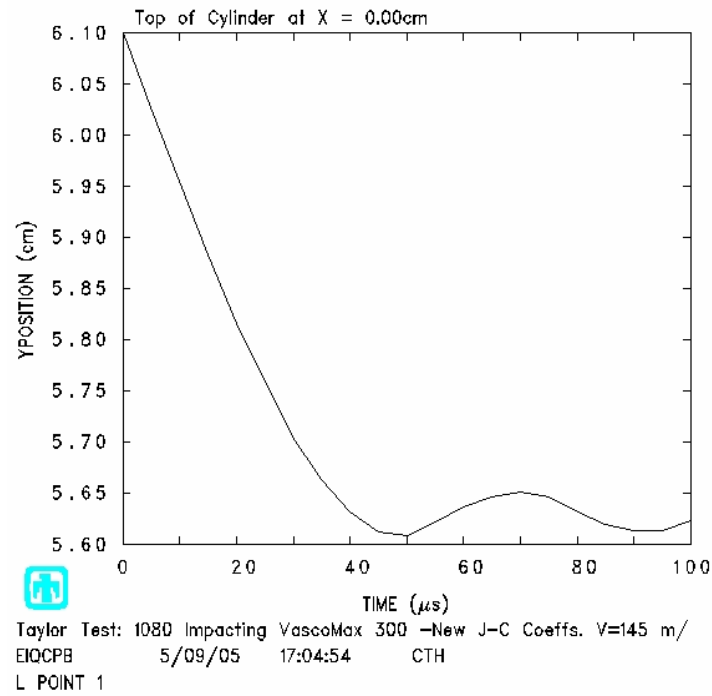


Figure 65 - 1080 steel CTH test S8 Change in Length

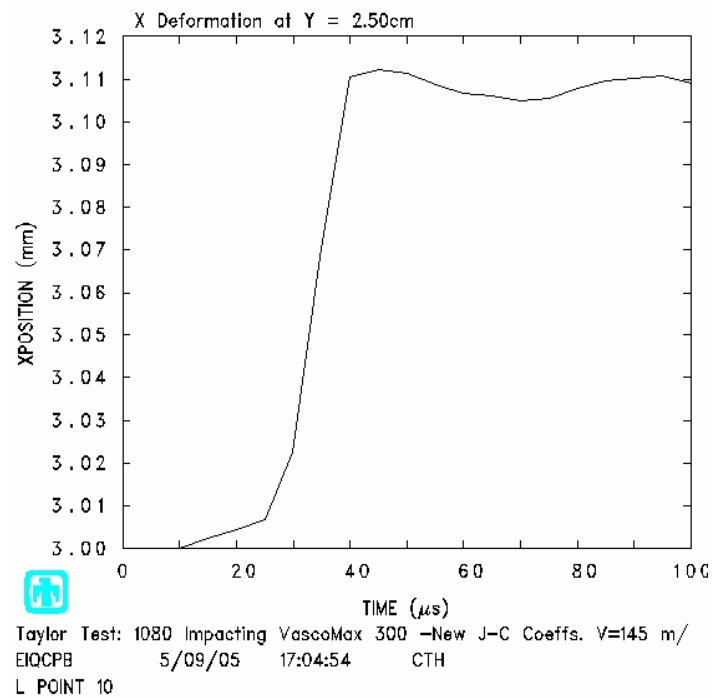


Figure 66 - 1080 steel CTH test S8 Undeformed Length

From these figures for test S9 conducted in CTH, similar results to test S8 are obtained. Again ringing is seen in the change in length plot. For test S9, the undeformed length was decreased due to the increase in impact velocity. The rod deformed about to 2.5 cm up from the bottom of rod. Time history plots of tracer points before and after the tracer point at 2.5 cm are shown Appendix 6 and give justification to why 2.5 cm of deformed length was chosen. With this data, Table 11 was constructed to compare the results of Cinnamon versus those found from the CTH model of 1080 steel. It should be noted that the goal of this work was to be able to reproduce the Taylor tests to within a reasonable difference in the order of 20% of the measured values. This might appear to be a large percentage, but in reality the experiment is dependent upon many factors that are not controllable. For all tables in this chapter, the percent difference for change in length of the cylinder and nose diameter is with respect to the final lengths compared to Cinnamon's results. The undeformed length is the percentage of the cylinder length that was not deformed with respect to its own initial length.

Table 11 - Comparison of 1080 steel Taylor tests

Test Type		From Film	Cylinder Length			Nose Diameter			Undeformed Length
	Test #	V_{impact}	L_{init}	L_{final}		D_{init}	D_{final}		
		(m/s)	(cm)	(cm)	(%)	(cm)	(cm)	(%)	(%)
Cinnamon	S9	145	5.995	5.719		0.589	0.660		70.49
	S8	123	5.991	5.774		0.600	0.652		66.70
CTH	S9	145	6.000	5.620	1.73	0.600	0.640	3.03	58.33
	S8	123	6.000	5.740	0.59	0.600	0.630	3.37	66.67

The overall results of this comparison are excellent for what this work was challenged to do. For test S8, CTH was able to reproduce the change in length result with only a difference of 1.73 percent. This small difference is seen as well for nose diameter where this work's Johnson-Cook model for 1080 steel was 3.37% off of the Taylor tests.

Outstanding results for undeformed length were achieved with only a 0.03% difference. However, at a slightly increased velocity used in test S9, percent differences between the CTH model and the Taylor tests were increased. Good results for change in length for test S9 were observed, with only a 1.73% difference. This was not true for undeformed length. The CTH model of test S9 was off by 12.16% for undeformed length. All of these differences are within the desired range of 20%, but test S9 suggests that at greater velocities than used in this work, the results produced by CTH would be outside of accepted range. This increasing percent difference could be mitigated by determining the Johnson-Cook coefficients for 1080 steel that better approximate higher strain rates, rather than equally curve fitting all of the strain rate tests.

As stated in chapter 3, a correction was made to the 1080 steel coefficients to exclude strain past 0.08. To examine the effects of making such a correction, this work ran the S8 and S9 tests for 1080 steel with the uncorrected Johnson-Cook coefficients. Table 12 displays the Johnson-Cook coefficients for 1080 steel for both final value without strain past 0.08 and those including strain higher than 0.08.

Table 12 - 1080 steel J-C Coefficients with and without 0.08 Strain

Test Number	A (GPa)	B (GPa)	n	C	m
Old Average	0.520	3.270	0.660	0.029	0.753
Final Average	0.525	3.590	0.668	0.029	0.753

With both sets of coefficients used in the CTH model, values of deformation were found and are displayed in Table 13.

Table 13 - 1080 steel Deformation Comparision

Test Type		From Film	Cylinder Length			Nose Diameter			Undeformed Length
	Test #	V_{impact}	L_{init}	L_{final}		D_{init}	D_{final}		
		(m/s)	(cm)	(cm)	(%)	(cm)	(cm)	(%)	(%)
Cinnamon	S9	145	5.995	5.719		0.589	0.660		70.49
	S8	123	5.991	5.774		0.600	0.652		66.70
CTH	S9 final	145	6.000	5.620	1.73	0.600	0.640	3.03	58.33
	S8 final	123	6.000	5.740	0.59	0.600	0.630	3.37	66.67
CTH	S9 old	145	6.000	5.610	1.91	0.600	0.640	3.03	58.33
	S8 old	123	6.000	5.700	1.28	0.600	0.631	3.22	66.67

From this table we see that the differences between the deformation values with and without strains higher than 0.08 are negligible or non-existent. Hence, the quasi-static portion of the Johnson-Cook model, specifically coefficients B and n, effect the overall deformation by only a small amount when they are changed slightly. This means that large modifications to B and n are needed to see measurable changes in deformation.

4.3 Verification of the Johnson-Cook coefficients for VascoMax 300

As with the 1080 steel, this work conducted CTH runs to understand the accuracy of the Johnson-Cook coefficients developed for VascoMax 300. Again, two tests were chosen from Cinnamon [17] to model in CTH. Test V6 and V7 were selected from Table 8 due to their initial cylinder dimensions and symmetric deformation. Using the CTH code described in verifying the 1080 steel results, this work modeled the VascoMax 300 tests by only changing the velocity of the rods, the equations of state, and the coefficients found from the SHB analysis. Table 10 states the coefficients for VascoMax 300.

VascoMax 300 tests V6 and V7 had equal impact duration of 42 usec. This work therefore chose to examine only the deformation described from CTH between 10 μsec

and $55\ \mu\text{sec}$. Again $10\ \mu\text{sec}$ is the approximate time of initial contact between the rod and the rigid wall. Below is the initial and final deformation described by the CTH model of test V7.

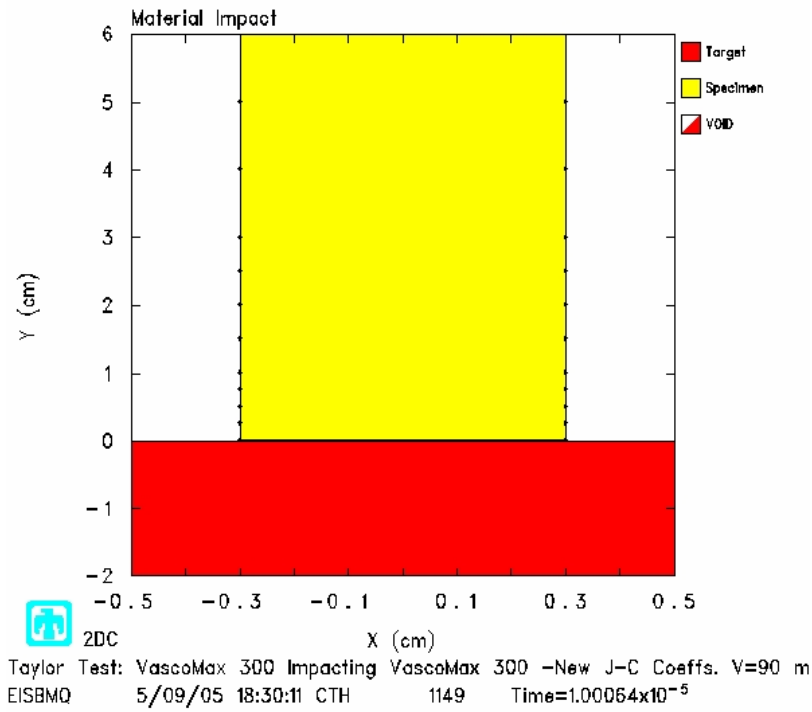


Figure 67 - VascoMax 300 test V7 Initial Contact

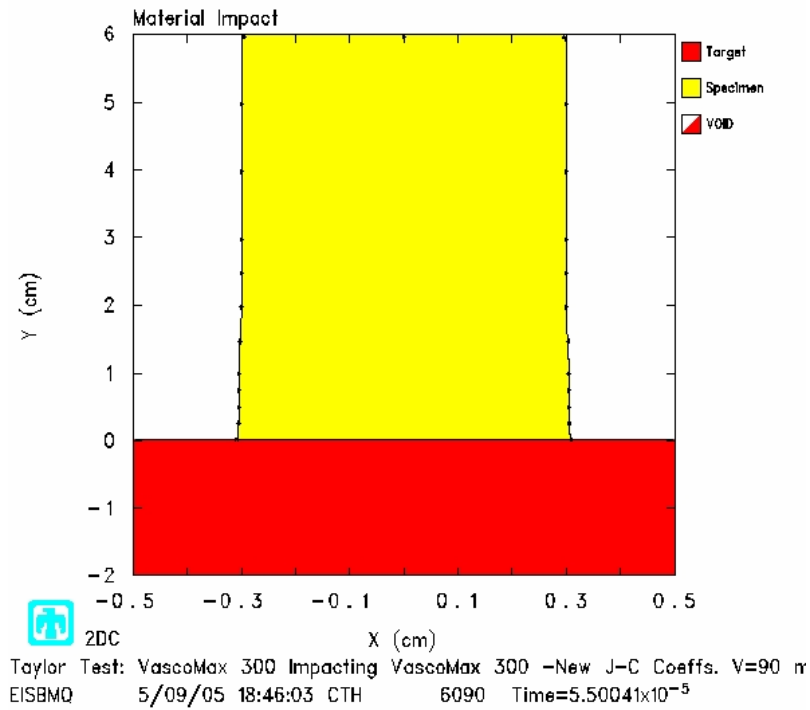


Figure 68 - VascoMax 300 test V7 Final Contact

From these two figures, it is seen that the total deformation of VascoMax 300 is very small compared to the results seen in 1080 steel. This is in agreement with the initial knowledge of VascoMax 300's material behavior; specifically that has a high yield limit due to the heat treatment the steel undergoes. A visual comparison between Cinnamon's test V7 rod and this work's CTH model of V7 is shown in Figure 69 [17].

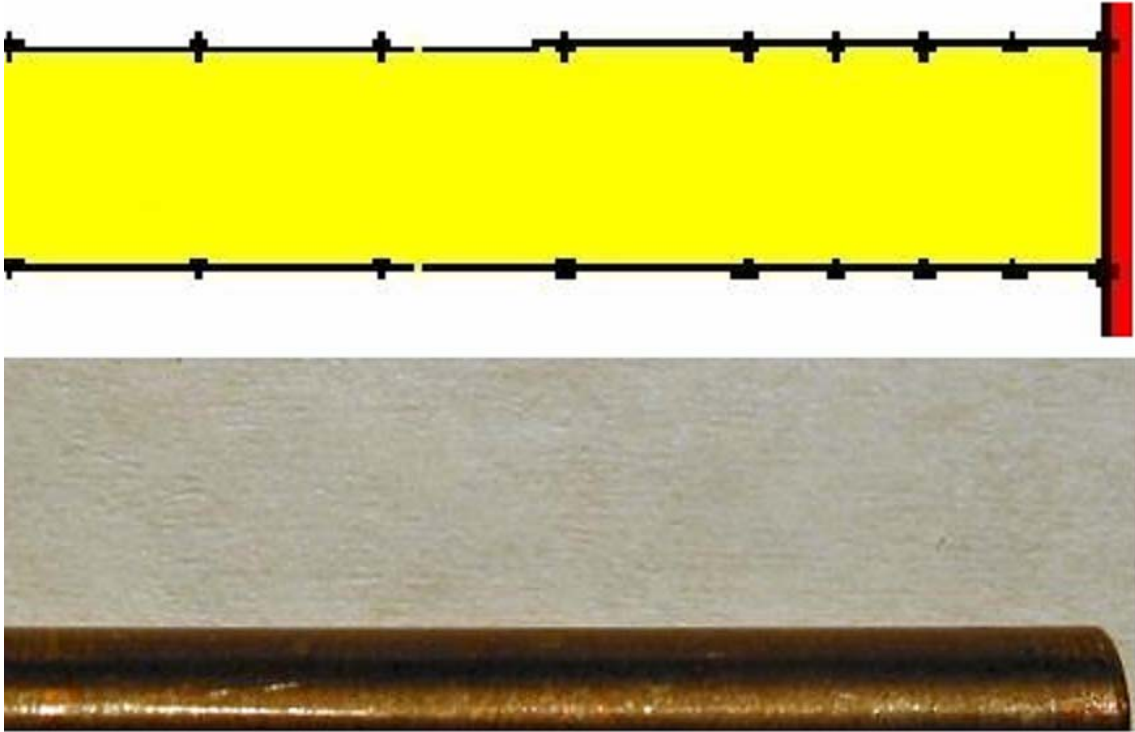


Figure 69 – Comparison of CTH model and Taylor test V7

This figure depicts the difficulty in visually explaining the deformation. To understand the deformation of VascoMax 300 a more accurate method was needed. As stated earlier, this work utilized tracer points in CTH to define values of deformation at certain locations. Figure 70, Figure 71, and Figure 72 show the nose deformation, change in length and undeformed length characteristics of test V7. Due to the slight change in deformation between test V7 and V6, V6 deformation plots are not needed to understand the results obtained.

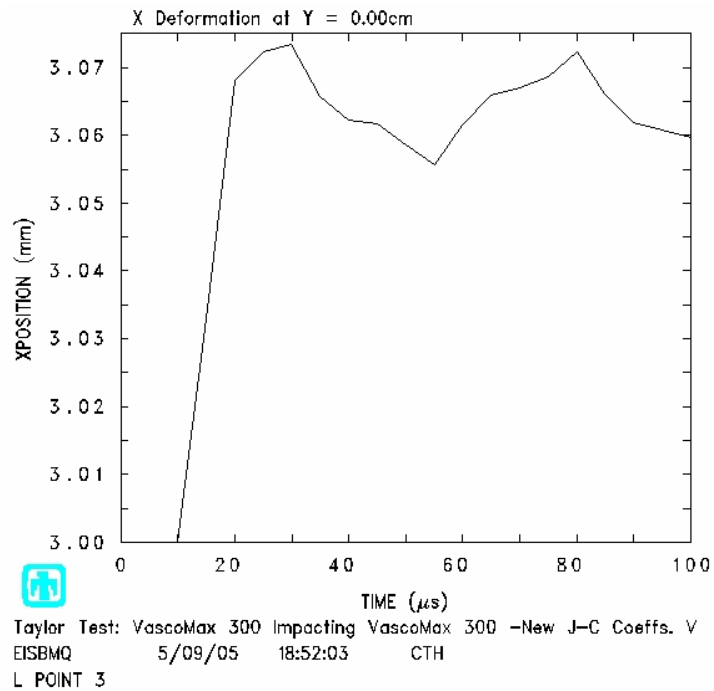


Figure 70 – VascoMax 300 CTH test V7 Nose Deformation

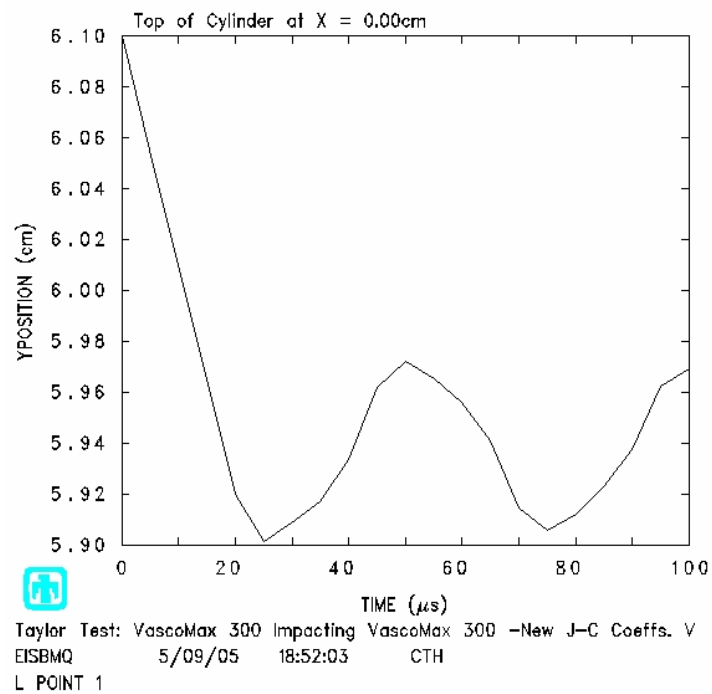


Figure 71 - VascoMax 300 CTH test V7 Change in Length

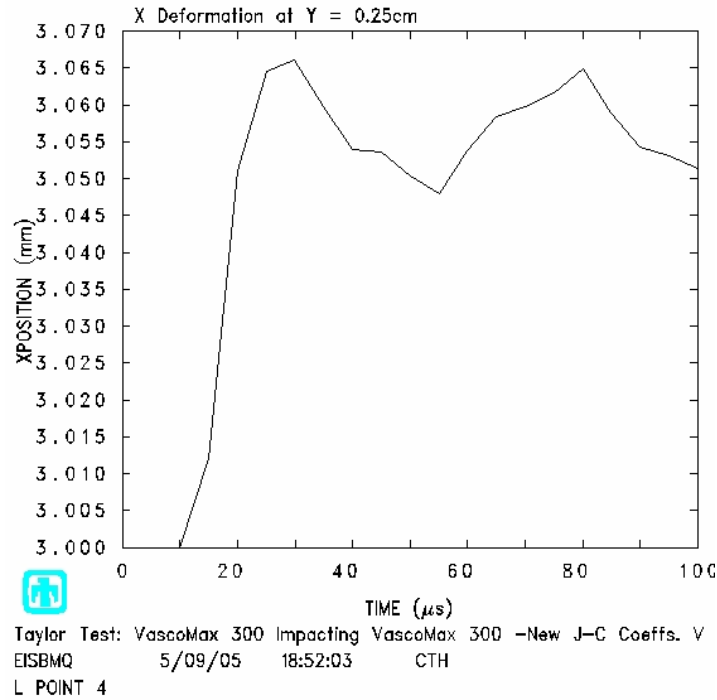


Figure 72 - VascoMax 300 CTH test V7 Undeformed Length

These figures display the initial analysis that VascoMax 300 deformed very minutely. For nose deformation at 55 μ sec, this CTH model produced only 0.12 mm change in diameter. A change in length of 0.03 cm and an undeformed length of 5.75 cm is observed from the above plots. It should be noted that accuracy was within 0.1 mm variation due to personal observation, but it is shown that the deformation in CTH test V7 never exceeded this value. This author felt that deformation after the 0.25 cm tracer point in CTH was negligible from the accuracy statement above and that the rod did undergo a measurable amount of deformation before the 0.25 cm tracer point. These results for test V7, along with those found in test V6 are displayed in Table 14.

Table 14 - Comparison of VascoMax 300 Taylor tests

Test Type		From Film	Cylinder Length			Nose Diameter			Undeformed Length
	Test #	V_{impact}	L_{init}	L_{final}		D_{init}	D_{final}		
		(m/s)	(cm)	(cm)	(%)	(cm)	(cm)	(%)	(%)
Cinnamon	V6	75	6.006	5.978		0.593	0.610		98.07
	V7	90	6.004	5.952		0.601	0.625		96.77
CTH	V6	75	6.000	5.985	0.12	0.600	0.608	0.33	97.50
	V7	90	6.000	5.970	0.30	0.600	0.612	2.08	95.83

From this table, the results of both CTH tests V6 and V7 show excellent approximation of the tests conducted by Cinnamon. A difference of less than 0.5% for change in length was seen for both CTH tests when compared to their equivalent real world Taylor test. This trend is also seen in nose diameter and undeformed length where the differences were approximately 2% and 1% respectively for both CTH tests. From an initial analysis of the VascoMax 300 CTH models, this work shows that the Johnson-Cook coefficients produced effectively define the material behavior of VascoMax 300, even though the steel's stress-strain relations were corrected for necking that occurred during the SHB tests. It should be noted here that the tests for VascoMax 300 were conducted at relatively low velocities of 75 m/s and 90 m/s. The tests were limited to these velocities to ensure proper deformation without fracture and total failure of the VascoMax 300.

To further justify the Johnson-Cook coefficients developed by this work, a comparison between this work and the coefficients developed by UDRI was analyzed. Using the same CTH code stated earlier, this work input the coefficients from UDRI and ran a simulation of the V6 test parameters. Table 15 displays the deformation values of Cinnamon, this work, and UDRI coefficients for test V6.

Table 15 - Comparison of VascoMax 300 Taylor Tests

Test Type		From Film	Cylinder Length			Nose Diameter			Undeformed Length
	Test #	V_{impact}	L_{init}	L_{final}		D_{init}	D_{final}		
		(m/s)	(cm)	(cm)	(%)	(cm)	(cm)	(%)	(%)
Cinnamon	V6	75	6.006	5.978		0.593	0.610		98.07
CTH	V6	75	6.000	5.985	0.12	0.600	0.608	0.33	97.50
UDRI	V6	75	6.000	5.970	0.13	0.600	0.612	0.66	91.67

This table displays some interesting similarities between this work's and UDRI's Johnson-Cook coefficients. For both change in length and nose diameter deformation, UDRI results correctly approximated the tests conducted by Cinnamon. At such small percent differences between this work and UDRI, neither work can be considered more accurate. However, the undeformed length results do promote the fact that the work of this thesis was able to more closely approximate the test conducted by Cinnamon. Since a complete analysis of UDRI's determination of the Johnson-Cook coefficients for VascoMax 300 is unknown, this work is unable to explain how UDRI was able to fit the uncorrected data with the Johnson-Cook model. As stated before, the Johnson-Cook model is not capable of explaining negative slopes in stress-strain curves, as seen for VascoMax 300. UDRI used 0.06 strain to define both the strain rate sensitivity and thermal softening coefficient, where this work used 0.07 strain. This might explain the fact that this work produced better undeformed results than UDRI. In addition, these Taylor tests were conducted at low velocities, leading to lower strain rates than would be experienced at higher velocities. With this stated, if the VascoMax 300 tests could be conducted at higher velocities, the UDRI values might lose their ability to define the deformation as their strain rate dependent coefficients lose their effectiveness.

4.4 Comparison of 1080 and VascoMax 300 to Iron and VascoMax 250

As stated earlier in this work, past analysis of the Taylor test conducted by Rickerd [1] utilized Iron to represent 1080 steel and VascoMax 250 to approximate VascoMax 300. This was due to an incomplete Johnson-Cook model for 1080 and VascoMax 300 model in CTH. Hence, the reason and basis for this work. Interesting and useful results were obtained through a comparison of these metals. From a similar code used for 1080 steel, test S8 and S9 were modeled to simulate an impact of Iron onto a VascoMax 300 rigid wall. The Johnson-Cook model for Iron already existed in the CTH viscoplastic data file. Table 16 displays the coefficients for Iron.

Table 16 - Iron Johnson-Cook Coefficients

Johnson-Cook Constants for Iron in CTH	
Constant	Value
A	1.7526×10^9 (GPa)
B	3.8019×10^9 (GPa)
C	0.06
m	0.55
n	0.32
T _m	1835.7

From these coefficients, velocities, and impact duration of 63 μ sec observed in test S8 and S9, the following deformation results were obtained from CTH.

Table 17 - Iron vs. 1080 Taylor Tests

Test Type		From Film	Cylinder Length			Nose Diameter			Undeformed Length
	Test #	V_{impact} (m/s)	L_{init} (cm)	L_{final} (cm)	(%)	D_{init} (cm)	D_{final} (cm)	(%)	(%)
Cinnamon	S9	145	5.995	5.719		0.589	0.660		70.49
	S8	123	5.991	5.774		0.600	0.652		66.70
1080	S9	145	6.000	5.620	1.73	0.600	0.640	3.03	58.33
	S8	123	6.000	5.740	0.59	0.600	0.630	3.37	66.67
Iron	S9	145	6.000	5.210	8.90	0.600	0.712	7.88	58.33
	S8	123	6.000	5.400	6.48	0.600	0.688	5.52	54.17

From Table 17, the constitutive model of 1080 better approximates the deformation seen in the Taylor tests for 1080 than the Iron model provides. The change in length for the 1080 model is more than 6 times better than that of the values Iron model. This is true with the undeformed length where the Iron model is off by as much as 18%. The nose diameter deformation produced by the 1080 model is 2 times better than the Iron model. Given the large differences seen from the undeformed length and change in length values compared to Cinnamon's results, Iron proves to be less effective than the 1080 model and hence can be omitted from further analysis of the gouging study.

A similar comparison between the effectiveness of constitutive models of VascoMax 300 versus VascoMax 250 in their ability define the deformation seen in Cinnamon's tests was conducted. Using the same CTH code for VascoMax 300, as mentioned before, the VascoMax 250 constitutive model in CTH was run with same velocities and duration of impact time that were used in the VascoMax 300 tests. Table 18 gives the Steinberg-Guinan-Lund model in CTH for VascoMax 250.

Table 18 - VascoMax 250 Constitutive Model in CTH

Steinberg-Guinan-Lund Constants for VascoMax 250 in CTH	
Constant	Value
A	2.06×10^{-12}
B	3.15×10^{-4}
ρ_o	8.129
G_o	7.18×10^{11}
Y_o	1.447×10^{10}
Y_{max}	2.5×10^{10}
$T_{m,o}$	2310
n	0.5
a	1.2
β	2
γ_o	1.67

Tests V6 and V7 were run with a VascoMax 250 rod striking VascoMax 300 rigid wall.

The results of these tests are compared with earlier results in Table 19.

Table 19 - VascoMax 250 vs. VascoMax 300 Taylor Tests

Test Type		From Film	Cylinder Length			Nose Diameter			Undeformed Length
	Test #	V_{impact} (m/s)	L_{init} (cm)	L_{final} (cm)	(%)	D_{init} (cm)	D_{final} (cm)	(%)	(%)
Cinnamon	V6	75	6.006	5.978		0.593	0.610		98.07
	V7	90	6.004	5.952		0.601	0.625		96.77
VM 300	V6	75	6.000	5.985	0.12	0.600	0.608	0.33	97.50
	V7	90	6.000	5.970	0.30	0.600	0.612	2.08	95.83
VM 250	V6	75	6.000	5.930	0.80	0.600	0.618	1.31	96.67
	V7	90	6.000	5.900	0.87	0.600	0.626	0.16	87.50

From initial comparison of the results produced by both VascoMax models only small differences exists between the deformations predicted by each one. Looking at change in length results, this work's VascoMax 300 model approximated the deformation seen in the Taylor tests better than the results produced by the VascoMax 250 model. However, VascoMax 250 CTH runs more closely resembled the nose deformation measured by

Cinnamon. In comparing the undeformed lengths of each model, VascoMax 250 approximated test V6 with the same percent difference as VascoMax 300 predicted. In test V7, though, VascoMax 250 was off by almost 10 % compared to 1% for VascoMax 300. From these results, this work suspects that the greater amount of heat treatment done on VascoMax 300 directly effects the vertical deformation seen in the tests done by Cinnamon. Even though greater accuracy is achieved by VascoMax 250 CTH model in determining the nose deformation, the difference between the two models is small. This is not true when the undeformed length is observed for test V7 and VascoMax 250 fails to approximate the length as well as VascoMax 300 model predicts. These facts allow this work to state that the VascoMax 300 model provides a better basis to understand the material behavior of the shoe at HHSTT than VascoMax 250.

It should be noted here that all tests, 1080 steel, VascoMac 300 and 250, and Iron displayed relatively high plastic strain rates during the initial contact frames and then dissipated rapidly. Also, low temperatures were observed during impact, corresponding to the relatively low velocities preformed by Cinnamon [17]. Test S8 for 1080 steel and test V7 for VascoMax 300 strain rate and temperature plots are shown below for the initial impact.

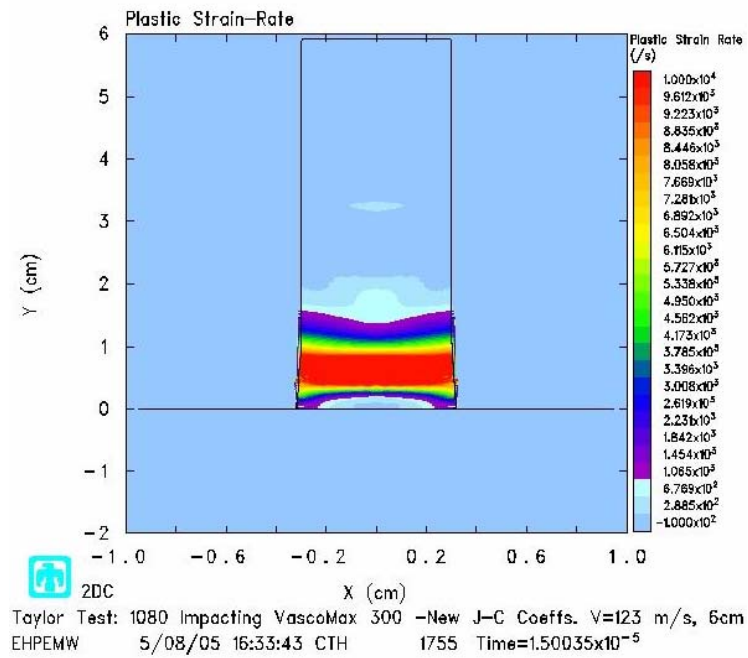


Figure 73 – 1080 Strain Rate for test S8

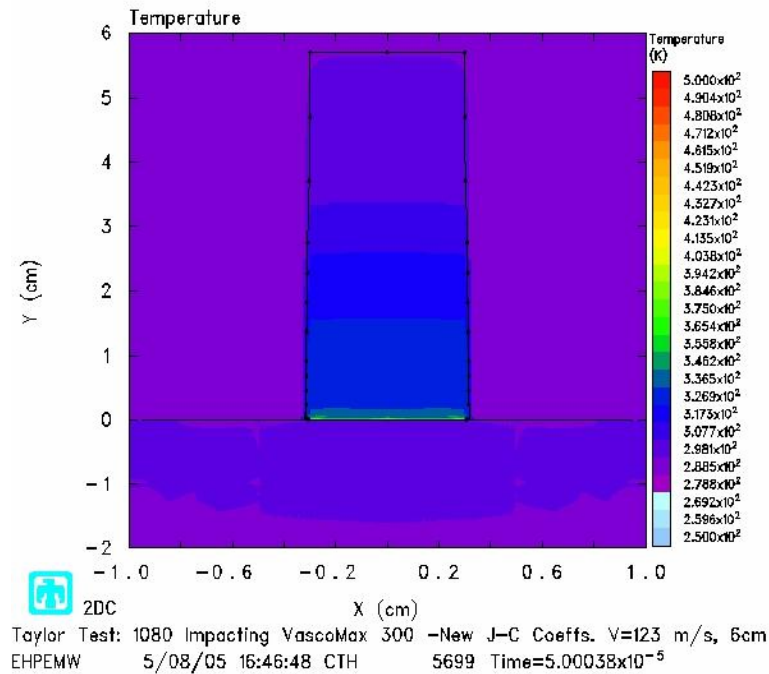


Figure 74 - 1080 Temperature for test S8

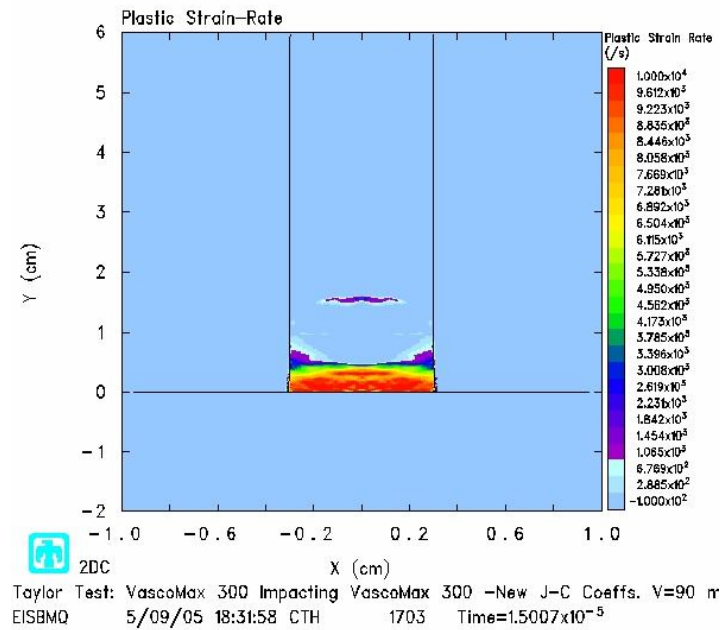


Figure 75 – VascoMax 300 Strain Rate for test S8

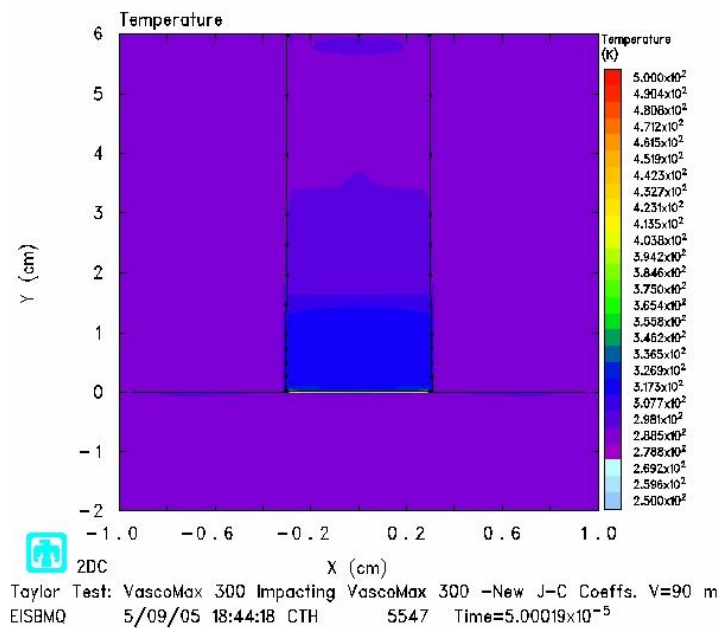


Figure 76 - VascoMax 300 Temperature for test S8

These plots represent the highest values obtained. We see that both the 1080 and VascoMax 300 experience the highest levels of plastic strain rate around 5 μsec into the impact. Also both steels reach their highest temperature around 40 μsec after impact. From the strain rates plots we see that 1080 steel and VascoMax 300 experience high local strain rates on the order of 1000/s. Temperatures for 1080 steel and VascoMax 300 never exceed 300° F . These facts will be discussed later in chapter 5.

Chapter 5 – Conclusions and Recommendations

5.1 Conclusions

The objective of this work was to provide an understanding of the material behaviors for two steel used at the Holloman High Speed Test Track. Specifically, the plastic deformation of 1080 steel and VascoMax 300 had to be quantifiably explained by a constitutive model through the fitting of various stress-strain relationships at various strain rates and temperatures. To test the models developed for 1080 steel and VascoMax 300, the Taylor test was used to verify the coefficients of the constitutive models through real world tests and computer modeling. This examination of the material behavior of both 1080 steel and VascoMax 300 utilized two experiments.

The first experiment used allowed the development of the Johnson-Cook constitutive model for both steels. The Split Hopkinson Bar test is a simple, yet effective method to understand the plastic deformation of materials at varying strain rates and temperatures. Over the past couple of decades, this test has yield excellent results for most metals, permitting strain rates from 100/s to $10^4 / s$ to be evaluated for the construction of a constitutive model. UDRI provided this study with stress-strain relations for both 1080 steel and VascoMax 300 at strain rates ranging from 500/s to 1500/s and temperatures from $300^{\circ} F$ to $1000^{\circ} F$. This data provided the basis for the Johnson-Cook constitutive model for 1080 steel and VascoMax 300.

The Johnson-Cook model was chosen due to its simplicity and straight forward approach to determining the coefficients that control the fit of the plastic region of a material's behavior. The model created for 1080 steel proved to provide an excellent fit for the material's behavior for quasi-static stress-strain relations, and more importantly the ESD and plastic strain values observed in the SHB tests. The coefficients produced through this work, as shown in chapter 3, were in agreement with those found by UDRI; providing a basis for the accuracy of the values.

For the determination of the Johnson-Cook model for VascoMax 300, the stress-strain relations provided by UDRI were not satisfactory in presenting the correct foundation to create a fit of the plastic behavior of the steel. Instead, a data correction method, depicted in chapter 3, was utilized to ensure the Johnson-Cook model for VascoMax 300 would represent a possible fit of the stress-strain relations. The use of a profilometer allowed this work to find the diameter change in the VascoMax 300 specimens that occurred during necking. From inspection of the 1080 specimens, negligible necking occurred and correction of the stress-strain relations was not needed. Understanding the area change in the VascoMax 300 specimens provided this work with the necessary means to correct a single stress-strain data point via the incompressible flow theory. This correction resulted in linear definition of the plastic region of the stress-strain curve for VascoMax 300, instead of the expected log curve seen for most metals. However, the Johnson-Cook constitutive model approximated the stress-strain relation of VascoMax 300 well, as seen in chapters 3 and 4.

A simple verification of the coefficients' ability to approximate the SHB experimental data they were based on was not enough to conclude this work had

explained the steel's material behavior under dynamic loading. Another experiment was needed to provide further justification of the models' effectiveness. The Taylor test was employed to confirm the accuracy of the Johnson-Cook models for both 1080 steel and VascoMax 300. Cinnamon [17] provided this work with the necessary Taylor test results to model in CTH. Using a similar CTH model developed by Rickerd [1], this study utilized two 1080 and VascoMax tests to evaluate the Johnson-Cook constitutive models for 1080 steel and VascoMax 300. Results from the CTH model of 1080 steel proved that the coefficients accurately approximated the deformation with respect to three measured parameters from Cinnamon [17]. The CTH model for almost every comparison was within 5% of Cinnamon's values. The most important fact that this work proved for the 1080 steel constitutive model was its ability to produce significantly better deformation results than the Iron model used in previous studies.

The VascoMax 300 Johnson-Cook model displayed excellent abilities to approximate the deformation results experienced by Cinnamon. All of the comparisons between the CTH model of test V6 and V7 and the values obtained from Cinnamon were within 2%. Given the corrections made to the VascoMax 300 data to ensure the Johnson-Cook model could fit the stress-strain relations, these extremely low percent differences suggest that the ultimate strength stress value obtained through the correction is fairly correct. This holds true due to the velocity limitations place on Cinnamon's tests because of fracture of the rods. Test V7 at 90 m/s represents the upper threshold of velocity attainable and thus stress produced is near the ultimate strength limit. However, it should be noted that the B and n coefficient are not completely correct due to the linear approximation made for the plastic region of the stress-strain curve for VascoMax 300.

In addition the results of UDRI coefficients in CTH advocate that more than one pairing of B and n coefficients can accurately define the deformation of the rods at low velocities. This work was effective at approximating the deformation for all three measurable parameters. The most significant discovery in verifying the abilities of this work's VascoMax 300 Johnson-Cook model was its ability to approximate the deformation seen in Cinnamon's results as well as VascoMax 250. For both velocities the VascoMax 300 model match the VascoMax 250 performance in defining the nose deformation and surpassed VascoMax 250 in its ability to approximate the change in length and undeformed length. As stated before, the greater amount of heat treatment done on VascoMax 300 and its resultant lack of strain hardening, proved problematic for VascoMax 250 in approximating the vertical components of deformation. Hence, this work provides a VascoMax 300 constitutive model that can replace VascoMax 250 model in further research efforts in understanding gouging at HHSTT.

In conclusion, this work successfully developed the Johnson-Cook constitutive models for 1080 steel and VascoMax 300. These models have shown their ability to approximate the material behavior of the two steels while undergoing dynamic loading with excellent accuracy given the desired goal of this study. It should be noted that the coefficients developed through this research are part of an empirical constitutive equation that represent a curve fit and allows other researches to develop models that approximate the stress-strain behavior seen in 1080 steel and VascoMax 300 with similar results [20]. However, this work provides a greater understanding of the materials involved in the gouging problem at HHSTT, yielding an improved basis for the development of a gouging model.

5.2 Recommendations for Future Research

Like any study in material properties, improvements in experimentation, use of different experimental methods, and refined analysis can yield new insight and better models created to understand a material's behavior. In this study, constitutive models were created to curve-fit a multitude of stress-strain relations at varying temperatures and strain rates for two steels. This model represents a best fit for this work, but could be adjusted to better suit new parameters.

From the SHB data, a constant strain rate was approximated as depicted in chapter 3. UDRI based its experimentation on this averaged strain rate and correlated certain stress-strain behavior to the three constant strain rates reviewed in this work. However, this constant strain rate is not an exact number and implies some error determining the true material behavior of 1080 steel and VascoMax 300. This leads to the potential correction to the models proposed by this work. By determining a range of strain rates for a given test, rather than a definite, constant value, the Johnson-Cook model would be modified. This modification would effect the coefficients dependent on strain rate, specifically the strain rate sensitivity parameter, C , and the thermal softening coefficient, m . By understanding the possible ranges of C and m , future studies could create 1080 steel and VascoMax 300 Johnson-Cook models that approximate high strain rates more accurately.

In addition to the proposed correction for strain rate effects above, a revised model of the Johnson-Cook model has been developed and may hold promise for this research. The revised model by Rule and Jones [16] is an attempt to more closely match

the observed material behavior of metals at high strain rates. The goal of their work was to enhance the strain rate sensitivity of the Johnson-Cook model while minimizing any changes to the original model where it had already effectively explained certain loading regimes. The revised Johnson-Cook model was shown to approximate ductile metals very well over a wide range of strain rates and assumes that each material has a maximum strain rate induced increase in yield strength which cannot be exceeded. [16]

This new model could help to explain the unusual necking behavior observed in VascoMax 300 and provide a better fit than the linear model developed in this study.

Appendix 1

QUASISTATIC DATA ON VASCOMAX 300 AND 1080 STEELS

Material	Test No.	Test Temp. (°F)	Strain Rate (s ⁻¹)	Flow Stress at $\epsilon = 0.06$ (GPa)	Mean Stress (GPa)
Vascomax	474-5	70	~1	1.99	1.955±0.035
300	474-6	70	~1	1.92	
				Flow Stress at $\epsilon = 0.08$	
1080	474-2	70	~1	1.03	1.048±0.016
Steel	474-3	70	~1	1.06	

SUMMARY OF SHB DATA ON 1080 STEEL

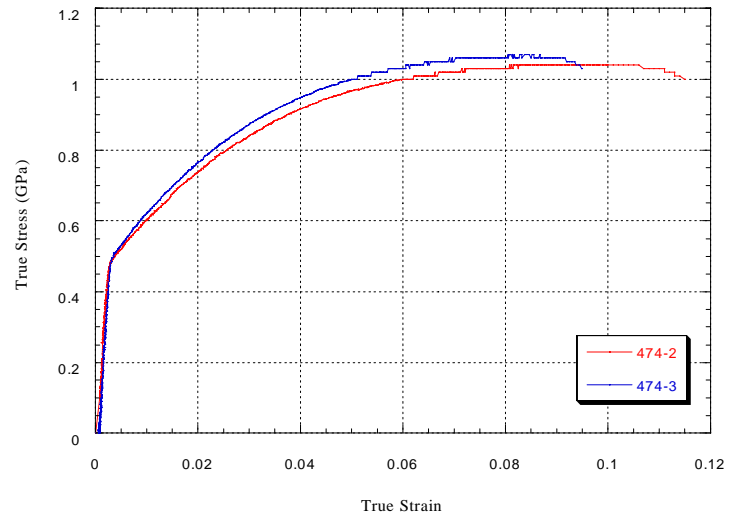
Test No.	Test Temp (°F)	Strain Rate (s ⁻¹)	Stress at $\epsilon \sim 0.08$ (GPa)	Mean Stress (GPa)
T-03	70	~500	1.22	1.24± 0.02
T-04	70	~500	1.26	
T-11	300	~500	1.09	1.10±0.015
T-12	300	~500	1.12	
T-16	500	~500	0.93	0.94± 0.015
T-17	500	~500	0.96	
T-13	300	~1000	1.07	1.05± 0.02
T-14	300	~1000	1.03	
T-23	500	~1000	0.97	0.94±0.03
T-24	500	~1000	0.91	

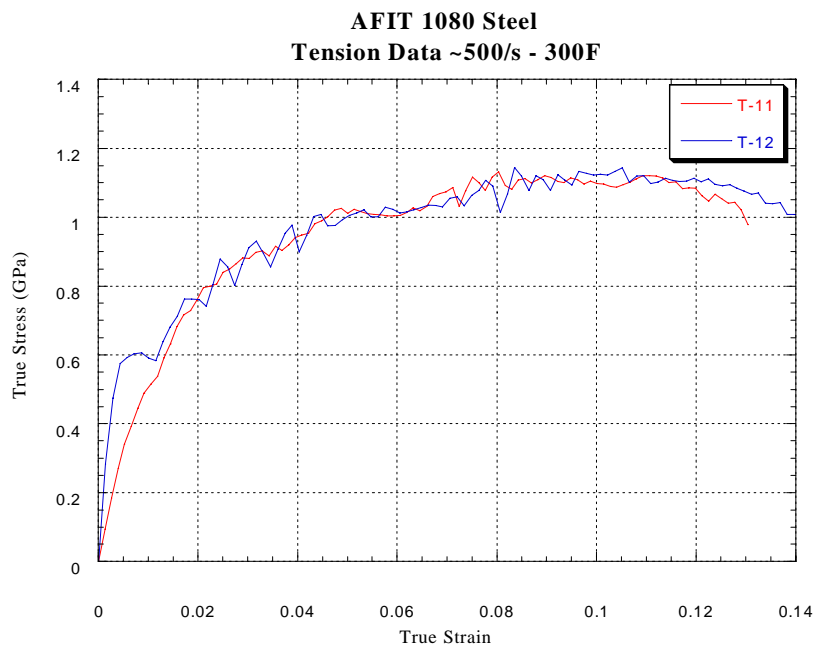
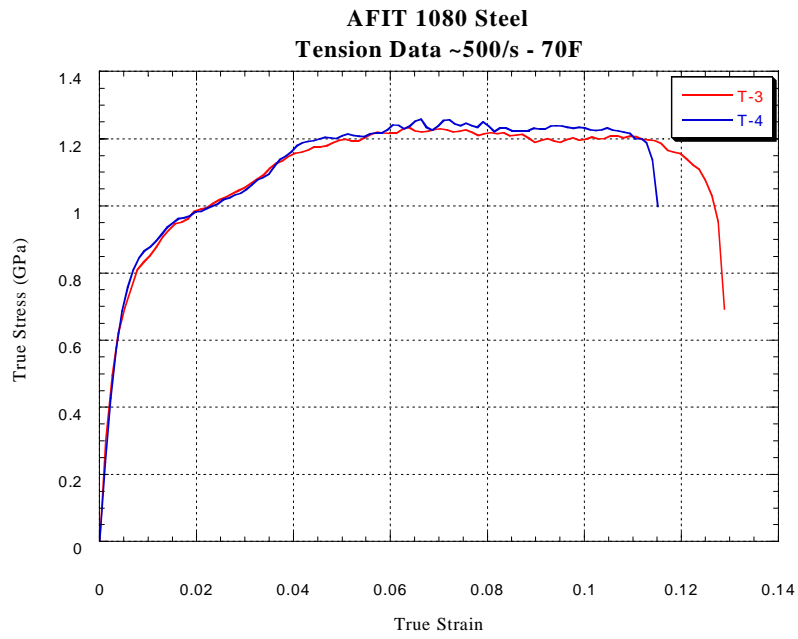
Test No.	Test Temp (°F)	Strain Rate (s ⁻¹)	Stress at $\epsilon \sim 0.08$ (GPa)	Mean Stress (GPa)
T-22	750	~1000	0.85	0.86 ± 0.01
T-31	750	~1000	0.87	
T-25	70	~1500	1.24	1.27±0.03
T-26	70	~1500	1.30	
T-33	300	~1500	1.24	1.20±0.035
T-34	300	~1500	1.17	
T-27	500	~1500	0.96	0.92±0.035
T-28	500	~1500	0.89	
T-36	750	~1500	0.92	0.94±0.02
T-38	750	~1500	0.96	

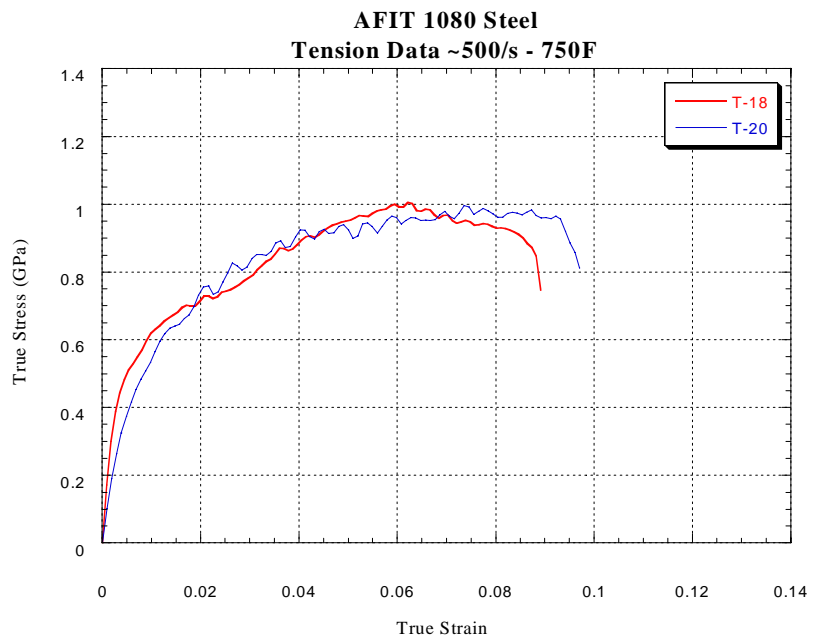
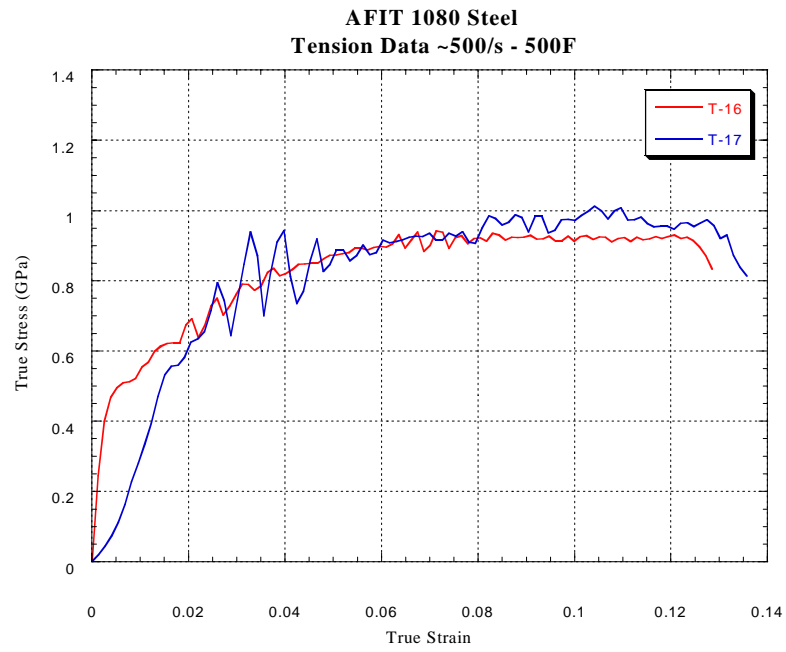
SUMMARY OF SHB DATA ON VASCOMAX 300 STEEL

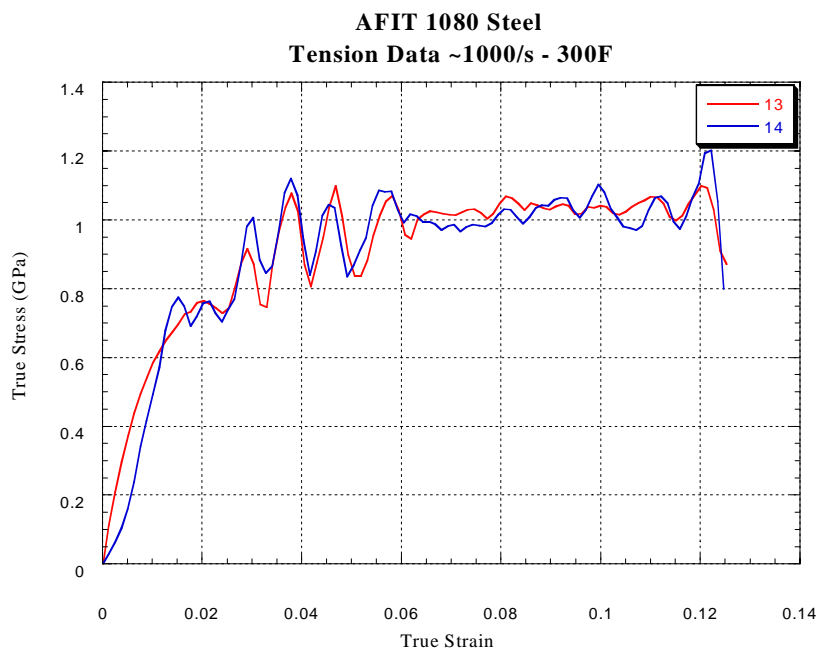
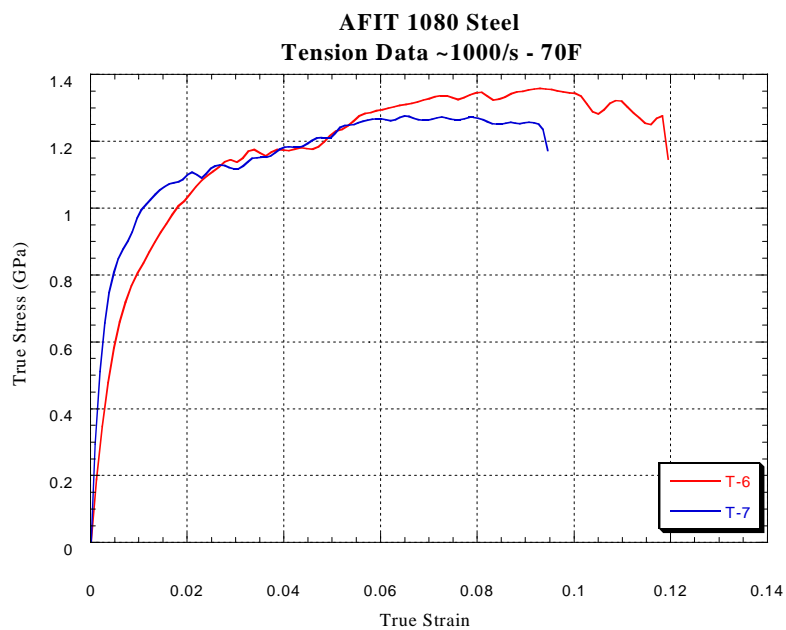
Test No.	Test Temp (°F)	Strain Rate (s ⁻¹)	Stress at $\epsilon \sim 0.06$ (GPa)	Mean Stress (GPa)
T-3	70	~500	1.88	1.92±0.04
T-4	70	~500	1.97	
T-15	500	~500	1.56	1.53±0.030
T-16	500	~500	1.50	
T-19	750	~500	1.50	1.52±0.02
T-20	750	~500	1.54	
T-17	1000	~500	1.16	1.14±0.02
T-18	1000	~500	1.12	
T-1	70	~1000	2.00	1.89±0.11
T-2	70	~1000	1.78	
T-9	500	~1000	1.74	1.77±0.03
T-28	500	~1000	1.80	
T-10	750	~1000	1.50	1.53±0.03
T-11	750	~1000	1.57	
T-12	1000	~1000	1.28	1.24±0.03
T-13	1000	~1000	1.21	
T-6	70	~1500	1.91	2.01±0.10
T-7	70	~1500	2.12	
T-21	500	~1500	1.99	1.97±0.02
T-23	500	~1500	1.95	
T-24	750	~1500	1.81	1.76±0.05
T-25	750	~1500	1.71	
T-26	1000	~1500	1.48	1.43±0.00
T-27	1000	~1500	1.39	

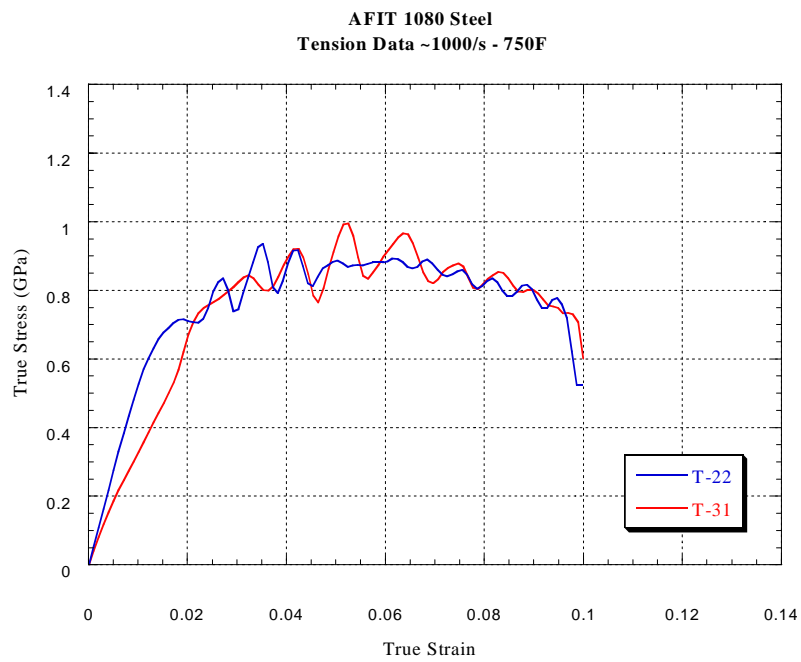
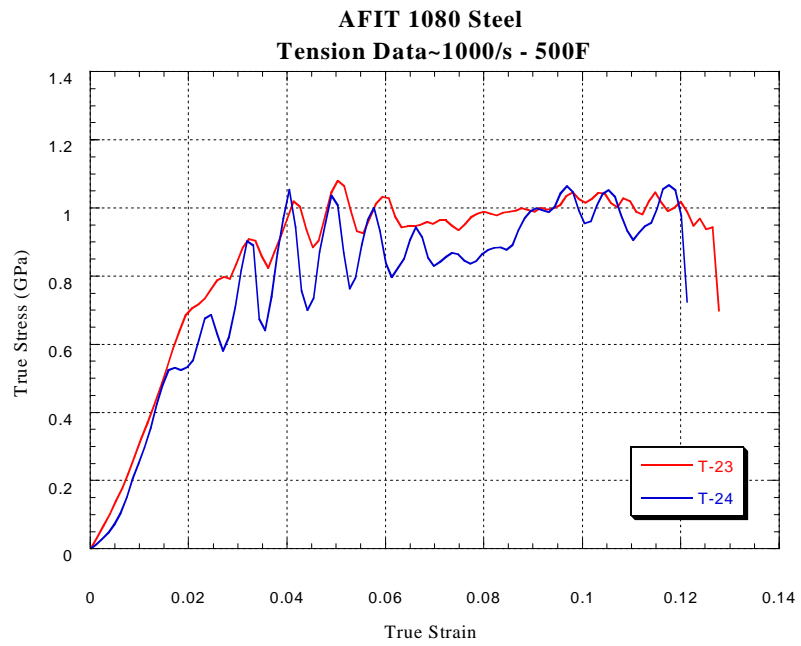
AFIT 1080 Steel
Tension Data ~1/s - 70F

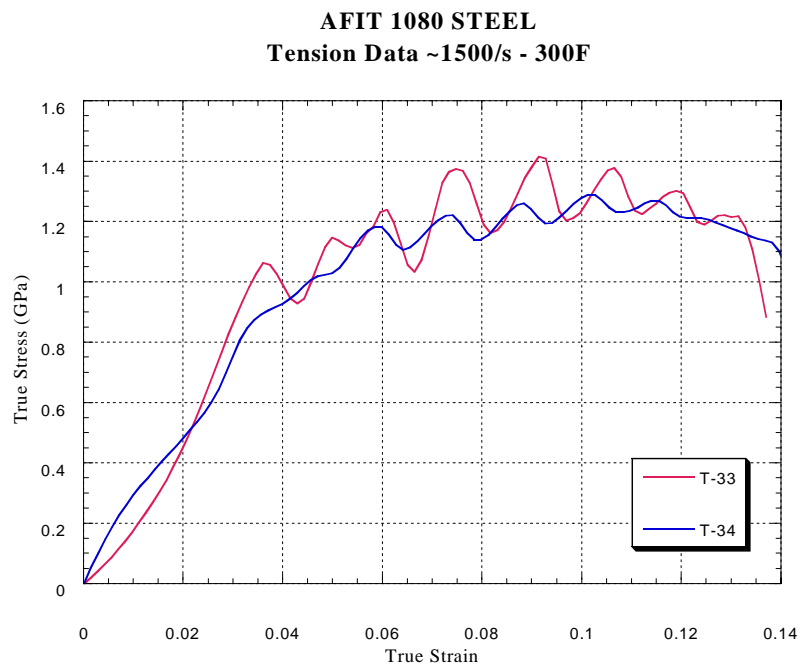
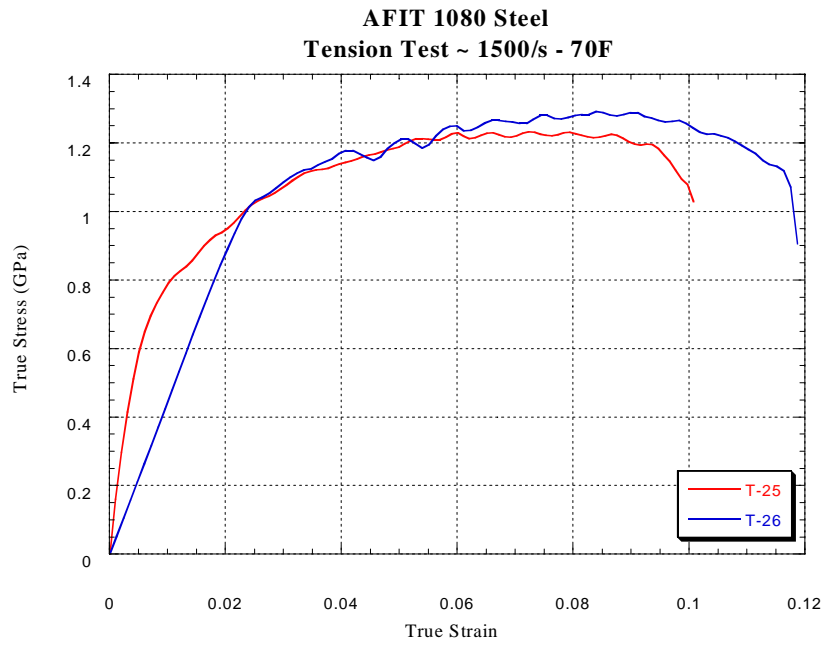


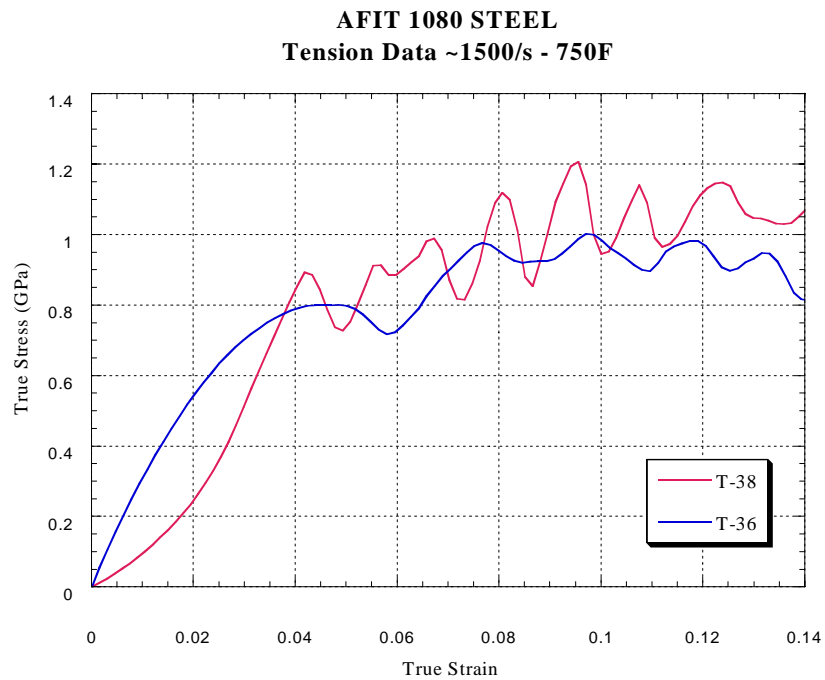
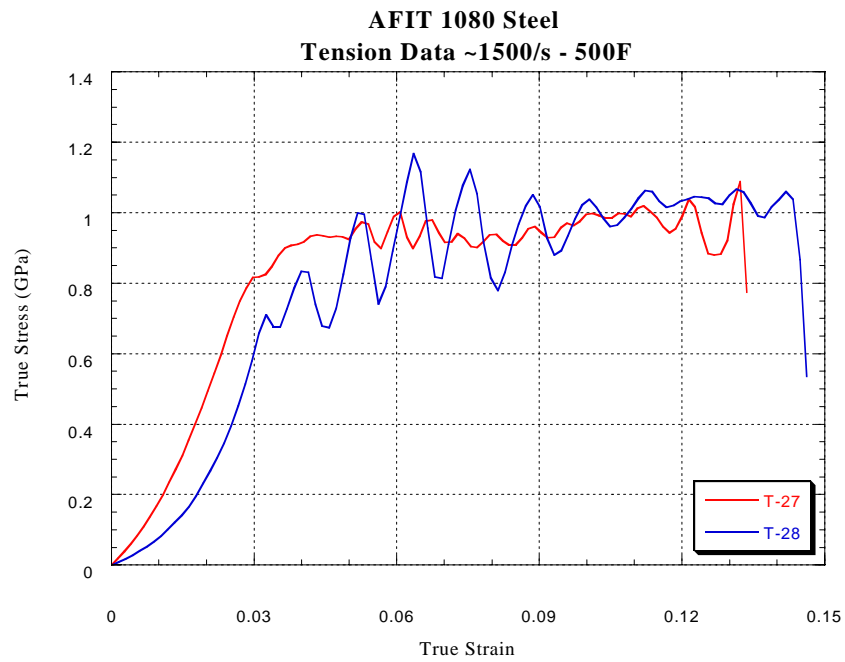




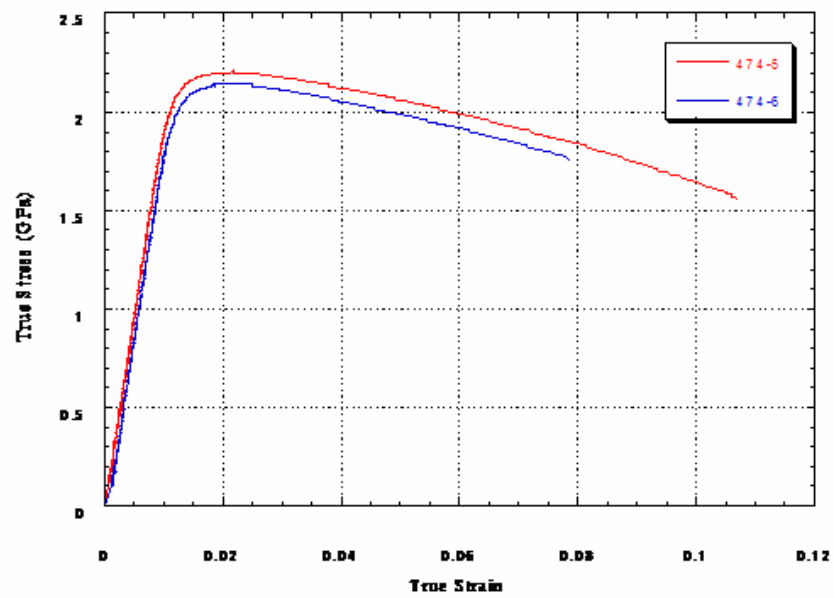


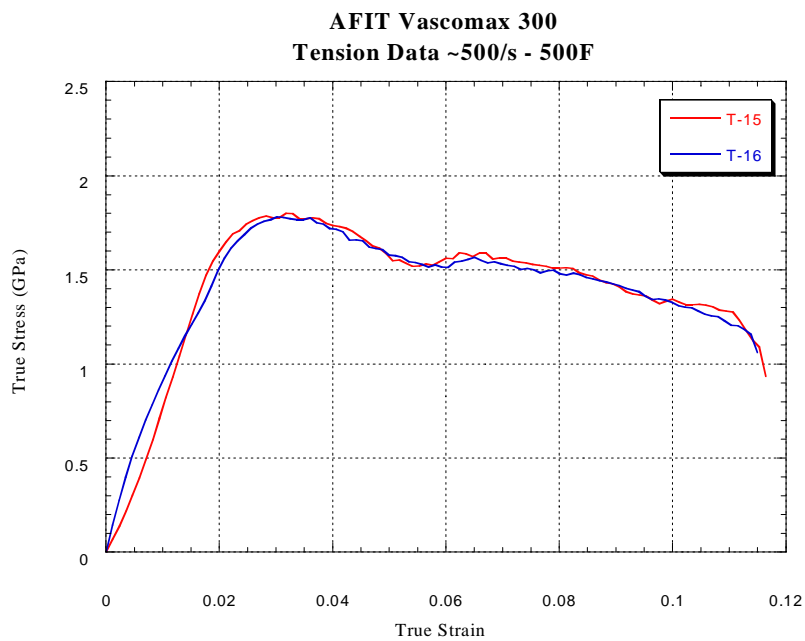
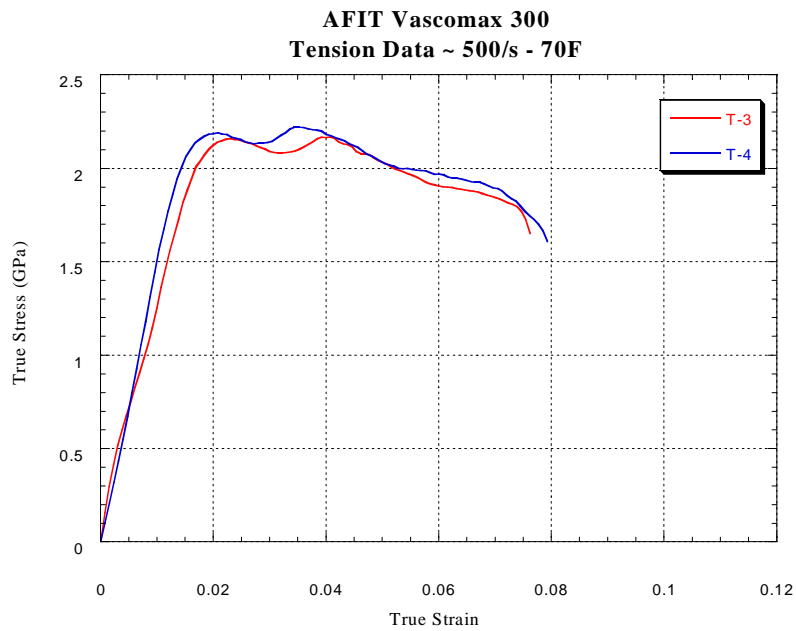


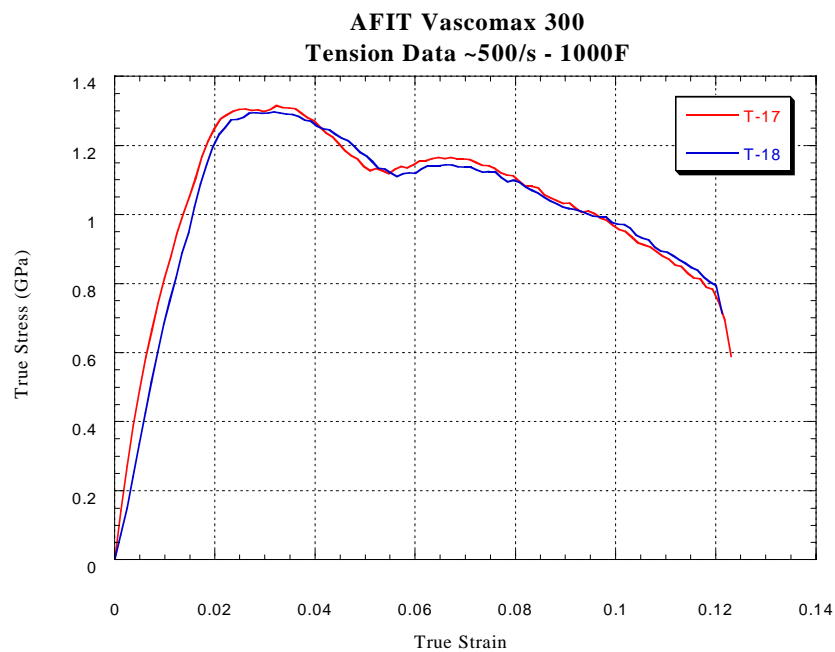
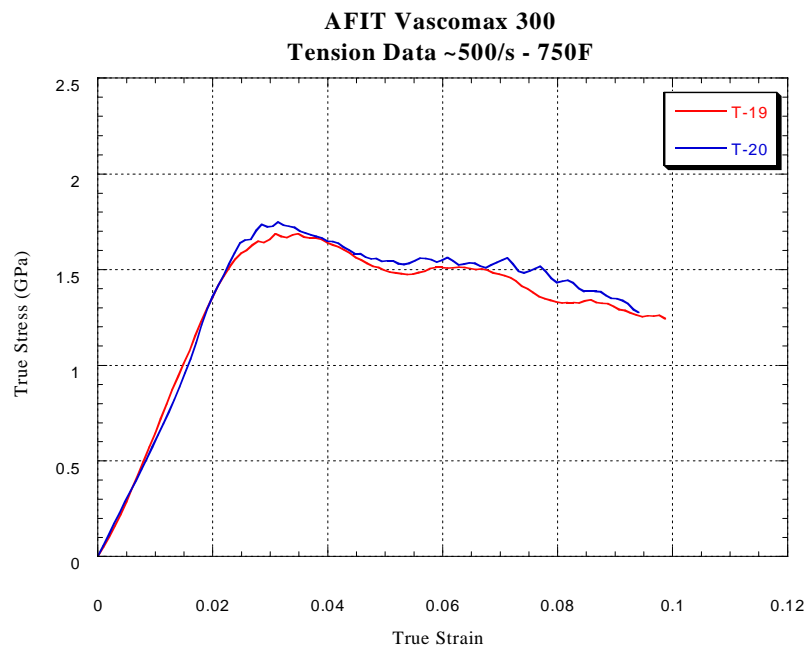


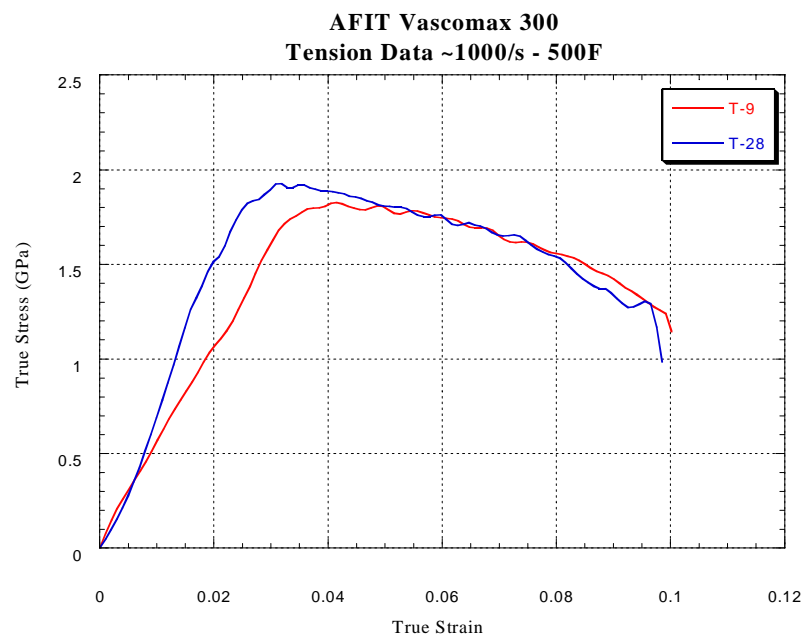
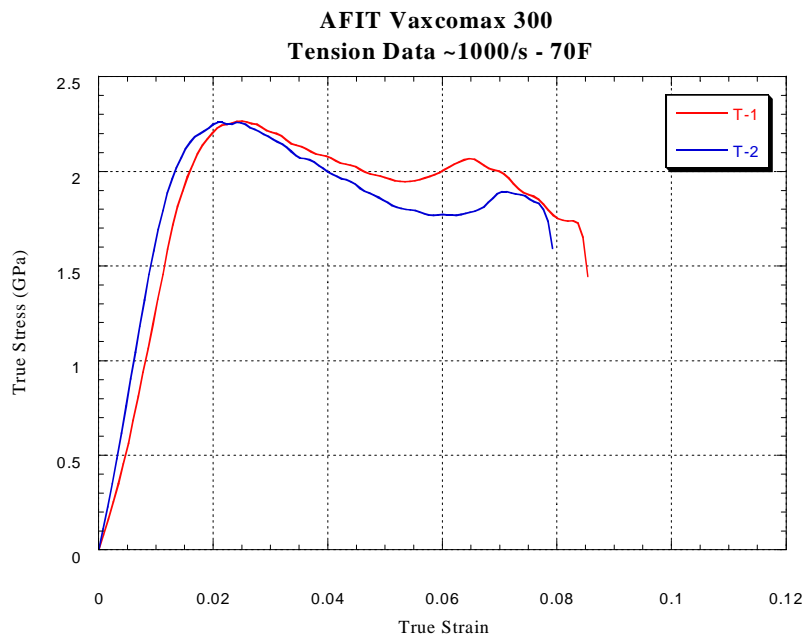


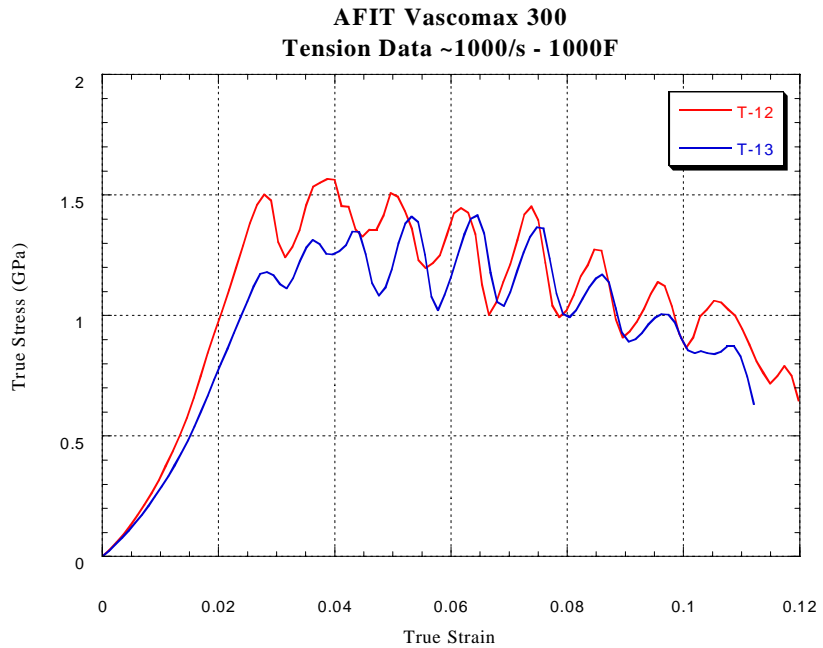
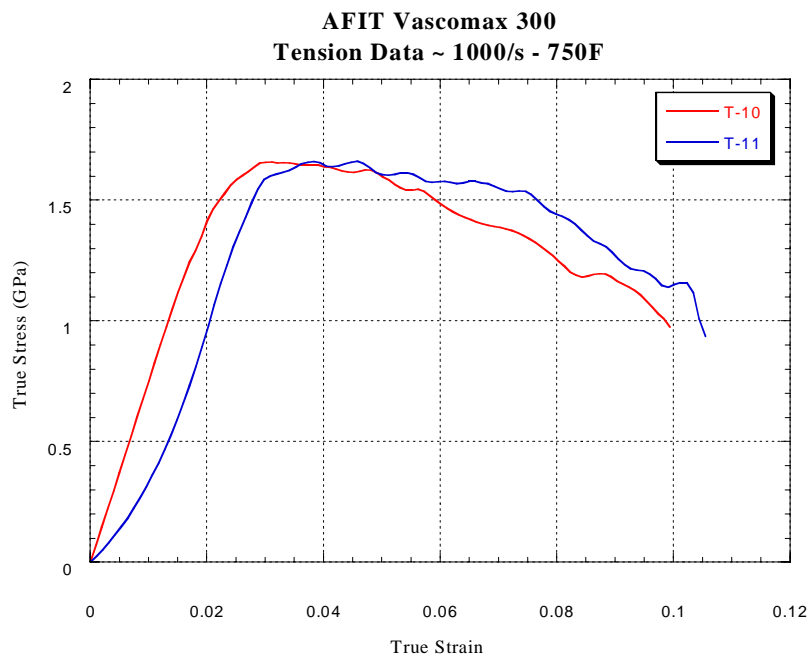
AFIT Vascomax 300
Tension Data ~ 1/s - 70F

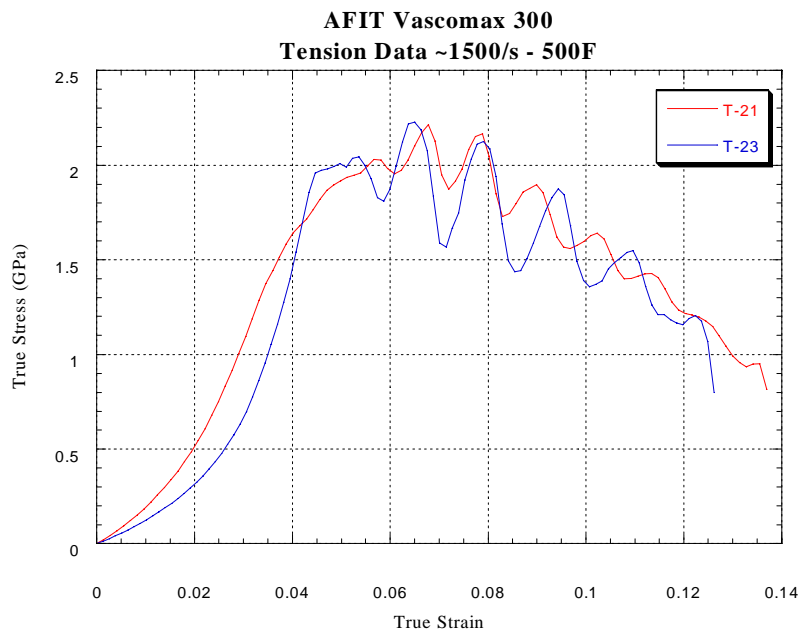
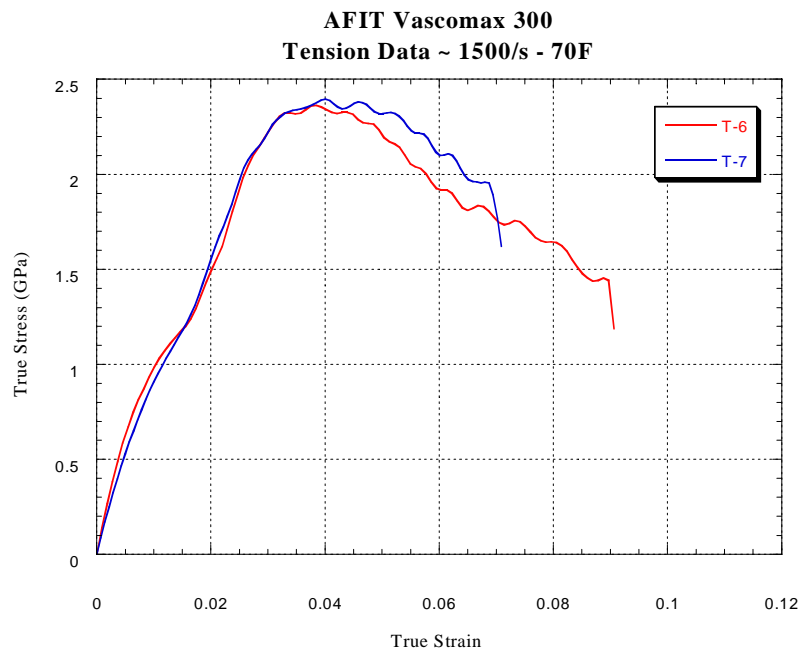


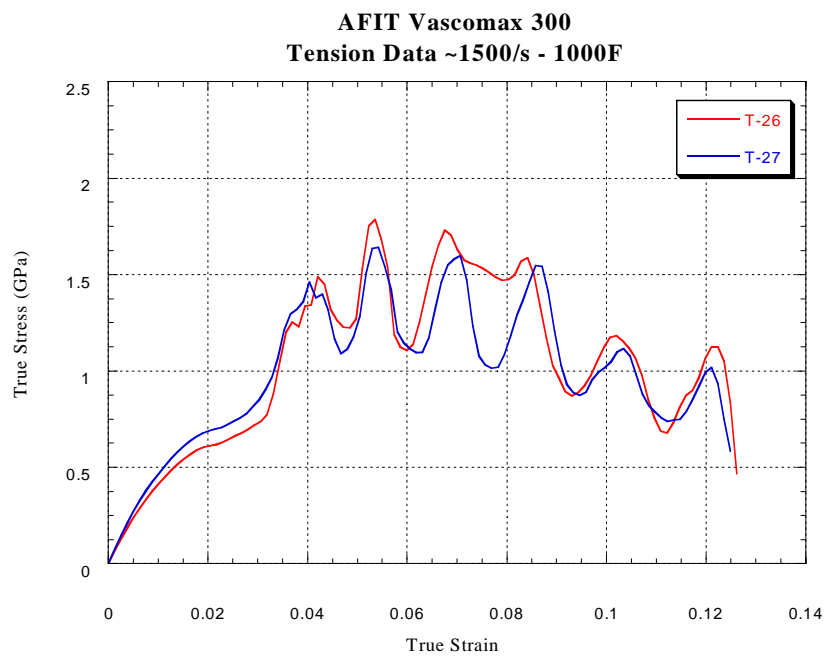
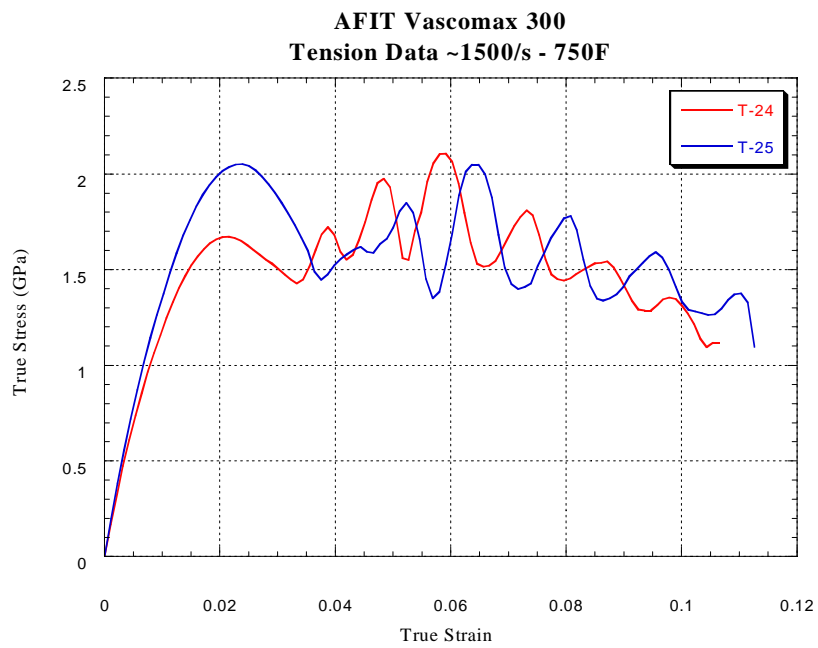












Appendix 2

1080 Steel Johnson-Cook modeling

Interpolation of Stress at 0.062 strain

Test	Strain (near .062)	Stess	Interp.	Interp. Stress
4	0.0617	1.2680	-97.9167	1.2347
	0.0621	1.2210		
3	0.0619	1.2020	108.6957	1.2107
	0.0624	1.2520		
6	0.0616	1.2940	7.3529	1.2971
	0.0623	1.2990		
7	0.0614	1.2530	-22.2222	1.2401
	0.0622	1.2350		
25	0.0614	1.1880	-21.6867	1.1759
	0.0623	1.1700		
26	0.0617	1.1690	40.9639	1.1825
	0.0625	1.2030		

Determination of C Coefficient

Strain Rate	Test Number	Stress at E=.062	Avg Stress	Dynamic/Static Stress	Ln(Strain Rate)
1	1	1.0000	1.0200	1.0000	0.0000
1	2	1.0400			
500	3	1.2107	1.2227	1.1987	6.2146
500	4	1.2347			
1000	6	1.2971	1.2686	1.2437	6.9078
1000	7	1.2401			
1500	25	1.1759	1.1792	1.1561	7.3132
1500	26	1.1825			

Determination of m Coefficient

Strain Rate 500

Dynamic Stress 1.222702

Test Number	Strain	Stress	Interpellation	Interp. Stress	Temp	Log(1-[Dyn. Stress(T) / Dyn. Stress(RT)])	T*	Log(T*)
3 and 4				1.2	70	-1.7313	0.0040	-2.3962
11	0.0619	1.0120	126.1905	1.0297	300	-0.8017	0.0964	-1.0160
	0.0623	1.0650						
12	0.0619	0.9935	1.0714	0.9936	300	-0.7273	0.0964	-1.0160
	0.0624	0.9941						
16	0.0617	0.8417	84.2308	0.8678	500	-0.5372	0.1767	-0.7527
	0.0622	0.8855						
17	0.0618	0.9043	-21.5625	0.8989	500	-0.5771	0.1767	-0.7527
	0.0624	0.8905						
18	0.0617	1.0200	106.6667	1.0520	750	-0.8551	0.2771	-0.5574
	0.0622	1.0680						
20	0.0618	0.9332	86.6667	0.9479	750	-0.6484	0.2771	-0.5574
	0.0623	0.9722						

Strain Rate 1000

Dynamic Stress 1.2685997

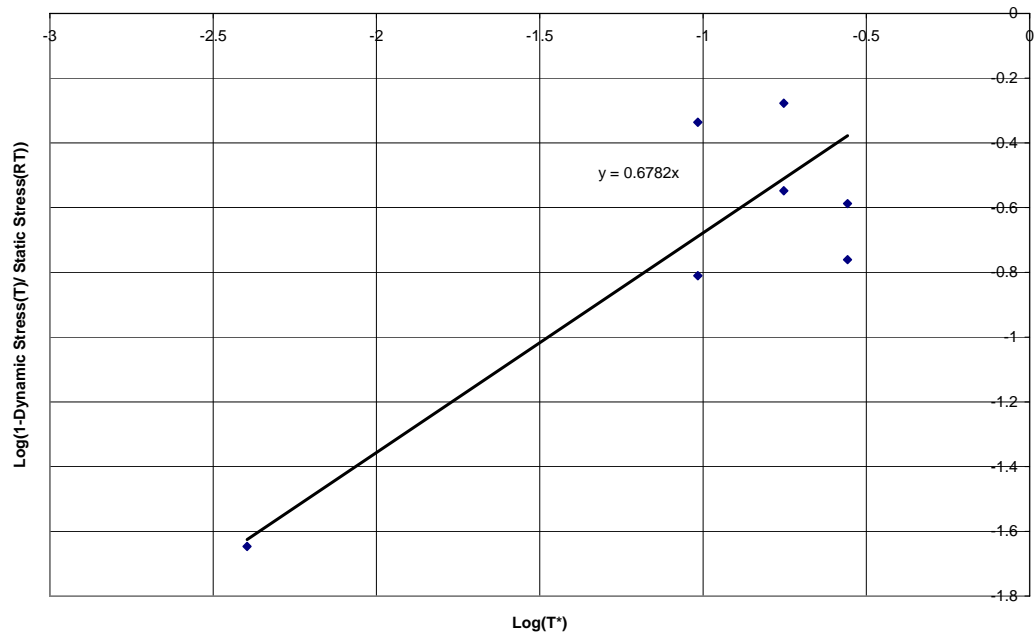
Test Number	Strain	Stress	Interpellation	Interp. Stress	Temp	Log(1- Dyn. Stress(T) / Dyn. Stress(RT))	T*	Log(T*)
6 and 7				1.24	70	-1.6470	0.0040	-2.3962
13	0.0620	0.6687	299.3671	0.6837	300	-0.3362	0.0964	-1.0160
	0.0627	0.9052						
14	0.0620	1.0730	-75.2809	1.0722	300	-0.8103	0.0964	-1.0160
	0.0629	1.0060						
23	0.0612	1.0910	-233.0000	0.9093	500	-0.5478	0.1767	-0.7527
	0.0620	0.9046						
24	0.0620	0.5966	211.9512	0.5987	500	-0.2773	0.1767	-0.7527
	0.0628	0.7704						
22	0.0616	0.9426	-4.4944	0.9406	750	-0.5875	0.2771	-0.5574
	0.0625	0.9386						
31	0.0611	0.9628	93.1579	1.0485	750	-0.7607	0.2771	-0.5574
	0.0622	1.0690						

Strain Rate 1500

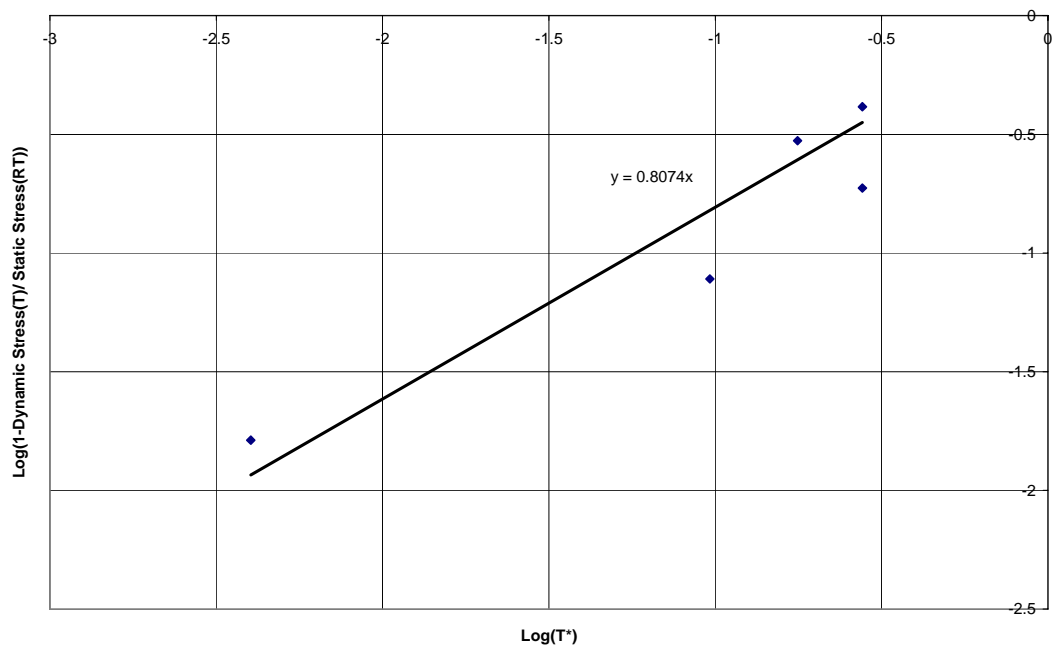
Dynamic Stress 1.1791867

Test Number	Strain	Stress	Interpellation	Interp. Stress	Temp	Log(1- Dyn. Stress(T) / Dyn. Stress(RT))	T*	Log(T*)
25 and 26				1.16	70	-1.7886	0.0040	-2.3962
33	0.0614	1.5230	-168.5535	1.4252	300	#NUM!	0.0964	-1.0160
	0.0630	1.2550						
34	0.0611	1.2130	-137.8571	1.0876	300	-1.1095	0.0964	-1.0160
	0.0625	1.0200						
27	0.0613	1.1150	-427.3494	0.8287	500	-0.5269	0.1767	-0.7527
	0.0622	0.7603						
28	0.0620	1.4160	349.6063	1.4195	500	#NUM!	0.1767	-0.7527
	0.0633	1.8600						
36	0.0610	0.6596	32.6506	0.6923	750	-0.3841	0.2771	-0.5574
	0.0627	0.7138						
38	0.0601	0.8270	66.9652	0.9576	750	-0.7260	0.2771	-0.5574
	0.0621	0.9616						

1080 M Coefficient at 1000/s



1080 M Coefficient at 1500/s

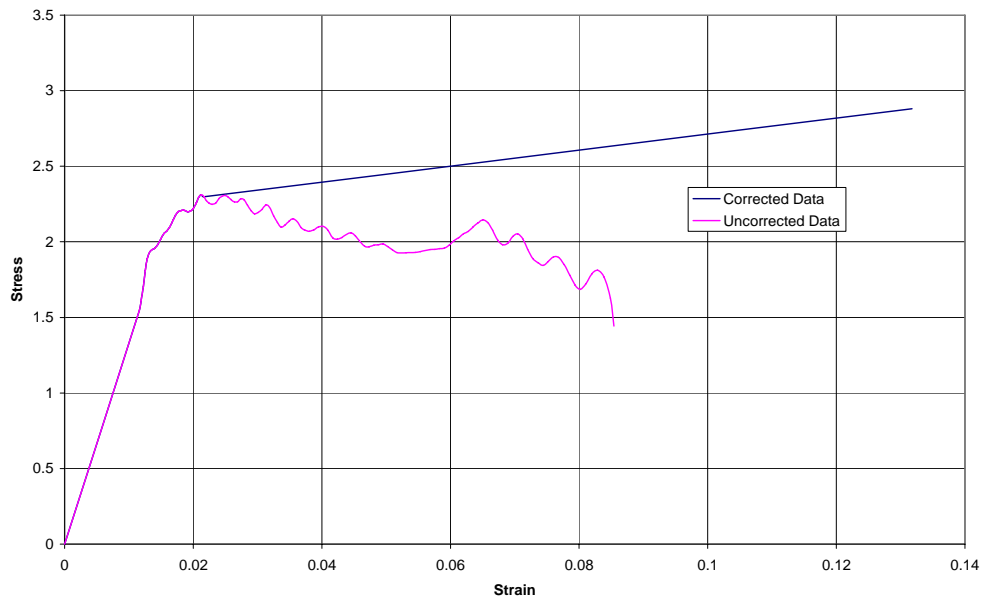


Appendix 3

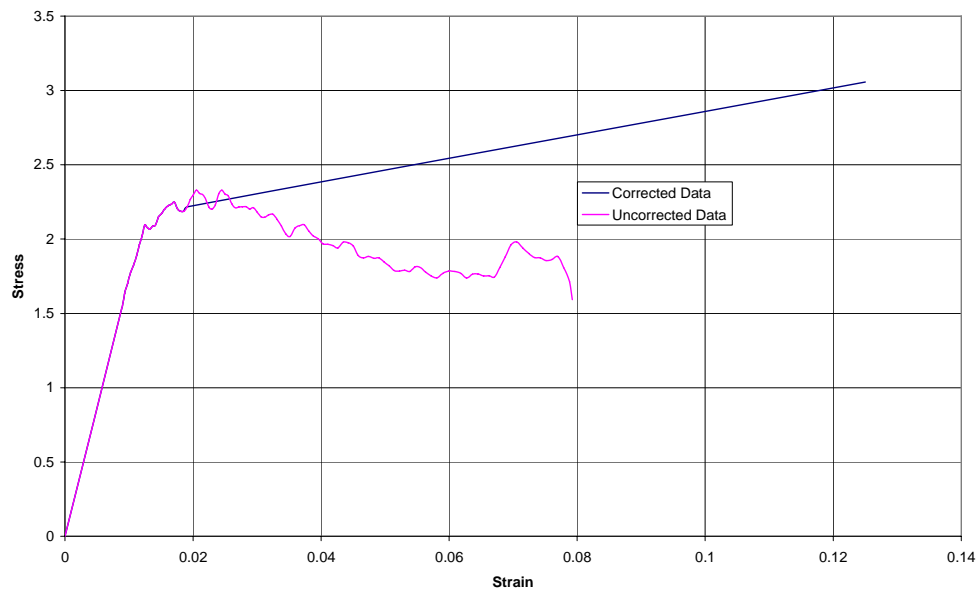
VascoMax 300 Stress-Strain Corrections

Correction of all VascoMax 300 UDRI Data

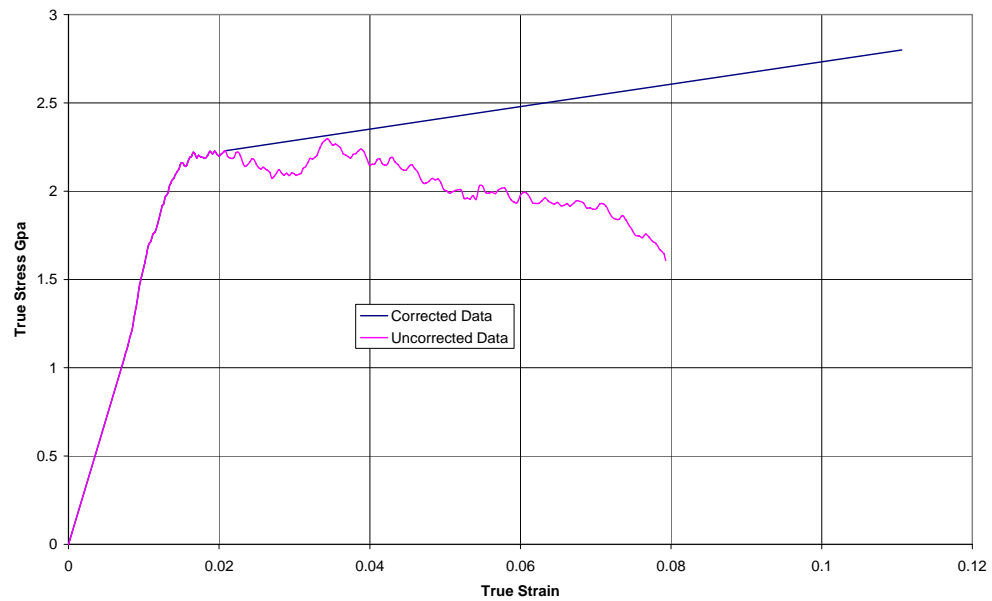
Comparison of Uncorrected and Corrected Data for VascoMax 300 Test 1



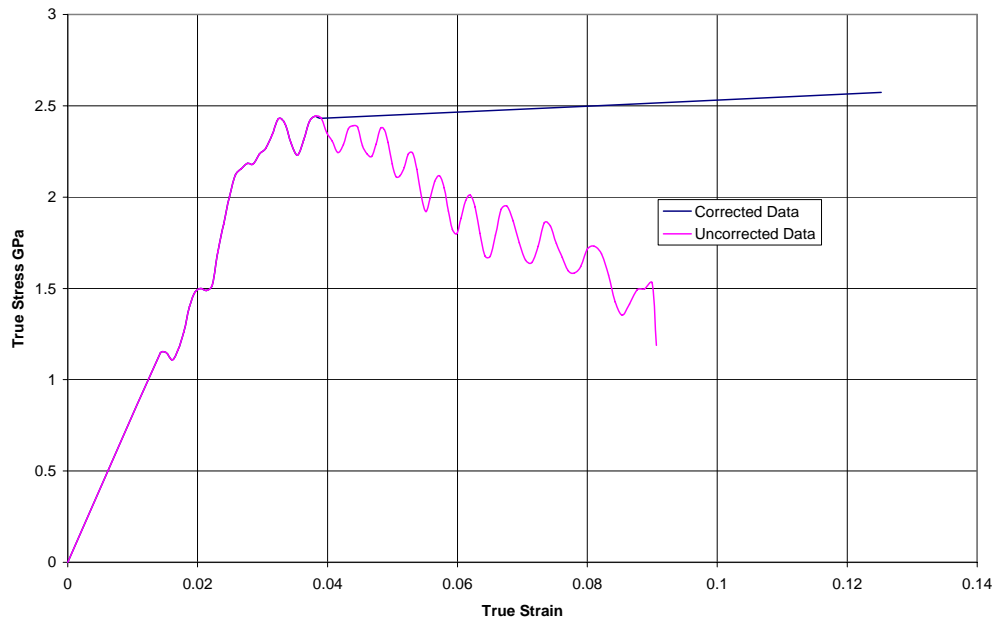
Comparison of Uncorrected and Corrected Data for VascoMax 300 Test 2



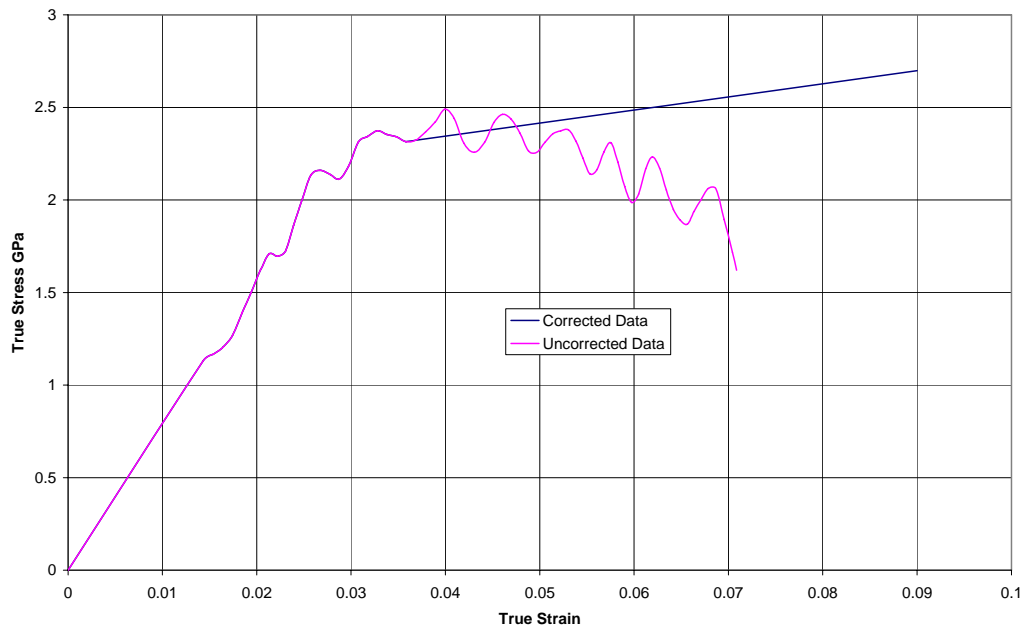
Comparison of Uncorrected and Corrected Data for VascoMax 300 Test 4



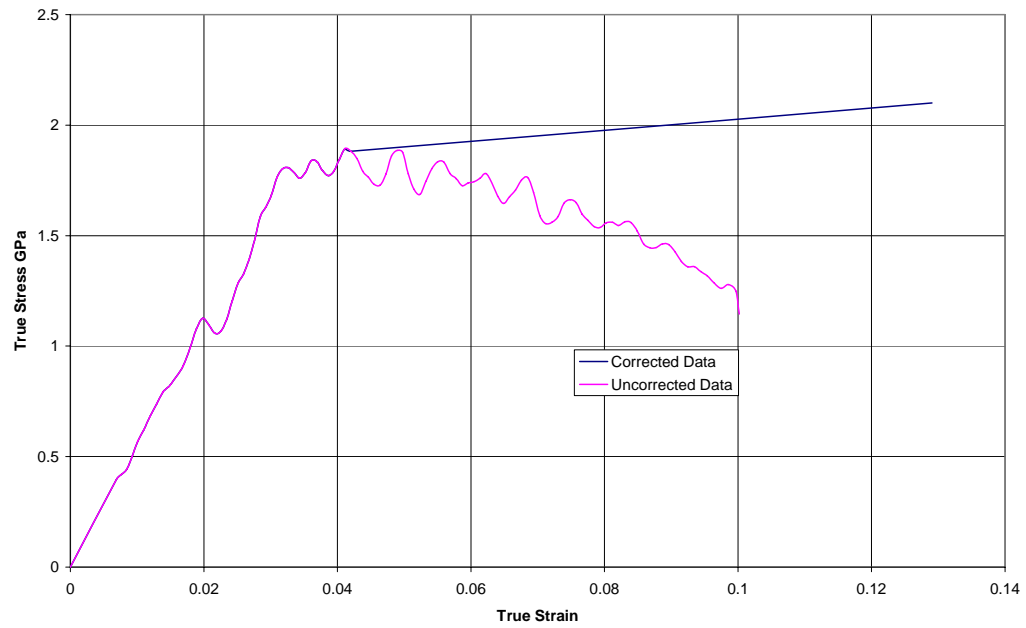
Comparison of Uncorrected and Corrected Data for VascoMax 300 Test 6



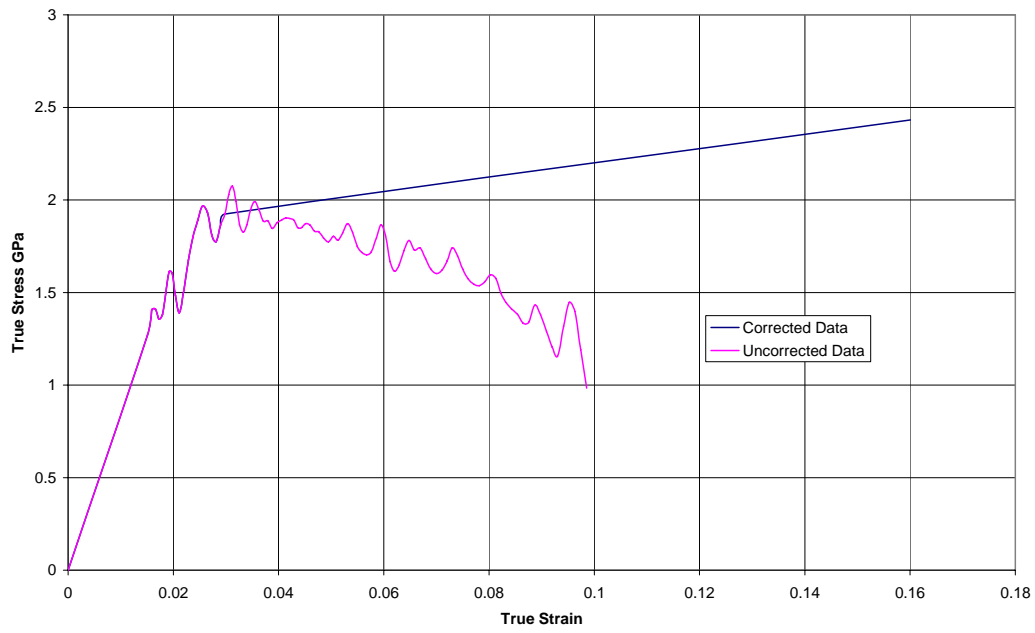
Comparison of Uncorrected and Corrected Data for VascoMax 300 Test 7



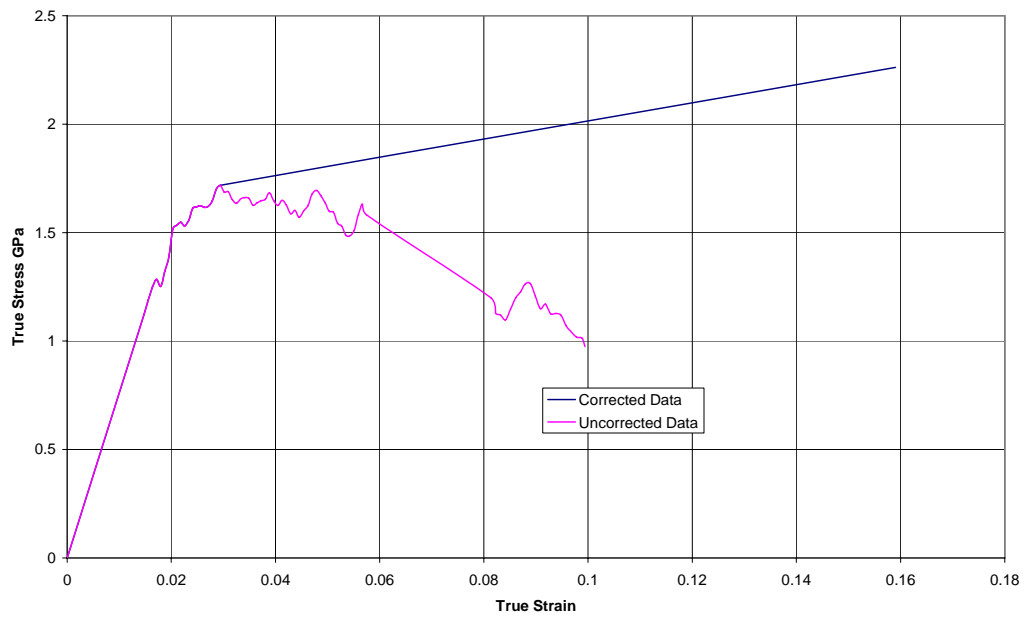
Comparison of Uncorrected and Corrected Data for VascoMax 300 Test 9



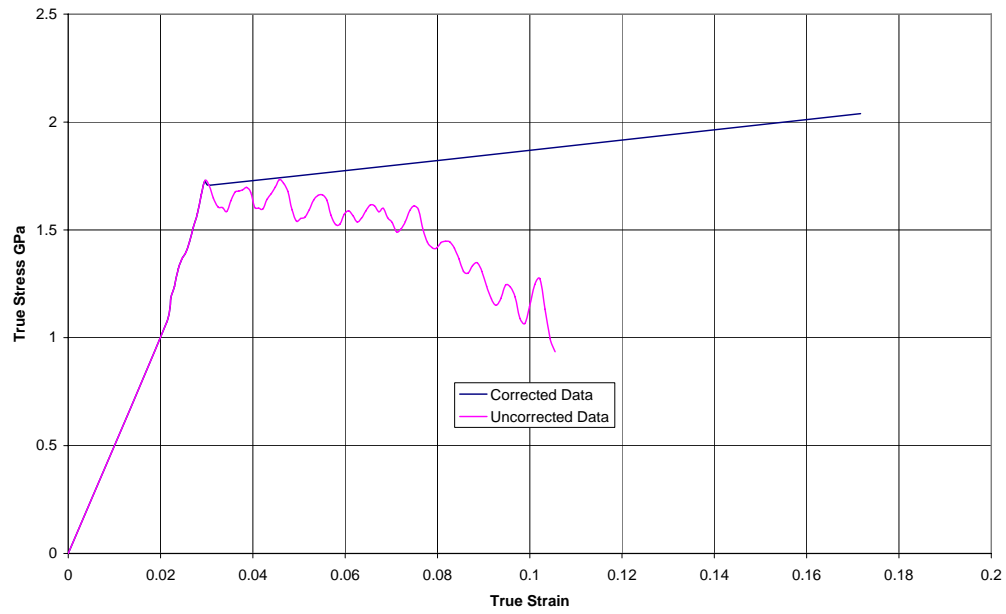
Comparison of Uncorrected and Corrected Data for VascoMax 300 Test 28



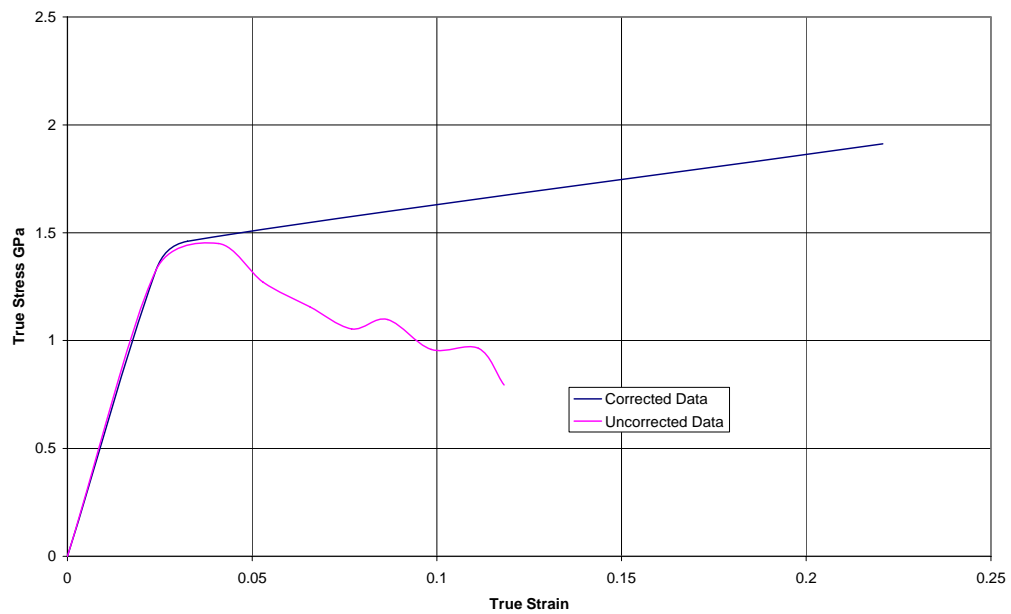
Comparison of Uncorrected and Corrected Data for VascoMax 300 Test 10



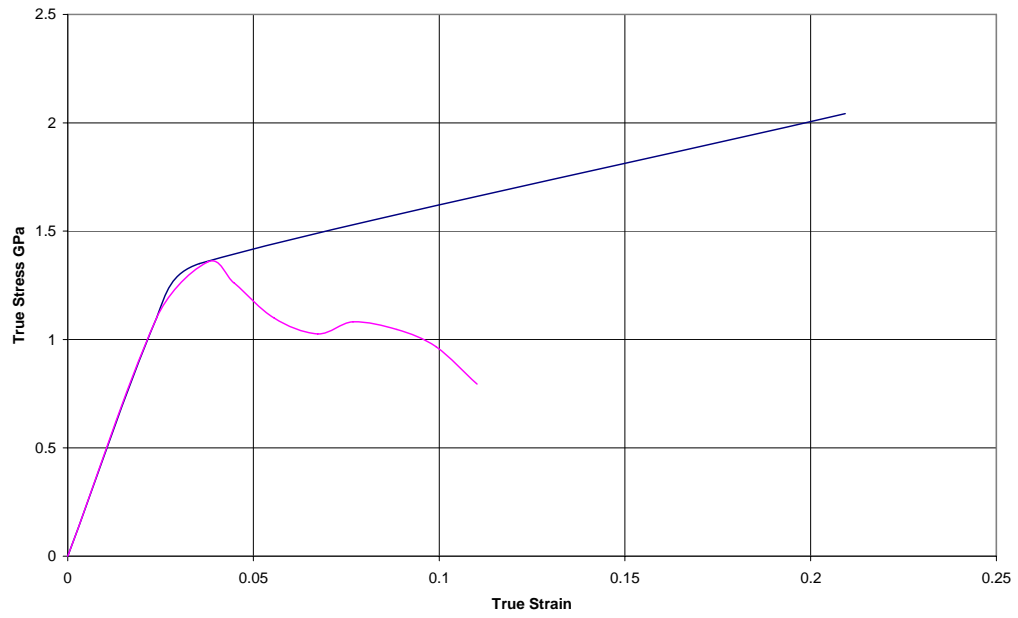
Comparison of Uncorrected and Corrected Data for VascoMax 300 Test 11



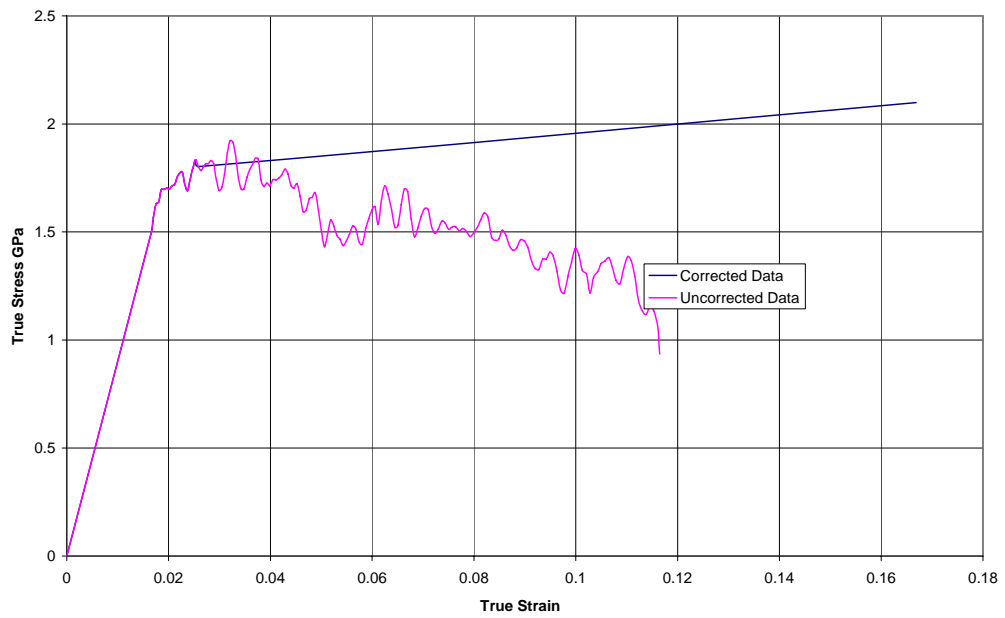
Comparison of Uncorrected and Corrected Data for VascoMax 300 Test 12



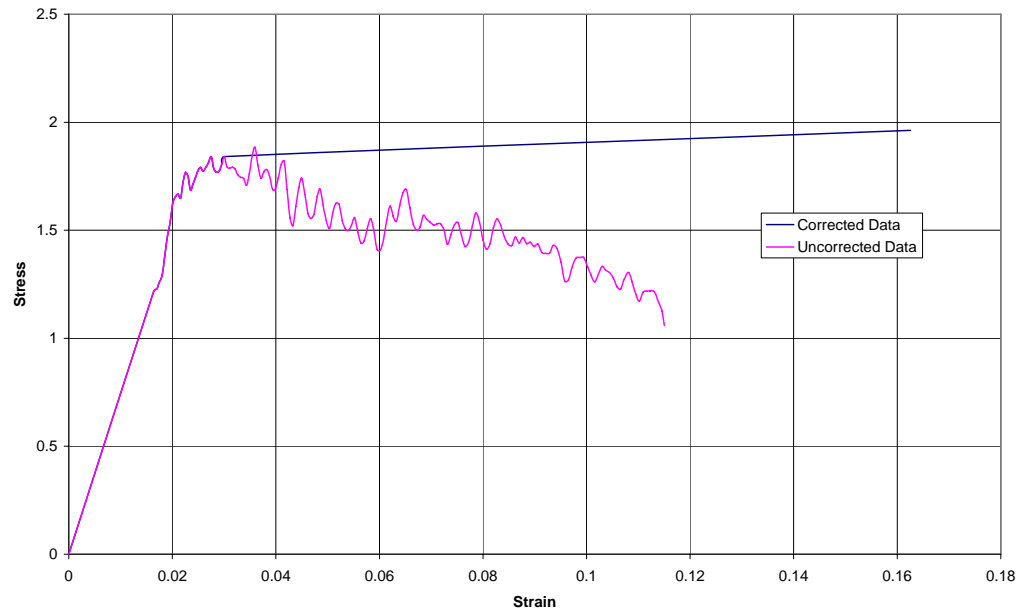
Comparison of Uncorrected and Corrected Data for VascoMax 300 Test 13



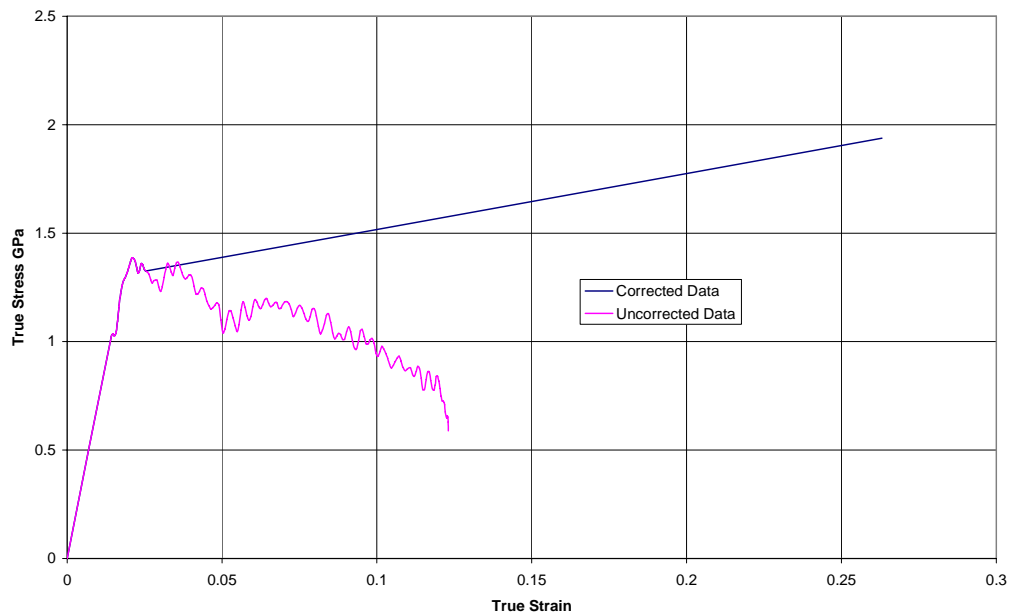
Comparison of Uncorrected and Corrected Data for VascoMax 300 Test 15



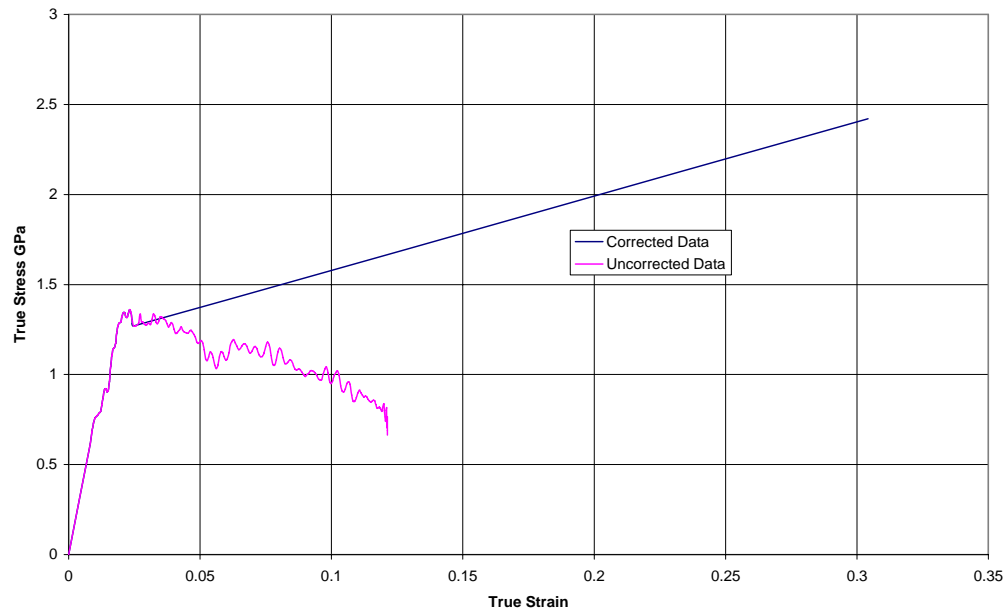
Comparison of Uncorrected and Corrected Data for VascoMax 300 Test 16



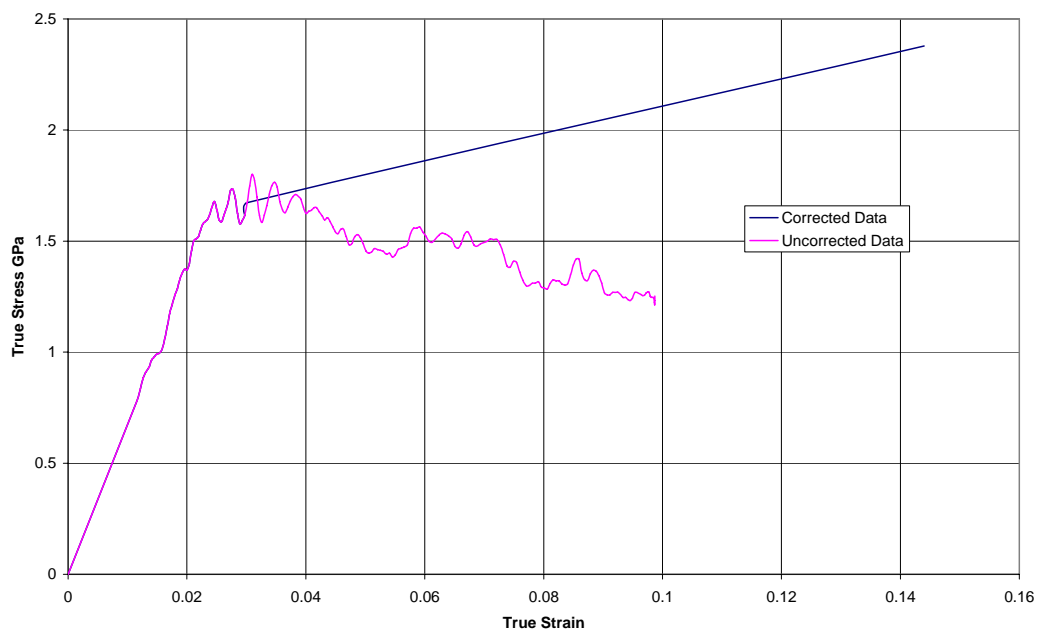
Comparison of Uncorrected and Corrected Data for VascoMax 300 Test 17



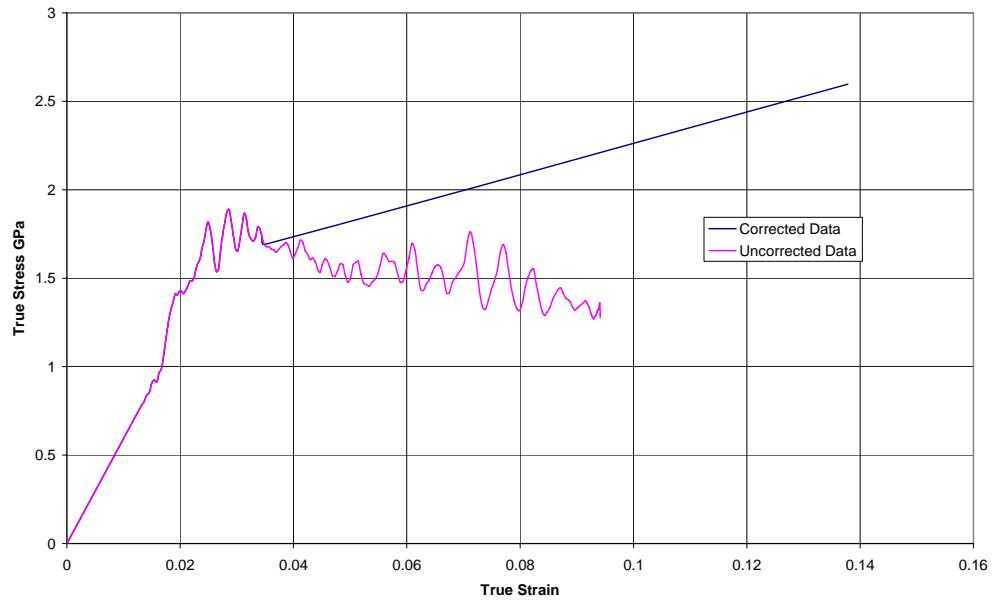
Comparison of Uncorrected and Corrected Data for VascoMax 300 Test 18



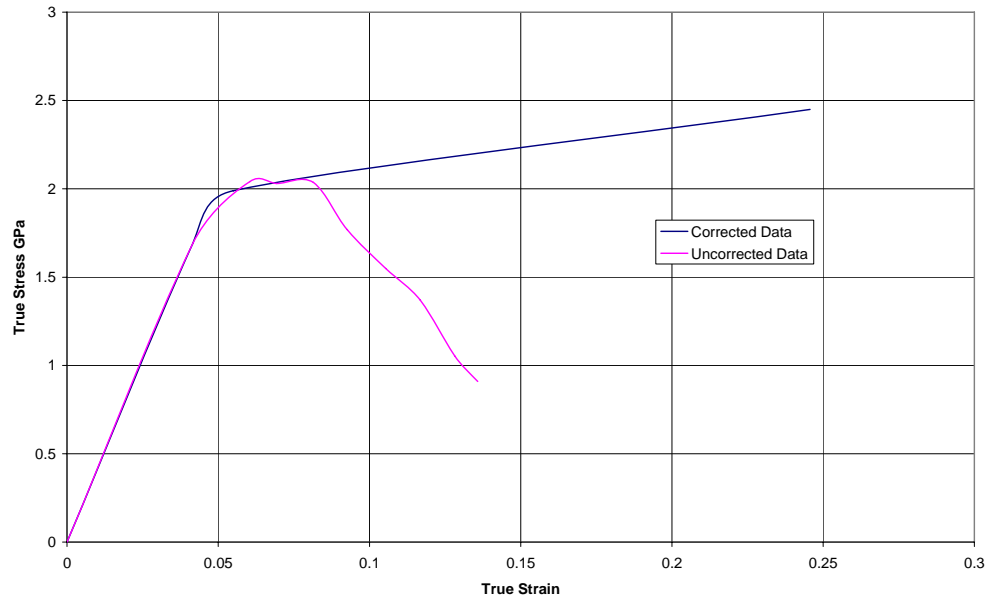
Comparison of Uncorrected and Corrected Data for VascoMax 300 Test 19



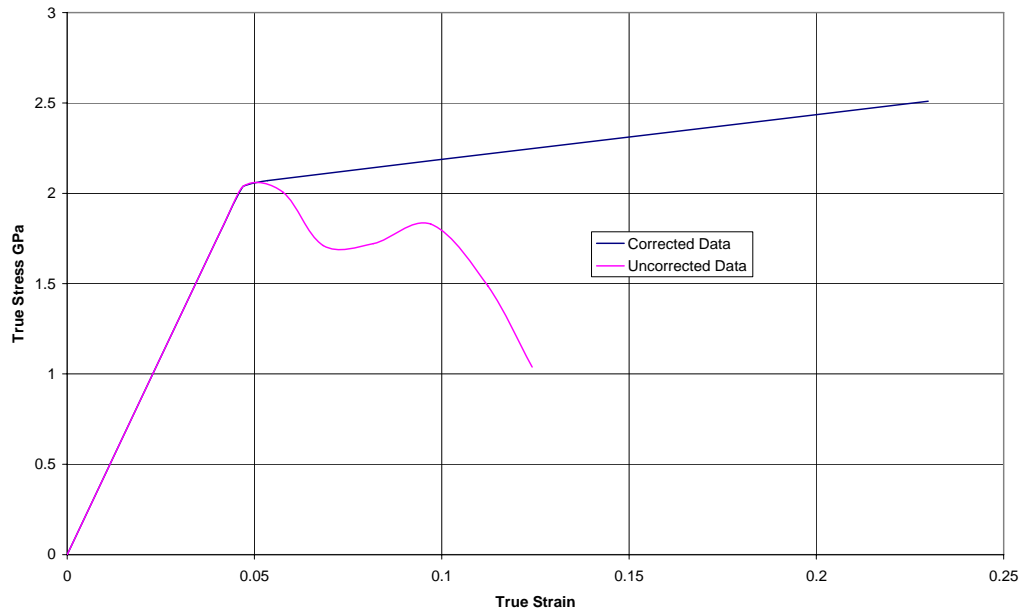
Comparison of Uncorrected and Corrected Data for VascoMax 300 Test 20



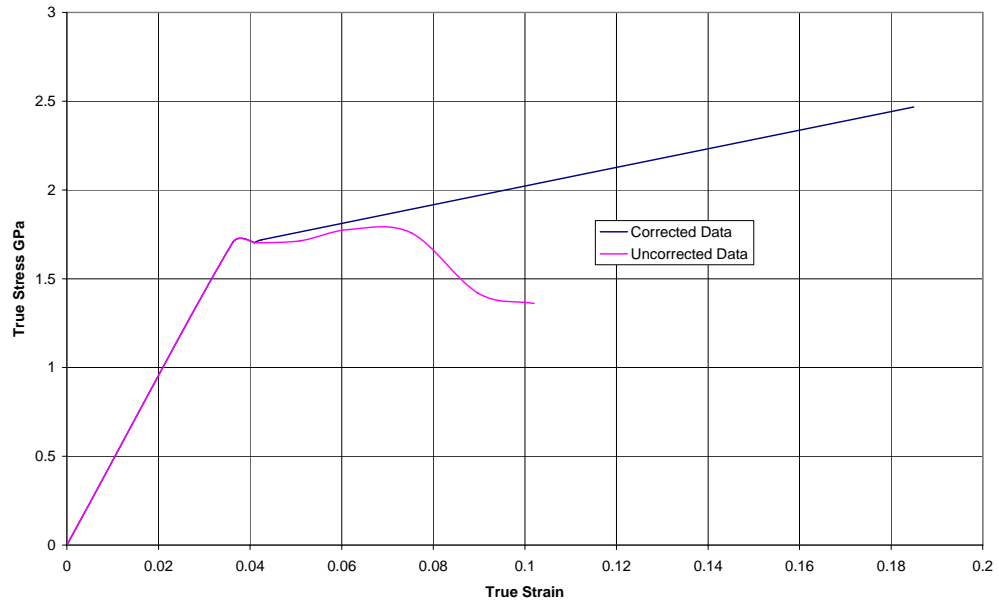
Comparison of Uncorrected and Corrected Data for VascoMax 300 Test 21



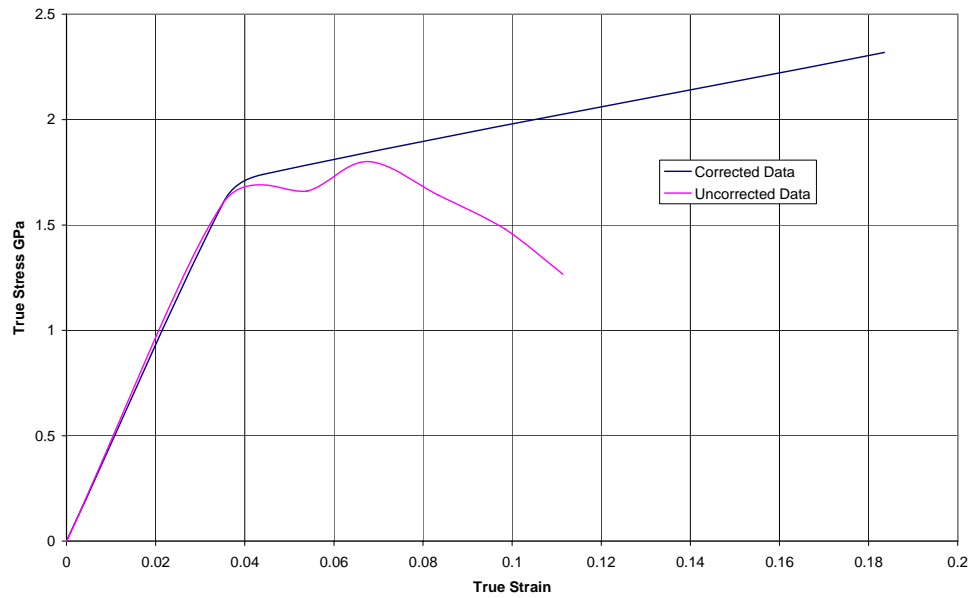
Comparison of Uncorrected and Corrected Data for VascoMax 300 Test 23



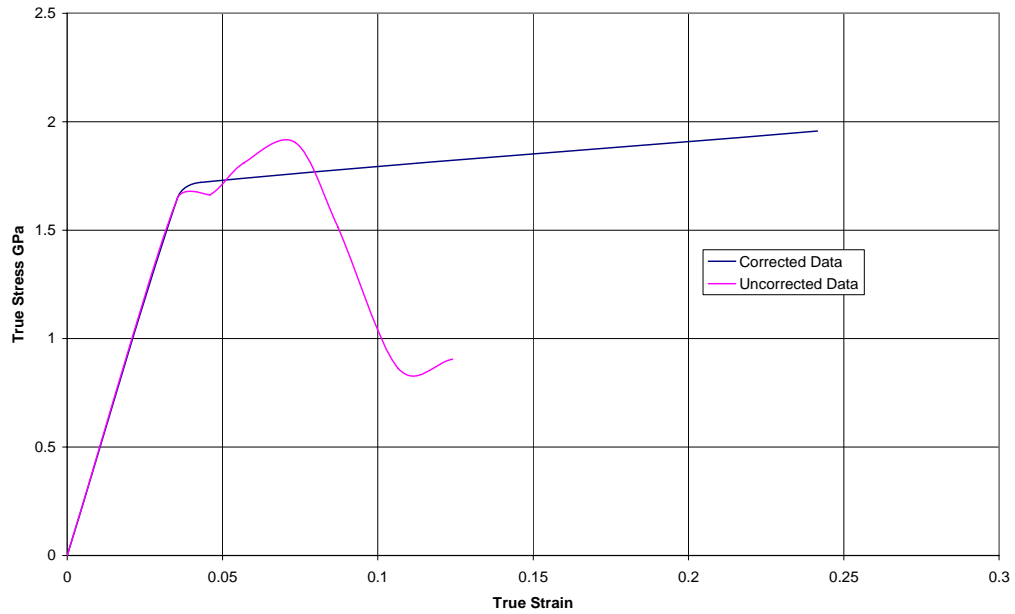
Comparison of Uncorrected and Corrected Data for VascoMax 300 Test 24



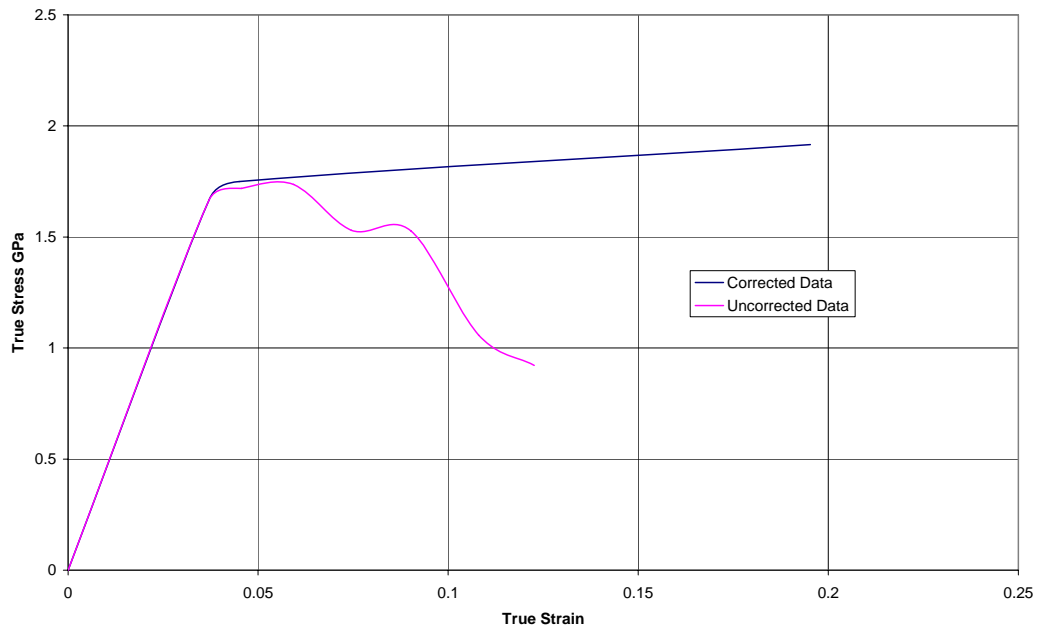
Comparison of Uncorrected and Corrected Data for VascoMax 300 Test 25



Comparison of Uncorrected and Corrected Data for VascoMax 300 Test 26



Comparison of Uncorrected and Corrected Data for VascoMax 300 Test 27



Appendix 4

VascoMax 300 Johnson-Cook modeling

Determination of C Coefficient

Strain Rate	Test Number	Stress at E=.07	Avg Stress	Dynamic/Static Stress	Ln(Strain Rate)
1	Quisi1	2.5390	2.4649	1.0000	0.0000
1	Quisi2	2.3907			
500	3	2.4965	2.5191	1.0220	6.2146
500	4	2.5418			
1000	1	2.5546	2.5877	1.0499	6.9078
1000	2	2.6209			
1500	6	2.4823	2.5194	1.0221	7.3132
1500	7	2.5565			

Determination of m Coefficient

Strain Rate 500

Dynamic Stress 2.519113

Test Number	Strain	Stress	Temp	Log(1-[Dyn. Stress(T) / Dyn. Stress(RT)])	T*	Log(T*)
3 and 4	0.07	2.4700	70	-1.7101	0.0040	-2.4005
15	0.07	1.8955	500	-0.6064	0.1750	-0.7571
16	0.07	1.8776	500	-0.5941	0.1750	-0.7571
19	0.07	1.9196	750	-0.6234	0.2744	-0.5617
20	0.07	1.9995	750	-0.6856	0.2744	-0.5617
17	0.07	1.4399	1000	-0.3681	0.3738	-0.4274
18	0.07	1.4565	1000	-0.3749	0.3738	-0.4274

Strain Rate 1000

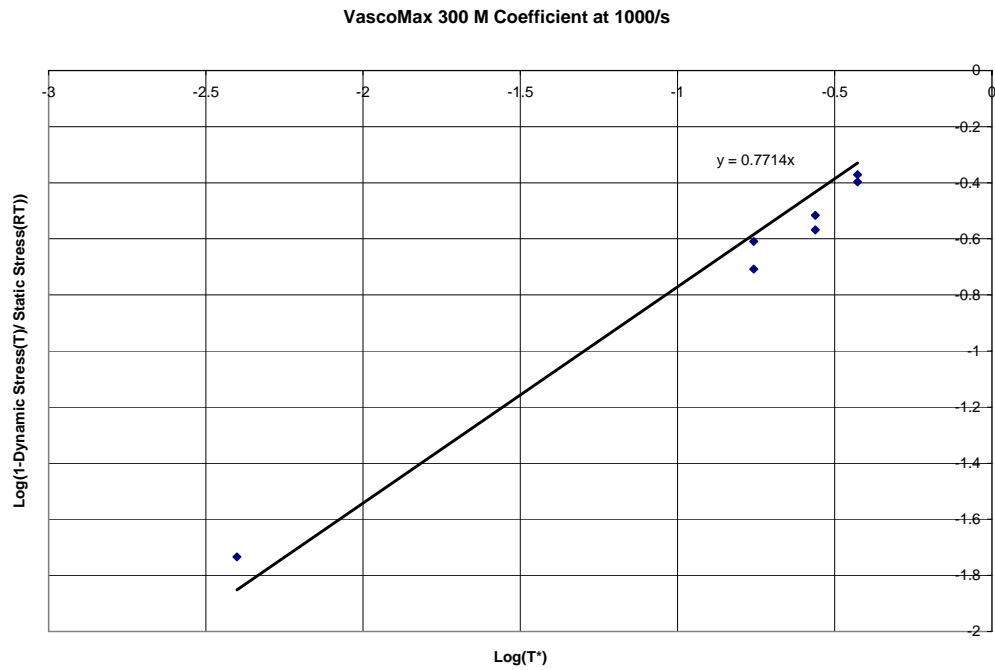
Dynamic Stress 2.587733

Test Number	Strain	Stress	Temp	Log(1-[Dyn. Stress(T) / Dyn. Stress(RT)])	T*	Log(T*)
1 and 2	0.07	2.5400	70	-1.7341	0.0040	-2.4005
9	0.07	1.9522	500	-0.6097	0.1750	-0.7571
28	0.07	2.0809	500	-0.7080	0.1750	-0.7571
10	0.07	1.8883	750	-0.5682	0.2744	-0.5617
11	0.07	1.7998	750	-0.5164	0.2744	-0.5617
12	0.07	1.5501	1000	-0.3969	0.3738	-0.4274
13	0.07	1.4874	1000	-0.3714	0.3738	-0.4274

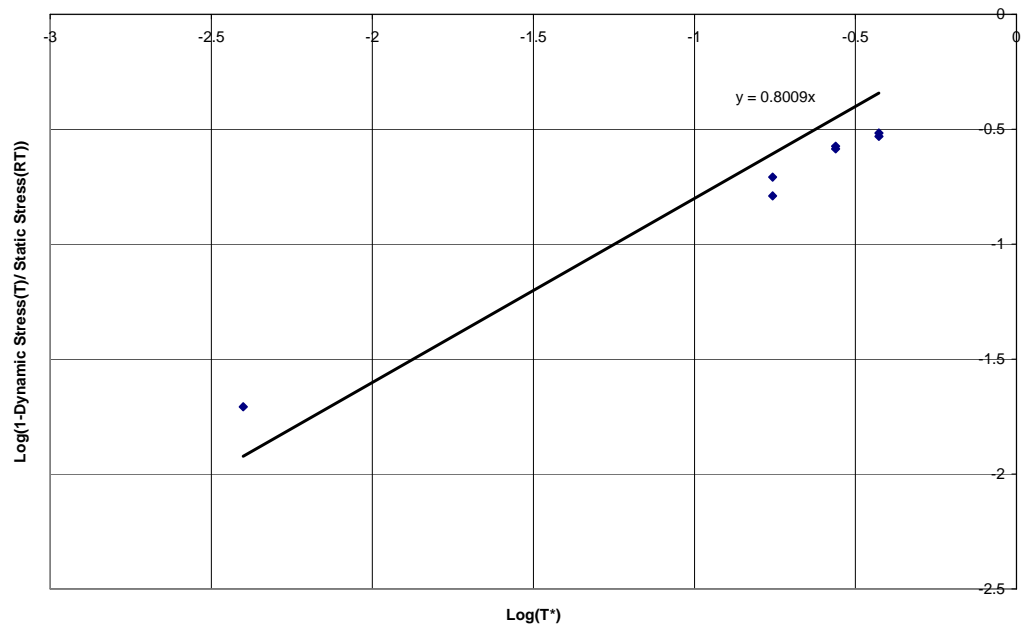
Strain Rate 1500

Dynamic Stress 2.519441

Test Number	Strain	Stress	Temp	Log(1-[Dyn. Stress(T) / Dyn. Stress(RT)])	T*	Log(T*)
6 and 7	0.07	2.4700	70	-1.7072	0.0040	-2.4005
21	0.07	2.0261	500	-0.7082	0.1750	-0.7571
23	0.07	2.1111	500	-0.7903	0.1750	-0.7571
24	0.07	1.8643	750	-0.5849	0.2744	-0.5617
25	0.07	1.8478	750	-0.5742	0.2744	-0.5617
26	0.07	1.7522	1000	-0.5164	0.3738	-0.4274
27	0.07	1.7776	1000	-0.5310	0.3738	-0.4274



VascoMax 300 M Coefficient at 1500/s



Appendix 5

This is a sample CTH code used in evaluation of Johnson-Cook Coefficients for both VascoMax 300 and 1080 steel. It is for 1080 steel rod impacting a rigid wall constructed on VascoMax 300. This code is the same for all CTH runs conducted, except for the parameters yvel, the Johnson-Cook coefficients for each material, and the material equations of state.

CTH Code for 1080 steel Impact

eor genin

Taylor Test: 1080 Impacting VascoMax 300 -New J-C Coeffs. V=123 m/s, 6cm specimen, Test S8

```
control
  mmp
  ep
  vpsave
endcontrol
```

```
mesh
  block 1 geom=2dc type=e * 2dc is two dimensional cylindrical
                        * e is for an Eulerian solution
    x0=0.0
      x1 n=50 w=0.5 dxf=0.01
      x2 n=55 w=5.5 dxf=0.10

    y0=-18.0
      y1 n=170 w=17.0 dyf=0.10
      y2 n=400 w=4.0 dyf=0.01
      y3 n=40 w=4.0 dyf=0.10
    endy
  endb
endmesh
```

/home/afit6/gae05j/zkennan/1080_uncoated

insertion of material

```

block 1
  package topblock
    material 2
    numsub 50
    yvel -123e2    * change only the first number, leave 'e2' this converts m/s to cm/s
  *
    insert box      * this is where you input the cylinder -
      * only model 1/2 of cylinder, and then "mirror" in plotting
      * format is p1 is the bottom center point of cylinder
      * p2 is top right hand corner of cylinder
      p1 0.0 0.1    * change p1 and p2 to define the size of rod
      p2 0.3 6.1
    endinsert
  endpackage

  package bottomblock
    material 1
    numsub 50
    insert box
      p1 0.0, 0.0
      p2 6, -17.5
    endinsert
  endpackage
endblock
endinsertion

edit
  block1
  expanded
endblock
endedit

*

tracer
*Cylinder Top Center                *1 Tracer point at top center to measure final length
  add 0.00 6.10
*Cylinder 0.00cm (Base)              *12 Tracer points along outer edge of
cylinder to estimate deformed profile
  add 0.30 0.10
*Cylinder 0.25cm up from base
  add 0.30 0.35
*Cylinder 0.50cm
  add 0.30 0.60

```



```

matep 2 johnson-cook USER    * change a, b, c, etc for 1080
    ajo=5.25e9,
    bjo=35.9e9,
    cjo=2.9e-2,
    mjo=7.525e-1,
    njo=6.677e-1,
    tjo=.040161e-1,
    poisson 0.27

vpsave
lstrain

*-----
*Slide Line Creation
*-----

slide 1 2

endep

*****
*eor* cthin2.060000E-12

Taylor Test: 1080 Impacting VascoMax 300 -New J-C Coeffs. V=123 m/s, 6cm
specimen

control
    mmp
    tstop = 100e-6    * Max contact time for uncoated S8 lab test is 84 micro sec
endc

Convct
    convection=1
    interface=high_resolution
endc

fracts
    pfrac1 -26.04.0e9
    pfrac2 -6.3e9
    pfmix -12.0e9
    pfvoid -12.0e9
endf

```

```

edit
  shortt
    tim 0.0, dt = 5.0e-6
  ends
  longt
    tim 0.0, dt = 1.0
  endl
  plott
    tim 0.0 dt = 5.0e-6    * this sets the time step it plots at 1/2 microsecond
  endp
  histt
    tim 0.0, dt = 5.0e-6    * this sets the time step it plots at 1/2 microsecond
  htracer all
  endh
ende

boundary
  bhy * rigid boundaries all around
  bl 1
    bxb = 0 , bxt = 1
    byb = 0 , byt = 1      * Changed byb to = 0, this seems to keep the projectile
from disintegrating.
  endb
  endh
endb

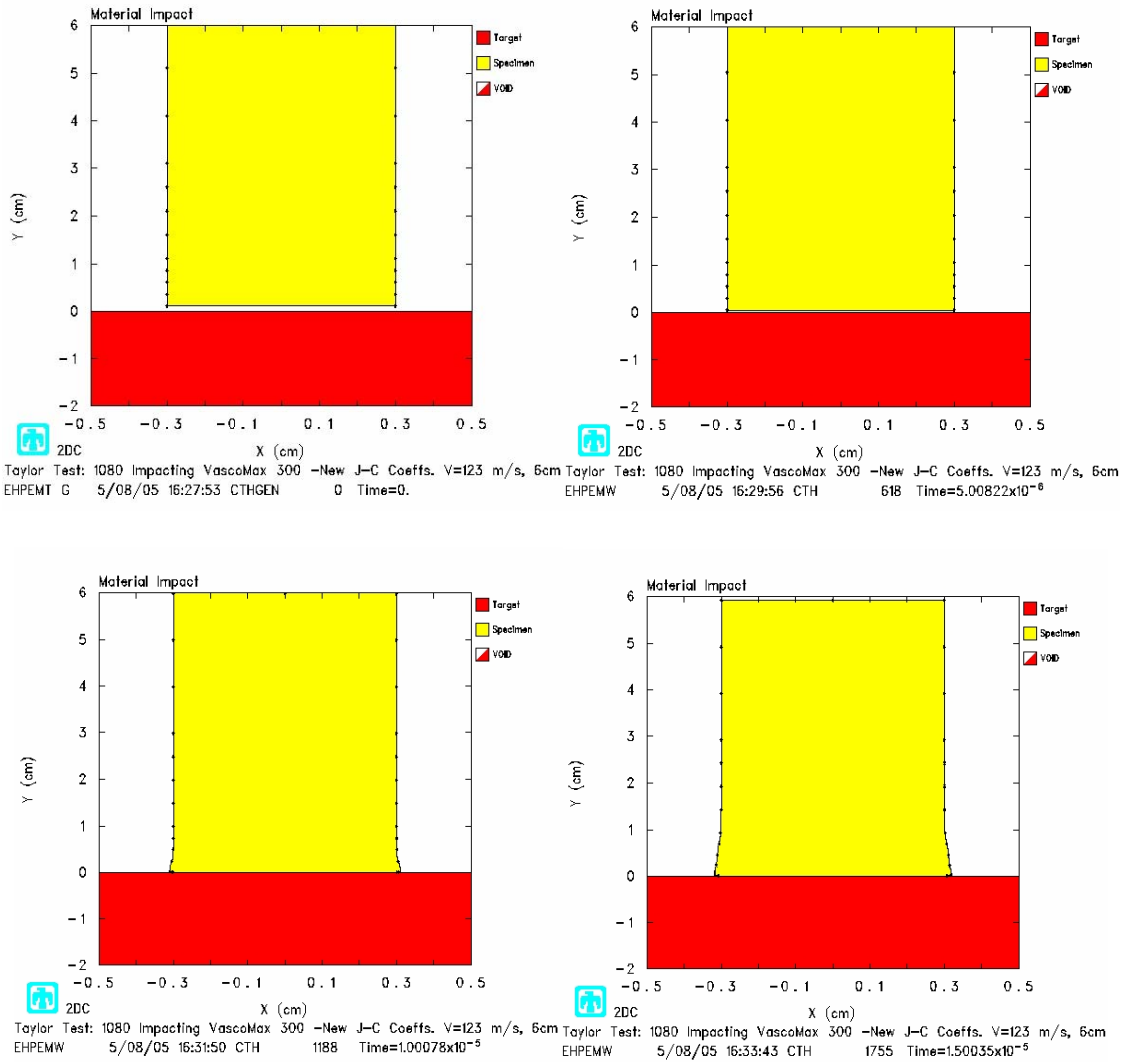
cellthermo
  mmp3      * This was recommended by Eglin and appears
            * to give good results as well.
  ntbad 100000
endc

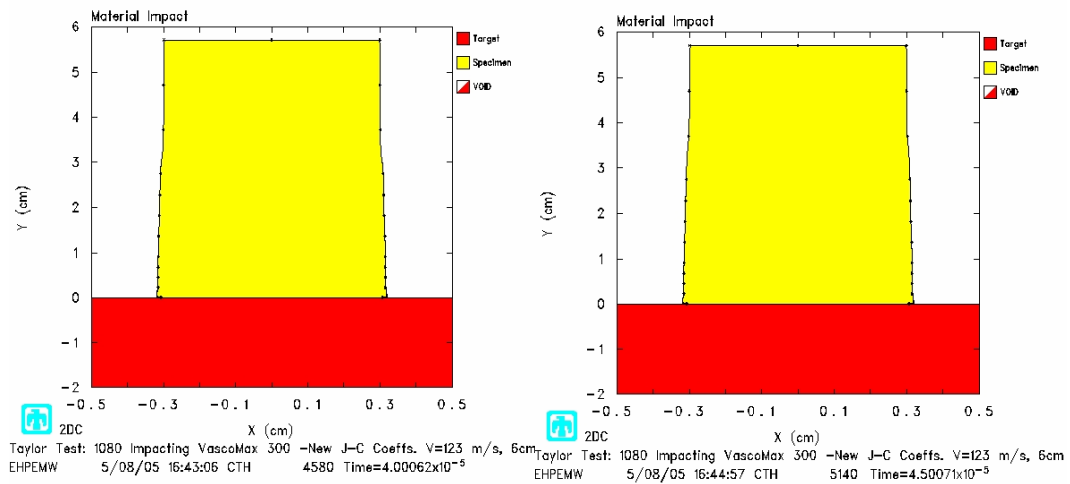
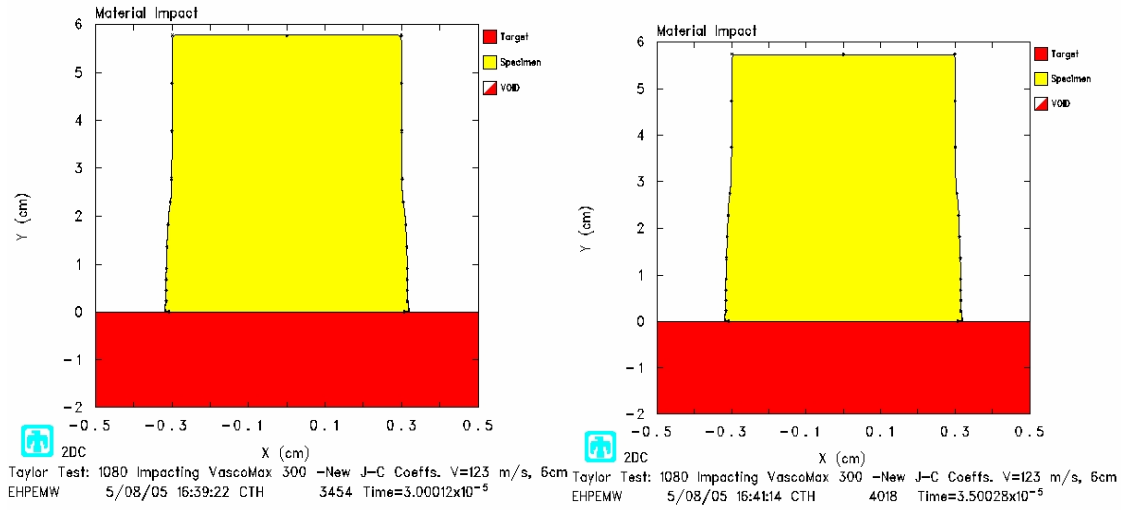
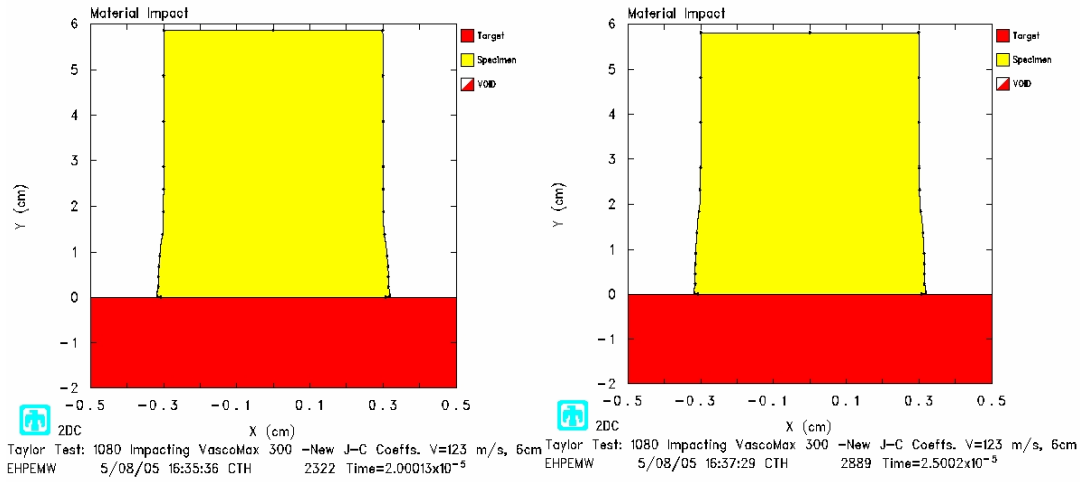
```

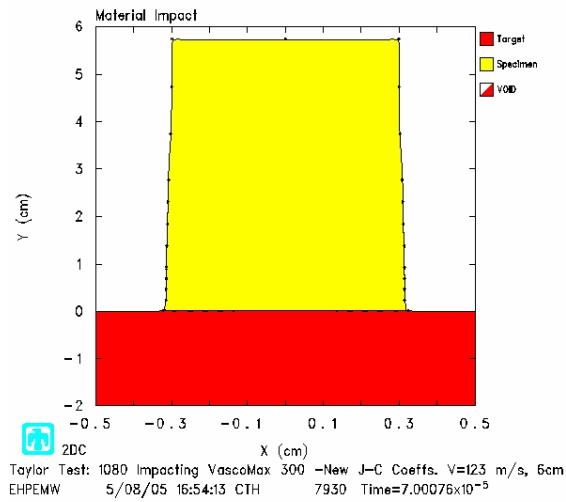
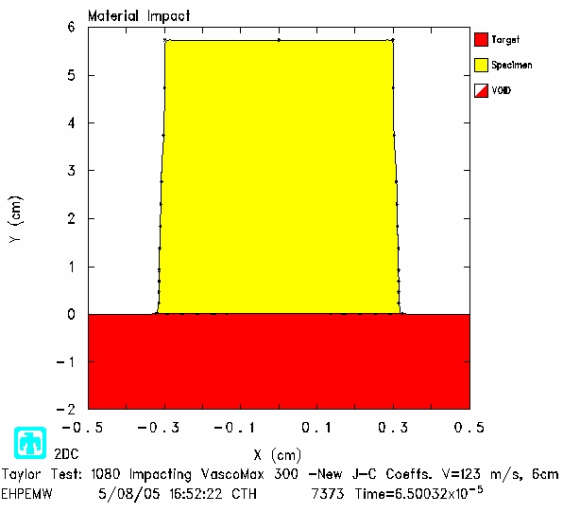
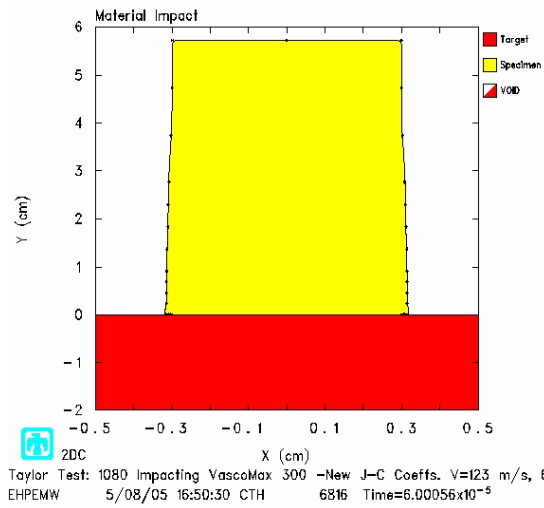
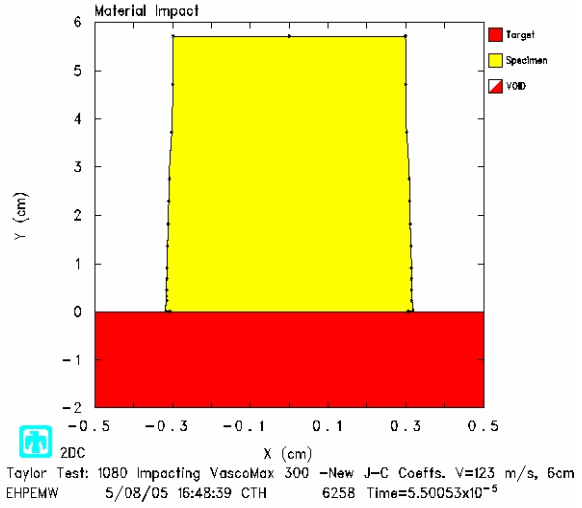
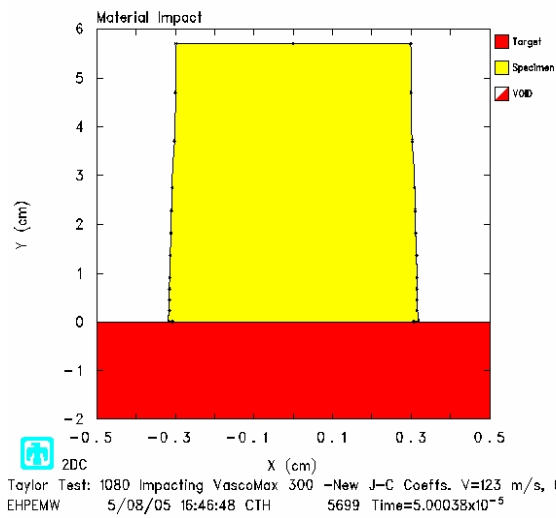
Appendix 6

CTH Deformation Plots for 1080 steel

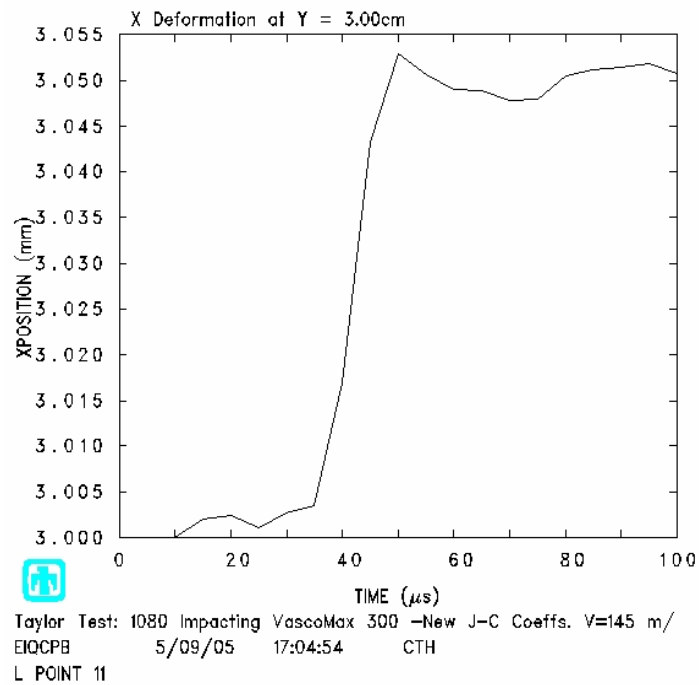
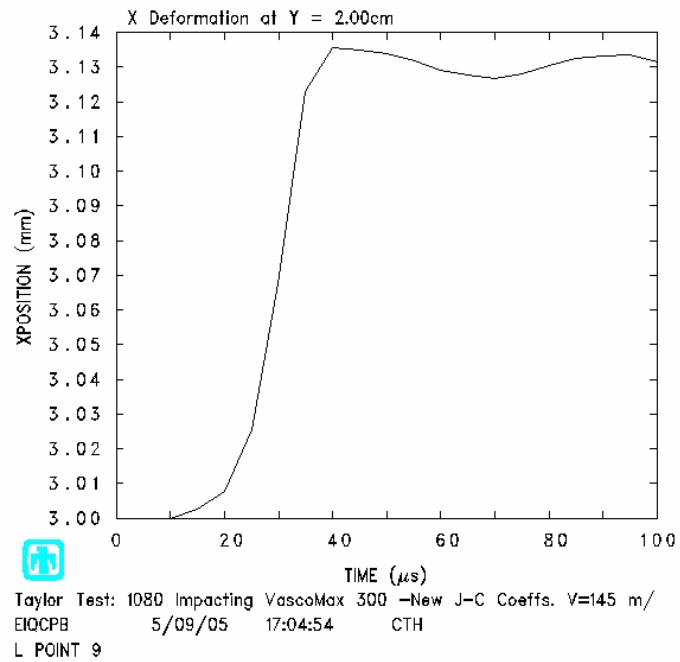
Test S8







Time History Plots for test S9 to confirm undeformed length



Bibliography

1. Rickerd, Gregory S. *An Investigation of a Simplified Gouging Model AFIT/GAE/ENY 05-M19*. Master's Thesis, Air Force Institute of Technology, Wright-Patterson AFB OH, March 2005.
2. Laird, David J. *The Investigation of Hypervelocity Gouging AFIT/DS/ENY 02-01*. PhD dissertation, Air Force Institute of Technology, Wright-Patterson AFB OH, March 2002.
3. Laird, D and A Palazotto. "Gouge development during hypervelocity sliding impact," *International Journal of Impact Engineering*, 30:205-223 (2004).
4. Hooser, Dr Michael. "Simulation of a 10,000 Foot per Second Ground Vehicle." *21st AIAA Advanced Measurement Technology and Ground Testing Conference*. Number AIAA 2000-2290. Denver CO: AIAA, 2000.
5. Nicholas, Theodore and Rodney F. Recht. *High Velocity Impact Dynamics*, chapter 1 Introduction to Impact Phenomena, 1-63. New York NY: John Wiley and Sons., 1990.
6. Nicholas, Theodore. Class Handout, AERO 899, High Velocity Impact. School of Engineering and Management, Air Force Institute of Technology, Wright-Patterson AFB OH, Fall Quarter 2004.
7. Nicholas, Theodore. *Impact Dynamics*, chapter 4 Elastic-Plastic Stress Waves, 95-154. Malabar FL: Krieger Publishing Company., 1982.
8. Nicholas, Theodore. "Tensile Testing of Materials at High Rates of Strain". *Experimental Mechanics*, 177-185, May, 1981.
9. Frew, Danny J. *Dynamic Response of Brittle Materials from Penetration and Split Hopkinson Pressure Bar Experiments*. Technical Report ERDC/GSL TR-01-6, U.S. Army Engineer Research and Development Center, MS, 2001.
10. Zukas, Jonas A. *Introduction to Hydrocodes*, San Diego CA: ELSEVIER Inc., 2004.
11. Cinnamon Cinnamon, John D., Anthony N. Palazotto, Z. Kennan, N. S. Brar, and D. Bajaj. "Johnson-Cook Strength Model Constants for VascoMax 300 and 1080 Steels". *14th APS Topical Conference on Shock Compression of Condensed Matter*.

12. J.P. Noble B.D. Goldthorpe, Church, J. Harding. "The use of the Hopkinson bar to validate constitutive relations at high rates of strain". *Journal of Mechanics and Solids*, 47:1187-1206.
13. Zerilli, Frank J., and Armstrong, Ronald W. "Dislocation-Mechanics-based constitutive relations for material dynamics calculations". *Journal of Applied Physics*, 61:1816-1825.
14. Brar, Singh N. *Characterization of VascoMax 300 and 1080 Steels at High Strain Rate and High Temperature*. Technical Report UDR-TR-2005-00049, University of Dayton Research Institute, University of Dayton, OH, 2005.
15. *Taylor Hobson*. Form Talysurf Series 2. Rolling Meadow: Taylor Hobson Inc, no date
16. Szmerekovsky, Andrew G. *The Physical Understanding of the use of Coatings to Mitigate Hypervelocity Gouging Considering Real Test Sled Dimensions AFIT/DS/ENY 04-06*. PhD dissertation, Air Force Institute of Technology, Wright-Patterson AFB OH, September 2004.
17. Palazotto, Dr; Cinnamon; Kennan; Blomer. "Development of a High Strain-Rate Constitutive Relationship for Hypervelocity Impact". Proceedings of the 2005 ASME International Congress, November 2005.
18. Szmerekovsky, Andrew G. *The Physical Understanding of the use of Coatings to Mitigate Hypervelocity Gouging Considering Real Test Sled Dimensions AFIT/DS/ENY 04-06*. PhD dissertation, Air Force Institute of Technology, Wright-Patterson AFB OH, September 2004.
19. Blomer, Mark A. *Cost Comparison of Existing Coatings for a Hypervelocity Test Rail AFIT/GAE/ENY 05-J01*. Master's Thesis, Air Force Institute of Technology, Wright-Patterson AFB OH, June 2005.
20. Meyers, Marc André. *Dynamic Behavior of Materials*. New York NY: John Wiley and Sons, Inc., 1994.

Vita

Zachary Kennan was born in Abington, PA and raised in Willow Grove, PA until 1992, when his family moved to Cherry Hill, New Jersey. There he attended and graduated from Cherry Hill High School East. Having earned a Navy ROTC scholarship, he was accepted to the Georgia Institute of Technology, where he earned his Bachelors of Science in Aerospace Engineering. Upon graduating from Georgia Tech, he was commissioned into the United States Navy as an Ensign and earned a designator of student aviator. After a short period of duty at NROTC Atlanta Region, he reported to the Air Force Institute of Technology at Wright-Patterson AFB. He is currently working on his master's degree in Aeronautical Engineering.

REPORT DOCUMENTATION PAGE					Form Approved OMB No. 074-0188	
<p>The public reporting burden for this collection of information is estimated to average 1 hour per response, including the time for reviewing instructions, searching existing data sources, gathering and maintaining the data needed, and completing and reviewing the collection of information. Send comments regarding this burden estimate or any other aspect of the collection of information, including suggestions for reducing this burden to Department of Defense, Washington Headquarters Services, Directorate for Information Operations and Reports (0704-0188), 1215 Jefferson Davis Highway, Suite 1204, Arlington, VA 22202-4302. Respondents should be aware that notwithstanding any other provision of law, no person shall be subject to a penalty for failing to comply with a collection of information if it does not display a currently valid OMB control number.</p> <p>PLEASE DO NOT RETURN YOUR FORM TO THE ABOVE ADDRESS.</p>						
1. REPORT DATE (DD-MM-YYYY)		2. REPORT TYPE		3. DATES COVERED (From – To)		
13-06-2005		Master's Thesis		Jun 2004 – Jun 2005		
4. TITLE AND SUBTITLE Determination of the Constitutive Equations for 1080 Steel and VascoMax 300				5a. CONTRACT NUMBER		
				5b. GRANT NUMBER		
				5c. PROGRAM ELEMENT NUMBER		
6. AUTHOR(S) Kennan, Zachary A., Ensign, USNR				5d. PROJECT NUMBER If funded, enter ENR #		
				5e. TASK NUMBER		
				5f. WORK UNIT NUMBER		
7. PERFORMING ORGANIZATION NAMES(S) AND ADDRESS(S) Air Force Institute of Technology Graduate School of Engineering and Management (AFIT/EN) 2950 Hobson Way WPAFB OH 45433-8865				8. PERFORMING ORGANIZATION REPORT NUMBER AFIT/GAE/ENY/05-J05		
9. SPONSORING/MONITORING AGENCY NAME(S) AND ADDRESS(ES) Dr. Neal Glassman, AFOSR (AFRL) 4015 Wilson Blvd, Room 713 Arlington, VA 22203-1954				10. SPONSOR/MONITOR'S ACRONYM(S)		
				11. SPONSOR/MONITOR'S REPORT NUMBER(S)		
12. DISTRIBUTION/AVAILABILITY STATEMENT APPROVED FOR PUBLIC RELEASE; DISTRIBUTION UNLIMITED.						
13. SUPPLEMENTARY NOTES						
14. ABSTRACT <p>The objective of this research is to establish a better representation of the components utilized in a gouging event being considered in research leading to a better understanding of the Holloman High Speed Test Track. Gouging occurs when two metals are traveling at a slight incline to each other at velocities nearing 1.5 kilometers per second, and results in a structural failure of both the metals. The gouging process occurs at very high strain rates, which results in non-linear stress-strain relations.</p> <p>The coefficients that lead to the Johnson-Cook equations have been determined by the Split Hopkinson Bar test for 1080 steel and VascoMax 300. The Split Hopkinson Bar test was conducted using various strain rates and temperatures to produce meaningful stress-strain relations for both of the steels. These relations allowed a fit of the data to yield specific material coefficients defined in the Johnson-Cook constitutive model. Both the 1080 steel and VascoMax 300 models showed excellent approximation of the plastic region. Verification of the constitutive models was conducted through the use of Taylor tests. A Taylor test model utilizing the constitutive equations was developed in CTH and produced deformation profiles that closely resembled specimens taken from experimental Taylor tests. The end result of this work will be utilized in further studies toward overall high energy impact evaluation.</p>						
15. SUBJECT TERMS Impact, Impact Loads, Impact Tests, Constitutive Equations, Split Hopkinson Bar, Johnson-Cook						
16. SECURITY CLASSIFICATION OF:			17. LIMITATION OF ABSTRACT	18. NUMBER OF PAGES	19a. NAME OF RESPONSIBLE PERSON	
a. REPORT	b. ABSTRACT	c. THIS PAGE			Dr. A.N. Palazotto, USAF	
U	U	U	UU	186	19b. TELEPHONE NUMBER (Include area code) (937) 255-3636 x4599 (anthony.palazotto@afit.edu)	